European laboratory for
Non-Linear Spectroscopy
Dipartimento di Fisica e Astronomia

International Doctorate in
Atomic and Molecular Photonics
Ciclo XXXVIII

Single Strontium atoms trapped in optical tweezer arrays for quantum simulation

Candidate

Veronica Giardini (ID number DT31655)

Thesis Advisor

Prof. Leonardo Fallani

Coordinator

Prof. Diederik S. Wiersma

Co-Advisor

Dr. Vladislav Gavryusev

Academic Year 2025/2026

Thesis defended on ——
in front of a Board of Examiners composed by:

—— (chairman)

——

——

Single Strontium atoms trapped in optical tweezer arrays for quantum simulation
PhD thesis. University of Florence

This thesis has been typeset by LaTeX and the UniFiTh class.

Version: February 23, 2026

Author's email: giardiniv@lens.unifi.it

Abstract

Optical tweezer arrays of neutral atoms have emerged as a versatile and powerful platform for quantum simulation and quantum information processing. In this thesis, I present the realization of an experimental platform for quantum simulation based on individually trapped strontium atoms in optical tweezer arrays. The experiment combines precise laser cooling, optical control, and high-resolution imaging to enable the manipulation and high fidelity detection of single atoms. I developed and optimized a two-stage three-dimensional magneto-optical trap (3D-MOT) that produces cold and dense samples of strontium atoms from a thermal beam. In the first stage, atoms are captured and precooled using the dipole-allowed $^1S_0 \rightarrow {}^1P_1$ transition at 461 nm (which has a linewidth of $\Gamma = 2\pi \times 32\,\mathrm{MHz}$). The second stage employs the $^1S_0 \rightarrow {}^3P_1$ narrow intercombination transition at 689 nm (with a linewidth of $\Gamma = 2\pi \times 7.5\,\mathrm{kHz}$) to further cool and compress the atomic cloud. By optimizing the trapping parameters, I achieved clouds with temperatures around 5 µK and densities above $10^{10}\,\mathrm{cm}^{-3}$, providing ideal initial conditions for efficient loading into optical tweezers.

A 3×3 array of 360 µK deep optical tweezers is generated by spatially modulating an 813.4 nm laser beam using two crossed acousto-optic deflectors. The deflected beams are relayed and focused into the science chamber using a high–numerical-aperture objective, which simultaneously serves as the collection optics for atomic fluorescence. The fluorescence light emitted by the atoms is imaged onto a scientific qCMOS camera, enabling site-resolved detection of individual atoms. I implemented and optimized the in-trap cooling dynamics to prevent atom loss during imaging and to minimize residual thermal motion. In addition, by precisely tuning light-assisted collisions, multiple atoms occupancies are removed from the traps and a single-atom regime is reached in the array, with a filling fraction of about 50%. I have demonstrated a single-atom detection fidelity of 99,986(1)% and a survival probability of 97(2)% between subsequent image acquisition, comparable to other current state-of-the-art experiments. To characterize the platform, I carried out release-and-recapture experiments, from which it is possible to measure a temperature for the individually trapped atoms of 12.95(5) µK.

These results demonstrate the successful implementation of a robust and high-fidelity platform for optical trapping and imaging of single strontium atoms. The apparatus provides the foundation for future quantum simulation experiments with alkaline-earth atoms excited to the Rydberg state, offering precise control over individual particles and the ability to scale towards larger, programmable atomic arrays.

My publications

Parts of the work presented in this thesis have been published or are in preparation for publication:

1. M. Ammenwerth, H. Timme, **V. Giardini**, R. Tao, F. Gyger, O. Lib, D. Berndt, D. Kourkoulos, T. Rom, I. Bloch, and J. Zeiher, *"Dynamical spatial light modulation in the ultraviolet spectral range,"* **Physical Review Applied 24**, 034031 (2025).

2. **V. Giardini**, L. Guariento, A. Fantini, S. Storm, M. Inguscio, J. Catani, G. Cappellini, V. Gavryusev, and L. Fallani, *"Single Strontium Atoms in Optical Tweezer Arrays for Quantum Simulation,"* *arXiv*:2510.19816 [physics.atom-ph] (2025), `https://doi.org/10.48550/arXiv.2510.19816`.

Acknowledgments

I would like to express my deepest gratitude to my supervisor, Prof. Leonardo Fallani, for his guidance during my doctoral studies, which has been fundamental to the development of this thesis and to my growth as both a researcher and a person.

I would also like to warmly thank my co-advisor, Dr. Vladislav Gavriusev, for his support, patience, and the stimulating discussions we shared over these years, as well as Dr. Jacopo Catani, Dr. Luca Guariento, Andrea Fantini, and Shawn Storm for collaborating with me in the laboratory, for their advice, and for the challenges we faced together.

Finally, I want to thank my family for their unconditional support and encouragement throughout this journey, and my friends for sharing both the highs and lows of these years with me and for making this experience truly memorable.

Contents

Chapter 1

Introduction

1.1 Motivation: Why Quantum Simulators?

Understanding the dynamics and properties of complex quantum systems is one of the greatest challenges in modern physics. Classical computers face enormous difficulties in tackling such problems due to the intrinsically exponential scaling of complexity of quantum mechanical problems. For a system composed of n two-level quantum particles, the number of basis states grows exponentially as 2^n, making exact simulation with classical computational resources impossible. Even just a few dozen particles exceed the capabilities of the most powerful supercomputers [1]. Moreover, fundamental quantum phenomena such as entanglement introduce correlations and dynamics that cannot be efficiently represented using classical bits and probabilities. Many problems in quantum physics fall into computational complexity classes that are inaccessible to classical algorithms, even in theory. These limitations hinder the study of many-body quantum phenomena such as high-temperature superconductivity, quantum magnetism, or non-equilibrium dynamics in strongly correlated systems.

This challenge was famously articulated by Richard Feynman in 1982, who proposed the concept of a controllable quantum system engineered to simulate another target quantum system, a quantum simulator [2]. Feynman observed that, as quantum systems themselves exhibit exponential complexity, this property could be harnessed positively: a quantum device could encode exponentially large information without requiring an exponentially large amount of physical hardware, making it a natural platform for simulating quantum phenomena. This is the idea behind the quantum simulator. By engineering such systems to mimic the behavior of target models, quantum simulators allow direct experimental access to many-body quantum physics. These analog simulators provide a powerful alternative to fully digital quantum computers, especially in the near term, where scalable fault tolerance remains a significant challenge [3, 4].

Let us consider a quantum system, whose state is denoted by $|\varphi\rangle$. The system evolves from the initial state $|\varphi(0)\rangle$ to $|\varphi(t)\rangle$ via the unitary transformation $U = \exp\{-i\hbar H_{\text{sys}} t\}$, where H_{sys} is the Hamiltonian of the system. In order to study this system we can use a controllable quantum simulator: one can prepare the initial state $|\psi(0)\rangle$, implement the desired evolution $U' = \exp\{-i\hbar H_{\text{sim}} t\}$, where

H_{sim} is the Hamiltonian of the simulator, and measure the final state $|\psi(t)\rangle$. If a mapping between the system and the simulator (i.e., between $|\varphi(0)\rangle$ and $|\psi(0)\rangle$, and between $|\varphi(t)\rangle$ and $|\psi(t)\rangle$) exists, then the dynamics of the original system can be effectively simulated. This is the basic idea of quantum simulation and it is represented schematically in Fig. 1.1.

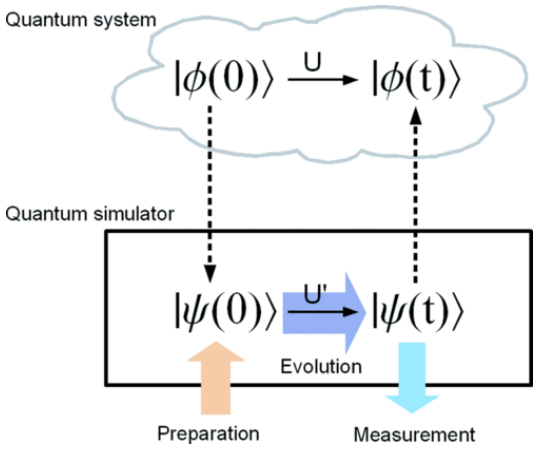

Figure 1.1. Schematic representation of a quantum system and its corresponding quantum simulator. The quantum state $|\varphi(0)\rangle$ evolves into $|\varphi(t)\rangle$ via the unitary transformation $U = \exp\{-i\hbar H_{\text{sys}}t\}$. The quantum simulator evolves from the state $|\psi(0)\rangle$ into $|\psi(t)\rangle$ via $U' = \exp\{-i\hbar H_{\text{sim}}t\}$. The simulator is designed to reproduce the behavior of the simulated system through specific mappings: $|\varphi(0)\rangle \leftrightarrow |\psi(0)\rangle$, $|\varphi(t)\rangle \leftrightarrow |\psi(t)\rangle$, and $U \leftrightarrow U'$. While the simulated system may be uncontrollable or experimentally inaccessible, the simulator is fully controllable: the initial state $|\psi(0)\rangle$ can be prepared, the unitary evolution U' can be engineered, and the final state $|\psi(t)\rangle$ can be measured. The result of this measurement provides information about the simulated system. The colored arrows denote the controllable operations. The solid black arrows describe the time evolution of the system and the simulator. The dashed arrows indicate the correspondence between the quantum states of the simulator and the simulated system. Figure taken from Ref. [1].

The mapping between the simulator and the simulated system can be implemented through either analog or digital approaches. In analog quantum simulation, the simulator's Hamiltonian is engineered to reproduce the target model directly, allowing the system to naturally evolve under equivalent dynamics. In digital quantum simulation, the desired evolution is constructed from a discrete sequence of quantum gate operations that approximate the target unitary transformation. While the former captures specific physical models with high efficiency, the latter provides universality and programmability at the cost of increased experimental complexity.

1.2 Historical Development and Physical Platforms for Quantum Simulation

The idea of quantum simulation originated with Feynman's visionary proposal in the early 1980s, and was further formalized by Lloyd in 1996, who showed that quantum systems can efficiently simulate any local quantum Hamiltonian [5].

The experimental pursuit of quantum simulators has advanced rapidly, driven by technological innovations and a growing understanding of how to engineer controllable quantum systems. Over the past few decades, several distinct physical platforms have emerged, each offering unique capabilities and challenges, and contributing to the development of quantum simulation in complementary ways.

Among the first platforms to realize many-body quantum simulations in the laboratory were ensembles of ultracold atoms in optical lattices. Enabled by breakthroughs in laser cooling and optical trapping, these systems provided a natural realization of lattice models such as the Bose–Hubbard and Fermi–Hubbard Hamiltonians. Notably, the observation of the superfluid–Mott insulator transition in bosonic systems represented a landmark achievement, demonstrating the potential of quantum simulators to access strongly correlated quantum phases [6]. Optical lattice experiments have since enabled the study of quantum magnetism [7, 8], topological states [9], and out-of-equilibrium dynamics in extended many-body systems [10, 11].

Trapped ions have constituted another highly successful platform, enabled by progress in radio-frequency trapping techniques, precise laser-based quantum control, and state-of-the-art vacuum and cryogenic technologies. These systems offer exceptionally long coherence times and allow for high-fidelity initialization, manipulation, and readout of individual qubits [12, 13]. Using the collective vibrational modes of ion chains as a quantum bus, effective spin models, such as transverse-field Ising Hamiltonians, can be engineered with tunable interaction ranges [14, 15, 16]. Landmark experiments have demonstrated the simulation of quantum phase transitions, non-equilibrium dynamics, and entangled states involving tens of individually addressable ions [17, 18]. These features make trapped ions a versatile platform for both analog and digital quantum simulation protocols.

Superconducting circuits, based on Josephson junctions and microwave resonators, have also played a major role in the evolution of quantum simulators. Advances in microfabrication and cryogenic techniques have allowed the realization of strongly interacting arrays of artificial atoms, that can act as qubits with tunable parameters and fast gate operations [19]. Superconducting platforms have enabled the exploration of quantum optics in circuit QED architectures [20, 21], as well as the simulation of lattice gauge theories [22] and spin models [23].

Other platforms, such as photonic systems [24, 25] and semiconductor quantum dots [26, 27], are also being explored for specific applications in quantum simulation, though challenges in scalability and interaction control remain significant.

1.3 Neutral Atoms in Optical Tweezers

In the landscape of quantum simulation platforms, neutral atoms in optical tweezer arrays have recently emerged as a powerful and highly adaptable alternative to more established systems such as optical lattices, trapped ions, and superconducting circuits. Enabled by the ability to trap and manipulate individual atoms using tightly focused laser beams, these platforms offer a combination of high spatial resolution, individual addressability, and dynamic reconfigurability, offering a level of control that was previously inaccessible in large-scale quantum architectures [28]. Compared to traditional optical lattices, optical tweezer arrays provide significantly

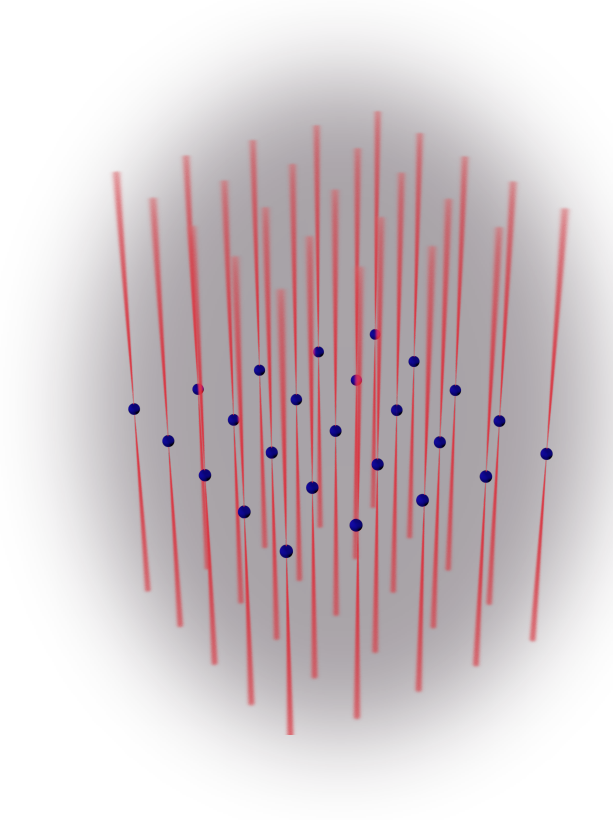

Figure 1.2. Schematic representation of an Array of optical tweezers (red beams) trapping individual atoms (blue spheres).

enhanced control. Atoms can be arranged in arbitrary geometries, repositioned in real time, and initialized with near-unity filling through active rearrangement protocols [29].

Using highly excited Rydberg states, long-range interactions between atoms can be engineered in a tunable and programmable way, enabling the simulation of spin models with customizable geometry, interaction range, and connectivity [30]. These features have been exploited to study diverse many-body phenomena, including quantum phase transitions [31], topological model[32], and quantum optimization problems [33].

A particularly promising direction involves the use of alkaline-earth(-like) atoms, such as Strontium (Sr) or Ytterbium (Yb) [34, 35]. These species offer long-lived metastable states, narrow optical transitions, and rich internal structures, making them ideal for high-precision control and quantum state encoding. Their electronic and nuclear spin degrees of freedom enable novel schemes for information storage and manipulation, as well as potential synergies with optical clocks and precision metrology.

Recent experimental advances have demonstrated the assembly of defect-free arrays comprising hundreds or thousands of atoms, with coherent control over their quantum

evolution [36, 33, 37, 38, 39]. Combined with a growing toolbox—including local addressing, Rydberg dressing, and real-time geometry shaping—optical tweezer arrays now stand at the forefront of programmable quantum simulation, offering a uniquely versatile platform for probing complex many-body physics in both equilibrium and out-of-equilibrium regimes.

1.4 Scope and structure of this thesis

This thesis presents the work carried out during the three years of my PhD, dedicated to the construction and development of the first Italian platform for quantum simulation using Strontium Rydberg atoms trapped in optical tweezers. The project lies at the intersection of atomic physics, quantum optics, and quantum information science, and aims to establish a scalable and coherent quantum simulator capable of exploring many-body quantum phenomena.

The thesis is structured to provide a coherent path from the fundamental principles of atom–light interaction to the experimental realization of single-atom arrays for quantum simulation. Chapter 2 provides a theoretical overview of atom–light interactions, laser cooling, and trapping mechanisms, which form the basis for the manipulation of neutral atoms. Chapter 3 follows with a detailed description of the electronic structure of the strontium atom, emphasizing the optical transitions used for cooling, imaging, and coherent excitation to Rydberg states. Chapter 4 introduces the concept of optical tweezers and discusses their implementation in this work, including beam-shaping techniques and the generation of tweezer arrays. The physics of Rydberg atoms is explored in Chapter 5, where excitation to high-lying states enables strong and controllable interactions between neutral atoms, a fundamental mechanism for realizing and probing many-body quantum dynamics. The technical realization of the experimental setup is presented in Chapter 6, which describes the vacuum apparatus, magnetic-field control, and laser systems employed the experiment. Chapter 7 then focuses on the development and characterization of a two-stage magneto-optical trap for strontium, based on the broad 461 nm and narrow 689 nm transitions. Chapter 8 presents the loading of atoms into optical tweezers and the full preparation sequence leading to arrays of single strontium atoms, as well as the methods used for imaging, detection, and signal analysis. Finally, Chapter 9 concludes the thesis with an outlook on future directions, including Rydberg excitation, atom reordering, system scaling, and the implementation of Ising and XY quantum models.

Chapter 2

Cooling and trapping

The interaction between atoms and light is fundamental in atomic physics, especially in the context of laser cooling and trapping. This chapter provides an overview of the main aspects of laser cooling and trapping that are employed in the realization of the experiment.

2.1 Theory of Atom-Light Interaction

To describe the interaction between atoms and light in a tractable way, the semi-classical approximation is often employed, in which the atomic degrees of freedom are treated quantum mechanically, while the electromagnetic field is modeled as a classical monochromatic wave. This description remains valid in the regime of large photon numbers, where quantum fluctuations of the radiation field are negligible. In this framework, a simple yet instructive model is that of a two-level atom interacting with a near-resonant light field. The Hamiltonian in the rotating-wave approximation (RWA) is given by [40, 41]:

$$H = \frac{\hbar\Delta}{2}\sigma_z + \frac{\hbar\Omega}{2}\sigma_x \tag{2.1}$$

where $\Delta = \omega_L - \omega_0$ is the detuning between the laser frequency ω_L and the atomic transition frequency ω_0, Ω is the Rabi frequency proportional to the electric field amplitude, and σ_i are Pauli matrices operating on the two-level basis. The dynamics of population and coherence between the states are governed by the optical Bloch equations, or equivalently by the master equation for the density matrix ρ:

$$\frac{d\rho}{dt} = -\frac{i}{\hbar}[H, \rho] + \mathcal{L}[\rho] \tag{2.2}$$

where $\mathcal{L}[\rho]$ accounts for dissipative processes such as spontaneous emission. This formalism allows us to predict not only populations, but also steady-state behavior and transient dynamics in the atom-light interaction. In absorption and emission process not only the internal state changes, there is also a momentum exchange between light and atom. Each absorption and spontaneous emission event imparts a recoil of $\hbar k$ to the atom, where k is the wavevector of the light. This repeated interaction leads to the so-called radiative forces, including the radiation pressure force and the optical dipole force.

These concept form the foundation for understanding laser cooling mechanisms, radiation pressure forces, and light-assisted trapping techniques, which are discussed in the following sections. A full quantum treatment of atom-light interaction (especially in low-intensity or tightly focused regimes) requires the quantization of the light field, using the Jaynes–Cummings model or master equation approaches. However, for most laser cooling applications, the semiclassical picture provides an excellent approximation

2.2 Radiation pressure

When an atom absorbs a photon from a near-resonant laser beam, it receives a momentum kick of magnitude $\mathbf{p} = \hbar\mathbf{k}$ in the direction of the wavevector $\mathbf{k}$, where $k = \frac{2\pi}{\lambda}$ and λ is the wavelength of the atomic transition. After a characteristic time determined by the excited-state lifetime, the atom spontaneously emits a photon in a random direction and returns to the ground state. As a result, over many absorption–emission cycles, the atom experiences a net momentum transfer of $\hbar\mathbf{k}$ per scattering event. This process gives rise to the so-called radiation pressure force, a fundamental dissipative mechanism underlying laser cooling. For a two-level atom illuminated by a monochromatic plane wave, the average photon scattering rate, i.e. the rate at which the atom absorbs and emits photons, is given by:

$$\Gamma_{\mathrm{sc}} = \frac{\Gamma}{2}\frac{s}{1 + s + (2\Delta/\Gamma)^2} \tag{2.3}$$

where Γ is the natural linewidth of the atomic transition, $\Delta = \omega_L - \omega_0$ is the detuning between the laser frequency and the atomic resonance frequency, and $s = I/I_{\mathrm{sat}}$ is the saturation parameter, defined as the ratio between the laser intensity I and the saturation intensity of the transition: $I_{\mathrm{sat}} = \frac{2\pi\hbar\Gamma c}{3\lambda^3}$, where $\hbar$ is the reduced Plank constant and c is the speed of light. The resulting radiation pressure force acting on the atom is therefore:

$$\mathbf{F}_{\mathrm{rad}} = \hbar\mathbf{k}\Gamma_{\mathrm{sc}} \tag{2.4}$$

The scattering rate can reach its maximum $\Gamma_{\mathrm{sc}} = \frac{\Gamma}{2}$ for $\Delta = 0$ and $s \gg 1$. This represents a fundamental physical limit: and explains why transitions with a large natural linewidth Γ are particularly suitable for manipulating atoms with high velocities.

2.3 Doppler and Zeeman effect

The effective detuning experienced by an atom can be evaluated by exploiting its velocity-dependent Doppler shift. For an atom moving with velocity $\mathbf{v}$ and interacting with a laser field of frequency ω_L and wave vector $\mathbf{k}$, the frequency of the light in the atom's rest frame is given by

$$\omega' = \omega_L - \mathbf{k}\cdot\mathbf{v} \tag{2.5}$$

Consequently, the effective detuning becomes

$$\Delta = \omega' - \omega_0 = \omega_L - \mathbf{k}\cdot\mathbf{v} - \omega_0 \tag{2.6}$$

Substituting this expression into Eq. 2.3 yields the Doppler-shifted scattering rate. When the atom and the laser beam propagate in opposite directions ($\mathbf{k} \cdot \mathbf{v} < 0$), to achieve the condition of maximum scattering ($\Delta = 0$), the laser frequency must therefore be set slightly below the atomic resonance (red detuning). Instead, if the atom moves in the same direction as the laser beam ($\mathbf{k} \cdot \mathbf{v} > 0$), the laser frequency must be tuned above resonance (blue detuning) to compensate for the Doppler shift and restore the resonant condition.

A typical atomic source for cold atom experiments consists of an atomic beam produced by heating a solid sample in an oven. The atoms come out from the hot reservoir, forming a directed beam with a broad, non-thermal velocity distribution. To decelerate the atoms, we exploit the radiation pressure from a counter-propagating laser beam as shown in Fig. 2.1.

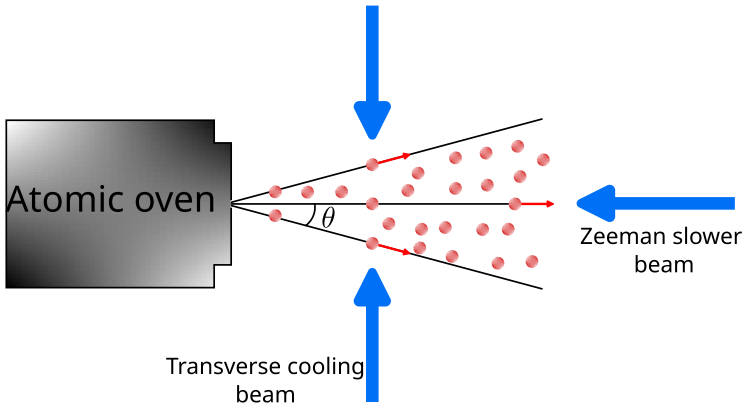

Figure 2.1. Schematic representation of the Zeeman slower and transverse cooling mechanism. Atoms emitted from the thermal oven form an effusive atomic beam with divergence θ. A counter-propagating laser beam (Zeeman slower beam) decelerates the atoms along the longitudinal axis, while transverse cooling beams reduce the atomic divergence, increasing the flux of slow atoms reaching the trapping region.

The radiation pressure force acting on an atom is given by Eq. 2.4. Due to the Doppler effect, the detuning experienced by an atom moving with velocity v_0 along the propagation axis of the atomic beam becomes

$$\Delta = \omega_L - \omega_0 - kv_0 \tag{2.7}$$

The scattering force reaches its maximum magnitude when the laser is resonant with the atomic transition in the atom's rest frame, i.e. when $\Delta = 0$, leading to the resonance condition:

$$\omega_L - \omega_0 = -kv_0 \tag{2.8}$$

The Doppler effect modifies the detuning experienced by a moving atom and therefore plays a key role in determining the efficiency of laser cooling.

Another important phenomenon that affects the resonance condition of atomic transitions is the Zeeman effect, which arises from the interaction between the atomic magnetic moment and an external magnetic field $\mathbf{B}$. The Zeeman interaction Hamiltonian can be written as

$$H_z = -\boldsymbol{\mu} \cdot \mathbf{B} \tag{2.9}$$

where the total magnetic dipole moment $\boldsymbol{\mu}$ is given by

$$\boldsymbol{\mu} = -\frac{\mu_b}{\hbar}\left(g_L\hat{\mathbf{L}} + g_S\hat{\mathbf{S}}\right) + \frac{\mu_N}{\hbar}g_I\hat{\mathbf{I}} \tag{2.10}$$

Here, $\hat{\mathbf{L}}$, $\hat{\mathbf{S}}$, and $\hat{\mathbf{I}}$ denote the orbital, spin, and nuclear angular momentum operators, respectively, while μ_B and μ_N are the Bohr and nuclear magnetons, and g_L, g_S and g_I are the corresponding Landé factors. For a magnetic field applied along the z axis, the Zeeman Hamiltonian takes the scalar form

$$\hat{H}_z^{(z)} = \frac{\mu_B B}{\hbar}(g_L\hat{L}_z + g_S\hat{S}_z) - \frac{\mu_N B}{\hbar}g_I\hat{I}_z = \frac{\mu_B B}{\hbar}(g_J\hat{J}_z) - \frac{\mu_N B}{\hbar}g_I\hat{I}_z \tag{2.11}$$

where $J_z = L_z + S_z$ is the total electronic angular momentum and g_J is the Landé factor defined as

$$g_J = \frac{g_L[J(J+1) + L(L+1) - S(S+1)] + g_S[J(J+1) - L(L+1) + S(S+1)]}{2J + (J+1)} \tag{2.12}$$

For bosonic isotopes of strontium, ^{88}Sr and ^{86}Sr, the nuclear spin is zero, so the nuclear term can be neglected and only the electronic contribution remains. This is not the case for the fermionic isotope ^{87}Sr, where $I = 9/2$, or for other atoms with non-zero hyperfine structure.
The Zeeman interaction leads to a shift of the atomic energy levels proportional to the magnetic field strength and the magnetic quantum number m_J, resulting in a linear splitting of the Zeeman sublevels m_J:

$$\Delta E = \mu_B B g_J m_J \tag{2.13}$$

2.4 Transverse cooling

Atoms emerging from an atomic oven form a directed beam with a broad velocity distribution and a finite angular divergence. The angular spread originates from the thermal motion of atoms inside the oven, which causes them to exit with different transverse velocity components relative to the mean propagation direction. To reduce this divergence and improve the beam collimation, transverse laser cooling can be applied. In this technique, two counter-propagating laser beams are aligned along a direction orthogonal to the atomic beam propagation (for instance, along the x-axis) as shown in Fig. 2.1. Their radiation pressure generates a velocity-dependent force that damps the transverse motion of the atoms. Considering an atom moving at an angle θ with respect to the mean propagation direction, in the atomic reference frame the radiation pressure force, derived from Eqs. 2.4 and 2.3, is expressed as

$$F_x = \frac{\Gamma}{2}\hbar k\left[-\frac{s}{1+s+4\frac{(\Delta+kv\sin(\theta))^2}{\Gamma^2}} + \frac{s}{1+s+4\frac{(\Delta-kv\sin(\theta))^2}{\Gamma^2}}\right] \tag{2.14}$$

where k is the laser wavenumber and Δ is the laser detuning in the laboratory frame. Transverse cooling affects only the velocity components orthogonal to the

mean propagation, $v\sin(\theta)$. When $\theta > 0$, the Doppler term $kv\sin(\theta)$ is positive. By selecting a red detuning ($\Delta < 0$), the term $(\Delta + kv\sin(\theta))^2$ in the first denominator becomes smaller than the corresponding term in the second denominator, producing an imbalance between the two counter-propagating beams. This asymmetry generates a net damping force that pushes the atoms back toward $\theta = 0$, thereby reducing the angular divergence of the atomic beam. In our experimental implementation, this mechanism is also employed to deflect the atomic beam emerging from the oven by an angle $\theta_d = 20°$. Two nearly orthogonal laser beams, retroreflected by in-vacuum optics (see Sec. 6.1), form an unbalanced cooling configuration that introduces a controlled angular deviation of the mean atomic trajectory. The retroreflected beams are only partially reflected, leading to different optical powers along the two propagation directions.

2.5 Zeeman slower

Atoms coming out of from an oven source must be decelerated before they can be captured in subsequent stages of the experiment. A widely used technique in ultracold atom experiments combines the Doppler effect and the Zeeman effect to slow an atomic beam from hundreds of meters per second down to a few tens of meters per second, effectively reducing the mean kinetic energy per atom.
Consider an atomic beam propagating along the positive y-axis and a counter-propagating laser beam along the negative y-direction ($-\mathbf{k}\cdot\mathbf{v} = \mathrm{kv}$), in the presence of a magnetic field oriented along the y-axis. Combining Eqs. 2.4 and 2.3, the resulting radiation pressure force along the beam axis is:

$$F_y = -\frac{\Gamma}{2}\hbar k \frac{s}{1 + s + 4\frac{\left(\Delta + \left(\frac{m'_J g'_J \mu_B B_y}{\hbar} - \frac{m_J g_J \mu_B B_y}{\hbar}\right) + kv\right)^2}{\Gamma^2}} \tag{2.15}$$

Here, m_J and g_J denote the magnetic quantum number and the Landé g-factor of the ground state, while m'_J and g'_J correspond to those of the excited state. The difference between the Zeeman shifts of the two states, proportional to $(m'_J g'_J - m_J g_J)\,\mu_B B_y$, determines the effective detuning of the transition in the presence of the magnetic field. The saturation parameter s is approximately constant for a well-collimated laser beam. To compensate for the decreasing Doppler shift as the atoms slow down, a spatially varying magnetic field $B_y(y)$ is applied along the propagation axis. A common design choice is to impose a constant deceleration a, which requires a constant scattering rate, i.e. the detuning in the atom's frame must remain constant:

$$\Delta_{\text{atom frame}} = \Delta_+ B_y(y)\left(\frac{m'_J g'_J \mu_B}{\hbar} - \frac{m_J g_J \mu_B}{\hbar}\right) + k_v(y) = \text{const.} \tag{2.16}$$

Maximizing the scattering rate corresponds to set this detuning to zero:

$$-\Delta = B_y(y)\left(\frac{m'_J g'_J \mu_B}{\hbar} - \frac{m_J g_J \mu_B}{\hbar}\right) + kv(y) \tag{2.17}$$

By defining $\xi_y = \left(\frac{m'_J g'_J \mu_B}{\hbar} - \frac{m_J g_J \mu_B}{\hbar}\right)$ the spatial profile of the magnetic field that satisfies this condition is

$$B_y(y) = -\frac{\Delta}{\xi_y} - \frac{k}{\xi_y}\sqrt{v_0^2 + 2ay} \tag{2.18}$$

where v_0 is the initial atomic velocity. The maximum achievable deceleration for a transition of linewidth Γ is $a_{\max} = -\frac{\Gamma\hbar k}{2M}$, which scales with Γ, making broad atomic transitions preferable for efficient Zeeman slowing. For the blue transition of strontium ($\Gamma/2\pi = 32\,\mathrm{MHz}$) the maximum deceleration is $a_{\max} = 10^6\,\mathrm{m\,s^{-2}}$, which requires a length $L = 10\,\mathrm{cm}$ to slow atoms from $v_0 \approx 450\,\mathrm{m\,s^{-1}}$ to rest.

A typical Zeeman slower is realized using a solenoid composed of concentric coils with a varying number of turns along the atomic beam axis. In our experiment, a commercial atomic source (see Sec. 6.1) is provided with a set of permanent magnets approximately 5 cm long to generate the Zeeman slower field. This represents a non-optimal practical compromise solution and the exact field profile is not disclosed due to patent restrictions. The maximum initial velocity that can be slowed to a few tens of $\mathrm{m\,s^{-1}}$ over a 5 cm interaction region is about $320\,\mathrm{m\,s^{-1}}$, even considering $s \gg 1$. Moreover, the assumption of a constant saturation parameter s does not strictly hold, since the manufacturer recommends a slightly focused slowing laser beam to optimize performance. This produces a position-dependent radiation pressure force, which is stronger where the laser intensity is higher.

2.6 Magneto-Optical Traps (MOTs): principles and configurations

Atoms slowed by a Zeeman slower still possess residual kinetic energy and a finite spatial and velocity distribution. To confine and further cool these atoms for precision experiments, a Magneto-Optical Trap (MOT) is employed. A MOT combines counter-propagating, red-detuned laser beams with a spatially varying magnetic field to produce both a velocity-dependent damping force (cooling) and a position-dependent restoring force (trapping). This allows atoms to be simultaneously cooled and trapped near the trap center, forming a dense, ultracold sample suitable for subsequent experimental manipulation.
In most experiments, a 3D MOT configuration is used, where three orthogonal pairs of counter-propagating laser beams provide cooling along all spatial dimensions, while a quadrupole magnetic field centered at the beam intersection ensures spatial confinement.

The atomic motion can be analyzed independently along the Cartesian axes by solving the corresponding scalar equations. The quadrupole field is typically generated using two coils in an anti-Helmholtz configuration (coaxial circular coils with the same current flowing in opposite directions). The resulting magnetic field takes the form $\mathbf{B} = \frac{b}{2}[-x, -y, 2z]$, where b is the magnetic field gradient along z (we assume $b > 0$). The factor two and the opposite sign in the z-component arise from Maxwell's condition $\nabla \cdot \mathbf{B} = 0$. Apart from these amplitude and sign differences, the three spatial directions can be treated equivalently.
We consider optical transitions from a ground state with total angular momentum

$J = 0$ to an excited state with $J = 1$, as is the case for the cooling transitions used in both the blue and red MOTs of ^{88}Sr. When the quadrupole magnetic field is applied, the energies of the excited-state Zeeman sublevels $|J' = 1, m_{J'} = \pm 1, 0\rangle$ shift linearly with the local magnetic field, as shown in Fig. 2.2. The ground state $|J = 0\rangle$ remains unshifted since it has no magnetic moment. The two counter-propagating beams along the z-axis must be circularly polarized with opposite helicities, so that one drives σ^+ transitions ($\Delta m_J = +1$) and the other drives σ^- transitions ($\Delta m_J = -1$). Because of the Zeeman effect, atoms displaced from the trap center experience a local shift in resonance frequency that depends on position. For $z > 0$, where $B_z > 0$, the $m_{J'} = -1$ sublevel is shifted down in energy, bringing the σ^- beam (propagating toward $-z$) closer to resonance. Conversely, for $z < 0$, the effect of the σ^+ beam becomes dominant. This asymmetry in scattering rates between the two circular polarizations produces a restoring force that pushes atoms back toward the magnetic-field zero at the trap center. Together with the Doppler-dependent frictional force from the red-detuned light, this mechanism yields both spatial confinement and velocity damping.

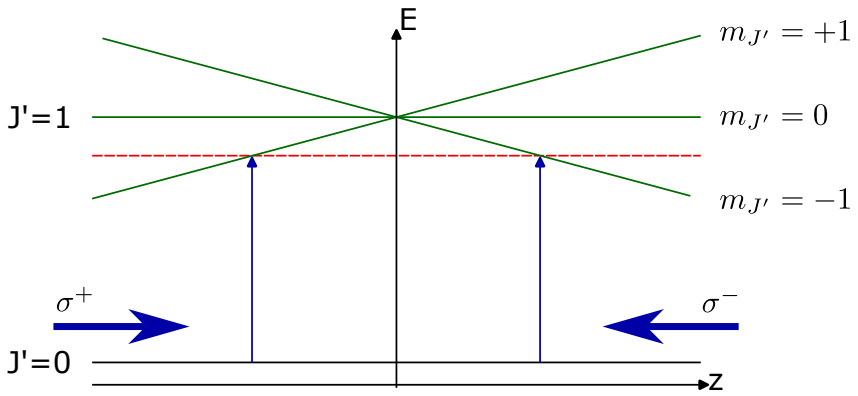

Figure 2.2. Zeeman splitting of the excited state $J' = 1$ in the presence of a magnetic field gradient. Two counter-propagating circularly polarized beams drive σ^+ and σ^- transitions from the ground state $J = 0$. The differential Zeeman shifts make one beam closer to resonance depending on the atomic position, generating a restoring force toward the magnetic-field zero.

The radiation pressure force along the z-axis has two contributions from the counter-propagating laser beams and can be expressed as

$$F_z = \frac{\hbar k \Gamma}{2} \left[\frac{s}{1 + s + 4(\Delta - \delta_Z - kv)^2/\Gamma^2} - \frac{s}{1 + s + 4(\Delta + \delta_Z + kv)^2/\Gamma^2} \right] \quad (2.19)$$

$$\text{with} \qquad \delta_Z = \frac{(m'_J g'_J)\, \mu_B b_z}{\hbar}.$$

For small velocities ($kv \ll \Gamma$) and small displacements ($\frac{m'_J g'_J \mu_B b z}{\hbar} \ll \Gamma$) this expression can be linearized as

$$F_z(v, z) \simeq -\alpha v - \kappa z, \quad (2.20)$$

where the damping and restoring coefficients are

$$\alpha = 8\hbar k^2 \frac{I/I_s}{[1 + s + 4\Delta^2/\Gamma^2]^2} \frac{|\Delta|}{\Gamma}, \qquad \kappa = \alpha \frac{g_J m_J \mu_B b}{\hbar k}. \quad (2.21)$$

This describes a damped harmonic oscillator, governed by

$$\frac{d^2z}{dt^2} + \gamma\frac{dz}{dt} + \omega_{\text{trap}}^2 z = 0 \tag{2.22}$$

where $\gamma = \frac{\alpha}{M}$ and $\omega_{\text{trap}} = \sqrt{\frac{\kappa}{M}}$, with M denoting the atomic mass. The MOT parameters can be tuned to optimize various characteristics such as atom number, density or capture velocity range depending on experimental priorities.
Because atoms continuously absorb and spontaneously re-emit photons, their motion exhibits a random walk, setting a lower bound on the achievable kinetic energy and, thus, final temperature. The Doppler cooling limit is given by

$$k_B T_D = \frac{\hbar\Gamma}{4}\frac{1+\left(\frac{2\Delta}{\Gamma}\right)^2}{\frac{2|\Delta|}{\Gamma}}, \tag{2.23}$$

where Δ is the laser detuning from resonance and Γ is the natural linewidth of the optical transition. The minimum Doppler temperature occurs for $\Delta = -\Gamma/2$:

$$T_D^{\text{min}} = \frac{\hbar\Gamma}{2k_B}. \tag{2.24}$$

The Doppler limit scales with the linewidth: the broad "blue" transition of Strontium has $\Gamma/2\pi \simeq 32\,\text{MHz}$ yielding $T_D^{\text{min}} \simeq 720\,\mu\text{K}$, whereas the narrow "red" transition with $\Gamma/2\pi \simeq 7.6\,\text{kHz}$ allows $T_D^{\text{min}} \simeq 180\,\text{nK}$. This hierarchy of transitions is a defining feature of the Strontium platform. While the broad blue transition provides the high scattering rates needed for efficient initial capture, the second-stage MOT on the narrow intercombination line is a physical necessity for tweezer loading. Indeed, the Doppler limit of the blue transition significantly exceeds the typical depths of our optical tweezers ($U_{\text{trap}} \approx 360\,\mu\text{K}$, see Chap. 8), making direct loading from a blue MOT practically impossible. The red MOT stage thus acts as a crucial bridge, compressing the cloud and cooling the atoms to the μK regime. This ensures that the atomic sample is well-matched to the conservative potential of the tweezers, achieving the high phase-space density required for reliable single-atom capture.

2.7 Far off-resonant atom-light interaction

We now introduce key theoretical aspects of atom-light interaction in the far off-resonant regime, which is crucial for understanding optical trapping with optical tweezers. In this context, the interaction between an atom and an oscillating electromagnetic field gives rise to what is commonly known as the optical dipole potential, also referred to as the light shift or the AC Stark shift [42, 43, 44]. This configuration creates a conservative potential capable of trapping neutral atoms.
The optical dipole potential generated by a far off-resonant laser beam can be expressed as [45]:

$$U(r,z) = -\frac{1}{2\varepsilon_0 c} I(r,z)\alpha(\lambda_L) \tag{2.25}$$

where ε_0 is the vacuum permittivity, c is the speed of light, $I(r,z)$ is the local intensity of the laser field at transverse position r and axial position z and $\alpha(\lambda_L)$ is the polarizability of the atomic state at the laser wavelength λ_L.
For a focused Gaussian beam, in the following called optical tweezer, the intensity profile is given by:

$$I(r,z) = \frac{2P_L}{\pi w^2(z)} e^{-\frac{2r^2}{w^2(z)}} \tag{2.26}$$

where P_L is the laser power and $w(z)$ is the beam radius ($\frac{1}{e^2}$ intensity) at position z. Substituting this into the expression for the potential Eq. 2.25 yields:

$$U(r,z) = -\frac{2P_L}{\varepsilon_0 c\pi w^2(z)} \alpha(\lambda_L) e^{-\frac{2r^2}{w^2(z)}} \tag{2.27}$$

The beam radius $w(z)$ varies along the propagation axis and reaches its minimum value w_0 at the beam waist $z = 0$. Its axial dependence is described by:

$$w(z) = w_0 \sqrt{1 + \left(\frac{z}{z_R}\right)^2} \tag{2.28}$$

where $z_R = \frac{\pi w_0^2}{\lambda_L}$ is the Rayleigh length, which defines the characteristic scale over which the beam diverges.
If the light is red-detuned ($\omega_L < \omega_0$) $\alpha(\lambda_L) > 0$ and Eq. 2.27 describes a potential well, two important parameters in experiments with optical dipole traps are the trap depth and the trap frequencies. The trap depth is defined as the maximum absolute value of the dipole potential from Eq. 2.27, which occurs at the center of the trap (at $r = 0$, $z = 0$):

$$U_0 = \frac{P_L}{\varepsilon_0 c\pi w_0^2} \alpha(\lambda_L) \tag{2.29}$$

The trap depth provides an upper bound for the energy (or temperature) of atoms that can be confined in the optical potential. In the regime where the trap depth is much greater (typically by several orders of magnitude) than the atomic thermal energy, the potential can be approximated as harmonic near the trap center.
To derive the trap frequencies, we expand the Gaussian intensity profile around the trap center. A second-order Taylor expansion of the exponential in Eq. 2.27 for small radial displacements at $z = 0$ gives:

$$e^{-\frac{2r^2}{w_0^2}} \approx 1 - \frac{2r^2}{w_0^2} \tag{2.30}$$

Substituting this into Eq. 2.27 yields a harmonic approximation (HO) of the dipole potential:

$$U_{\mathrm{HO}}(r,0) = -\frac{P_L}{\varepsilon c\pi w_0^2} \alpha(\lambda_L) \left(1 - \frac{2r^2}{w_0^2}\right) = -U_0 + \frac{2P_L \alpha(\lambda_L)}{\varepsilon c\pi w_0^4} r^2 \tag{2.31}$$

From Eq. 2.31 we can extract the radial trap frequency $\omega_{\mathrm{HO},r}$ by equating the potential to that of a harmonic oscillator:

$$\frac{1}{2} M \omega_{\mathrm{HO},r}^2 r^2 = \frac{2P_L \alpha(\lambda_L)}{\varepsilon c\pi w_0^4} r^2 \tag{2.32}$$

Solving for $\omega_{\mathrm{HO},r}$:

$$\omega_{\mathrm{HO},r} = \sqrt{\frac{4P_L\alpha(\lambda_L)}{M\varepsilon c\pi w_0^4}} \tag{2.33}$$

As in the radial case, the axial potential near the trap center can be approximated as a harmonic oscillator by expanding Eq. 2.27 in a Taylor series along z, keeping $r = 0$. This yields a constant term corresponding to the trap depth, plus a term quadratic in the axial coordinate z.

$$U(0,z) = -\frac{P_L}{\varepsilon c\pi w_0^2\left(1+\left(\frac{z}{z_R}\right)^2\right)}\alpha(\lambda_L) \approx -U_0 + \frac{P_L\alpha(\lambda_L)}{\varepsilon c\pi w_0^2 z_R^2}z^2 \tag{2.34}$$

By equating this quadratic term with the potential of a harmonic oscillator along z we obtain:

$$\frac{1}{2}M\omega_{\mathrm{HO},z}^2 z^2 = \frac{P_L\alpha(\lambda_L)}{\varepsilon c\pi w_0^2 z_R^2}z^2 \tag{2.35}$$

Solving for the axial angular frequency:

$$\omega_{\mathrm{HO},z} = \sqrt{\frac{2P_L\alpha(\lambda_L)}{M\varepsilon c\pi w_0^2 z_R^2}} \tag{2.36}$$

It is important to note that both the trap depth and the trap frequencies depend strongly on the parameters of the optical tweezers. The trap depth scales linearly with the optical power and inversely with the square of the waist, while the trap frequencies scale with the square root of the power and, again, inversely with the square of the waist. In the axial direction, the Rayleigh length introduces an additional dependence, but since $z_R \propto w_0^2$, the overall frequency scaling still follows an inverse cubic dependence on the waist. These scaling properties enable the use of micrometer-sized optical tweezers to generate deep traps with only a few mW of power per site, a key feature for extending the system to large arrays.

2.7.1 Atomic polarizability

The optical dipole potential can act either as a trapping or repulsive force for an atom, depending on the atom's internal structure and the sign of its polarizability. In general, the light shift produced by the interaction is maximal in magnitude where the laser intensity is highest. If this shift lowers the energy of the atomic state, the atom is attracted toward the region of highest intensity and experiences a confining potential. In contrast, if the shift raises the energy of the state, the atom is repelled from the light field and experiences an anti-trapping effect.

Computing the polarizability $\alpha(\lambda_L)$ for an off-resonant trapping wavelength λ_L can be non-trivial, especially since the two-level approximation often breaks down in realistic atomic systems. When the laser is detuned far from multiple transitions, the total polarizability must account for contributions from all relevant excited states. In such cases, an useful expression for the dynamic polarizability of an electronic state i is given by [46]:

$$\alpha_i(\omega_L) = \sum_k \frac{6\pi\varepsilon_0}{\omega_{ik}}\frac{A_{ik}}{\omega_{ik}^2 - \omega_L^2} \tag{2.37}$$

where $\omega_L = \frac{2\pi c}{\lambda_L}$ is the angular frequency of the trapping laser, A_{ik} are the Einstein A coefficients (proportional to the square of the dipole matrix elements), and ω_{ik} are the transition frequencies between the initial state i and the excited states k. Polarizabilities generally depend on the polarization of the trapping light, as well as on the atomic fine and hyperfine structures. Moreover, external magnetic fields may influence polarizability by shifting magnetic sublevels with non-zero magnetic moments. For detailed computational methods and tabulated values, see Refs.[47, 48, 49]. In particular, Ref. [49] provides a comprehensive approach to include fine and hyperfine interactions and Zeeman effects in the calculation of polarizabilities for Strontium atoms.

A key concept in optical trapping is the magic wavelength condition. This occurs when two atomic levels exhibit identical polarizabilities at a specific wavelength λ_{magic}, resulting in equal energy shifts for both states. At this wavelength, the differential light shift vanishes, ensuring that the transition frequency between the two levels remains unperturbed by the trapping field regardless of intensity. This condition is essential for precision platforms such as optical atomic clocks to prevent dephasing; In non-magic traps, fluctuation in laser power or pointing stability translate directly into frequency noise, degrading coherence.
Strontium, in particular, exhibits a magic wavelength at $\lambda_{\text{magic}} = 813.4\,\text{nm}$ for the clock transition ${}^1\text{S}_0 \rightarrow {}^3\text{P}_0$. This value lies conveniently in the infrared range, where high-power Ti:Sapphire lasers are readily available. Calculated polarizability values for key Strontium states at $\lambda_{\text{magic}} = 813.4\,\text{nm}$ can be found in Ref. [48] and are summarized in Tab. 2.1.

State	$\lvert m_J^x \rvert$	**Polarizability (a.u.)**
$5s^2\,{}^1\text{S}_0$	0	286
$5s5p\,{}^3\text{P}_0$	0	286
$5s5p\,{}^3\text{P}_1$	0	195.1
	1	353.9
$5s5p\,{}^3\text{P}_2$	0	464.3
	1	391.6
	2	173.8
$5s4d\,{}^1\text{D}_2$	0	256.8
	1	522.2
	2	1318
$5s5p\,{}^1\text{P}_1$	0	178.4
	1	737.8
$5s6s\,{}^3\text{S}_1$	0	−494.1
	1	−481.9

Table 2.1. Summary of polarizabilities of Strontium at $\lambda_{\text{magic}} = 813.4\,\text{nm}$, considering a linear polarization along $\hat{x}$, and zero magnetic field. Taken from Ref. [48]

2.7.2 Sisyphus cooling

For atoms confined in optical dipole traps or optical tweezers, the dynamics differ significantly from those in a MOT. The atoms experience an intensity and polarization dependent optical potential rather than a radiative pressure force. In this regime, the Doppler limit no longer represents the ultimate temperature bound. Here the atomic motion occurs in the optical potential of tightly focused and polarized light fields, and additional cooling mechanisms become relevant.

Cooling the atom to its motional ground state within the trap is essential for minimizing position uncertainty, crucial for coherent Rydberg interactions and for maintaining confinement during fluorescence imaging protocols, where photon scattering can lead to heating and atom loss.

Among the cooling methods suitable for optical tweezers, the two most relevant are sideband cooling [50, 51, 52] and Sisyphus cooling [53, 54, 55, 56]. Sideband cooling can be implemented in a magic trap, where the optical potentials for the ground and excited states, U_g and U_e, are identical. In contrast, Sisyphus cooling operates in non-magic traps, where $U_g \neq U_e$, and remains effective in both configurations where the excited state is more tightly confined than the ground state ($U_e > U_g$) or vice versa ($U_e < U_g$).
In our experiment, the optical tweezers at 813.4 nm create a non-magic potential for the $^1\mathrm{S}_0 \rightarrow ^3\mathrm{P}_1$ transition. We implement attractive Sisyphus cooling using circularly polarized light to address the $m_J = 1$ sublevels. While 813.4 nm is the magic wavelength for the clock transition, it intentionally creates a large differential light shift for the $^1\mathrm{S}_0 \rightarrow ^3\mathrm{P}_1$ cooling transition. This non-magic configuration is a key requirement for Sisyphus cooling, as it provides the necessary spatial dependence of the resonance condition within the micro-trap.

The basic idea of attractive Sisyphus cooling is illustrated schematically in Fig. 2.3. In a classical picture, the atom oscillates around the center of the optical potential, and the cooling laser is tuned to be resonant with the transition only at the bottom of the trap, where the detuning compensates for the local differential light shift $U_e - U_g$. As the atom moves within the trap, it can absorb a photon near the potential minimum and be excited to the upper potential U_e, which is more tightly confining. The atom then moves toward the outer region of the trap with higher potential energy. After a time determined by the excited-state lifetime, the atom spontaneously decays back to the ground state U_g, emitting a photon at a higher energy than the absorbed one. The difference in photon energies corresponds to a net loss of kinetic energy, thus cooling the atom. Through many such cycles, the atom's motional energy is reduced, approaching the ground-state energy of the trap.

A similar mechanism can occur in repulsive Sisyphus cooling, where $U_e < U_g$. In that case, the atom absorbs a photon when it is displaced from the trap center and loses energy while descending the potential hill associated with the ground-state potential before being optically pumped back to the lower potential.
Remarkably, the non-magic confinement results in non-orthogonal harmonic oscillator states for $|g\rangle$ and $|e\rangle$ in both the radial and axial directions when the motion of the atoms is treated quantum-mechanically. This allows a single cooling beam to remove energy from all motional degrees of freedom simultaneously [53, 55].

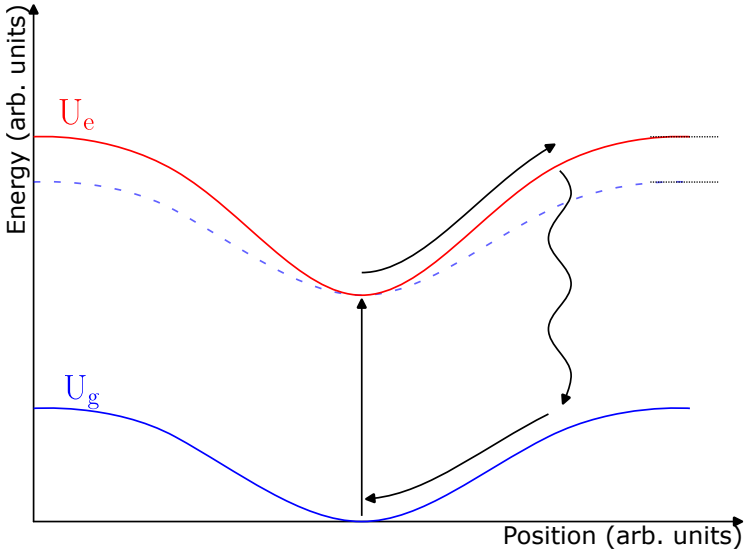

Figure 2.3. Schematic representation of the optical potentials for the ground (U_g) and excited (U_e) states in a non-magic optical trap. The atom absorbs a photon near the trap minimum, climbs the steeper excited-state potential, and then spontaneously decays to the ground state, losing kinetic energy in each cycle.

Chapter 3

The Strontium atom

The atomic structure of Strontium offers a unique combination of transitions with widely different natural linewidths, ranging from broad dipole-allowed lines to ultra-narrow intercombination and clock transitions. This allows for highly efficient cooling at various stages, precise coherent manipulation, and long coherence times. In addition, the availability of both singlet and triplet manifolds offers multiple excitation pathways, including routes to Rydberg states that are essential for engineering strong, controllable interactions between atoms.

In this chapter, we provide an overview of the atomic properties of Strontium that are most relevant to its use in our experiment. We begin with an illustration of its electronic level structure and the key transitions used for laser cooling and detection, followed by a discussion of the ultra-narrow clock transition and the excitation schemes to Rydberg states.

3.1 Electronic structure and level diagram

v

Isotope	Natural abundance	Statistics	Nuclear spin
^{84}Sr	0.56%	bosonic	0
^{86}Sr	9.86%	bosonic	0
^{87}Sr	7%	fermionic	$\frac{9}{2}$
^{88}Sr	82.58%	bosonic	0

Table 3.1. Properties of stables isotopes of Strontium [58].

Strontium is an atom with two valence electrons, a feature it shares with all alkaline-earth elements (Be, Mg, Ca, Sr, Ba, Ra). This configuration, however, is not unique to this group: Helium represents the simplest two-electron system, while Ytterbium is another atom with two valence electrons that has been widely used in recent years for experiments closely related to the ones presented in this work [59]. One of the most relevant properties of Strontium for our purposes is its level structure and the set of electronic transitions it offers, illustrated in simplified form in Fig. 3.1.
The two-valence-electron structure gives rise to a rich spectrum of singlet and triplet states. Particularly relevant to this work are the ground state $^1S_0$, the excited states

$^3P_0$, $^3P_1$, and $^1P_1$, as well as Rydberg levels in which one electron is promoted to a state with high principal quantum number n. The $^1S_0 \leftrightarrow {}^3P_0$ "clock" transition is ultra-narrow and underpins both optical atomic clocks and qubit implementations.

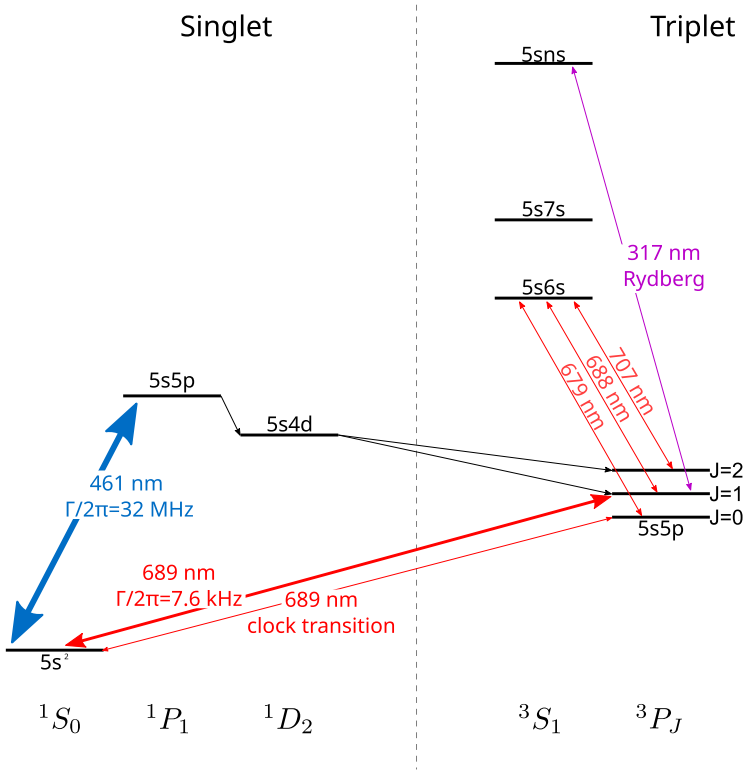

Figure 3.1. Simplified energy scheme for ^{88}Sr, with transitions of interest shown.

3.2 Relevant transitions for cooling and detection

Blue Transition The blue transition $5s^2\,{}^1\mathrm{S}_0 \leftrightarrow 5s5p\,{}^1\mathrm{P}_1$ has a wavelength of $\lambda = 460.9\,\mathrm{nm}$ and a natural linewidth of $\Gamma/2\pi = 32\,\mathrm{MHz}$ with a lifetime $\tau \sim 5.3\,\mathrm{ns}$ [60]. This transition plays a central role in the manipulation of Strontium atoms. Its broad linewidth makes it ideal for decelerating the atomic beam at early stages, both in the Zeeman slower and in the 2D MOT, where it efficiently reduces the atoms' kinetic energy before they arrive into the main trapping region. This transition is also employed in the operation of the first stage of the 3D MOT (see Sec. 7.3), where it provides strong cooling and confinement forces. It is also used for absorption imaging of the MOT and for fluorescence detection of single atoms confined in optical tweezers (see Sec. 8.2). However, the transition is not perfectly closed: the excited $^1\mathrm{P}_1$ state can decay, with a small branching ratio, into the $5s4d\,{}^1\mathrm{D}_2$ state. This intermediate level then decays into the metastable $5s5p\,{}^3\mathrm{P}_1$ and $^3\mathrm{P}_2$ states, effectively removing atoms from the cooling cycle. This loss mechanism limits the efficiency of the blue MOT, as further discussed in Sec. 7.3.

Red Transition The red transition $5s^2\,{}^1\mathrm{S}_0 \leftrightarrow 5s5p\,{}^3\mathrm{P}_1$ has a wavelength of $\lambda = 689.4\,\mathrm{nm}$ and a natural linewidth of $\Gamma/2\pi = 7.6\,\mathrm{kHz}$ (corresponding to a lifetime of $\tau = 21\,\mu\mathrm{s}$) [61]. It is a narrow intercombination line connecting the ground state with the triplet ${}^3\mathrm{P}_1$ state. Due to its much narrower linewidth compared to the blue transition, this transition enables cooling to temperatures about three orders of magnitude lower, but does not scatter photons fast enough to directly trap a hot atomic beam in a red MOT. However, its linewidth can be artificially broadened using appropriate techniques, thereby increasing the MOT's capture range and enabling its use in a second-stage MOT. This stage allows for the preparation of colder and denser atomic clouds, as described in Sec. 7.4. Furthermore, the red transition plays a key role in in-tweezer cooling (see Sec. 4.5), and it can also be employed in high-resolution imaging schemes [62].

Repumpers Transition The dipole-allowed transitions $5s5p\,{}^3\mathrm{P}_J \leftrightarrow 5s6s\,{}^3\mathrm{S}_1$ play a crucial role in managing atomic population within the ${}^3\mathrm{P}_J$ manifold, particularly in experiments involving the blue MOT and imaging. These transitions occur at wavelengths $\lambda = 679.1\,\mathrm{nm}$ for the ${}^3\mathrm{P}_0 \leftrightarrow {}^3\mathrm{S}_1$ transition (with linewidth $\Gamma/2\pi = 1.4\,\mathrm{MHz}$, $\tau = 112\,\mathrm{ns}$), $\lambda = 687.8\,\mathrm{nm}$ for the ${}^3\mathrm{P}_1 \leftrightarrow {}^3\mathrm{S}_1$ transition ($\Gamma/2\pi = 4.3\,\mathrm{MHz}$, $\tau = 37\,\mathrm{ns}$), and $\lambda = 707.0\,\mathrm{nm}$ for the ${}^3\mathrm{P}_2 \leftrightarrow {}^3\mathrm{S}_1$ transition ($\Gamma/2\pi = 6.7\,\mathrm{MHz}$, $\tau = 24\,\mathrm{ns}$). These transitions are essential for repumping atoms that fall into long-lived metastable states as a result of decay from the $5s5p\,{}^1\mathrm{P}_1$ state during cooling or imaging via the blue transition. After decaying through weak channels, atoms accumulate in the ${}^3\mathrm{P}_2$ and ${}^3\mathrm{P}_1$ states. While atoms in the ${}^3\mathrm{P}_1$ state decay back to the ground state within a few microseconds, those in metastable ${}^3\mathrm{P}_2$ remain trapped in a dark state. To clear this dark population, a repump laser resonant with the 707 nm transition can be used. However, atoms excited to the ${}^3\mathrm{S}_1$ state from ${}^3\mathrm{P}_2$ can decay into any of the three ${}^3\mathrm{P}_J$ levels. Therefore, a second repump laser at 679 nm is required to deplete the population of the metastable ${}^3\mathrm{P}_0$ state as well.

3.3 Clock transition

The **clock transition** $5s^2\,{}^1\mathrm{S}_0 \leftrightarrow 5s5p\,{}^3\mathrm{P}_0$, at a wavelength of $\lambda = 698.4\,\mathrm{nm}$, is characterized by an extremely narrow natural linewidth, effectively $\Gamma \to 0$, in the bosonic isotopes of Sr (corresponding to $\tau \to \infty$, limited in practice only by an extremely weak two-photon $E1$–$M1$ decay channel towards ${}^1\mathrm{S}_0$ with a theoretical lifetime of the order of 10^3 years). This is due to the fact that the transition is doubly forbidden by selection rules $\Delta S = 0$ and $J = 0 \nrightarrow J = 1$. While the first selection rule is relaxed by fine-structure interaction mixing singlet and triplet states, the absence of hyperfine interaction in the bosonic isotopes of Sr (where the nuclear spin $I = 0$) makes the second selection rule strict. However, it is possible to coherently drive this transition by applying a strong external magnetic field ($B \sim 1000\,\mathrm{G}$), which induces a mixing of ${}^3\mathrm{P}_J$ states and opens the transition channel, as discussed in Sec. 6.2. Under these conditions, the effective linewidth scales as $\Gamma(B) \propto B^2$, while the Rabi frequency scales as $\Omega(B) \propto B\sqrt{I}$, where I is the intensity of the driving laser. In the fermionic isotope ${}^{87}\mathrm{Sr}$, where the nuclear spin is $I = 9/2$, the

hyperfine interaction naturally mixes electronic states. This results in a small but nonzero natural linewidth for the clock transition, without the need for an external magnetic field. The metastable $^3\mathrm{P}_0$ state plays a central role in atomic clocks and qubit implementations, and can also serve as an intermediate level for coherent excitation to Rydberg states (see Sec. 5.2).

3.4 Rydberg excitation transitions

The transitions $5s5p\,^3\mathrm{P}_0 \leftrightarrow 5sns\,^3\mathrm{S}_1$ (at $\lambda \sim 317\,\mathrm{nm}$) and $5s5p\,^3\mathrm{P}_1 \leftrightarrow 5sns\,^3\mathrm{S}_1$ (at $\lambda \sim 319\,\mathrm{nm}$) provide access to Rydberg states with $n \gg 1$ that are essential for enabling strong, long-range interactions between otherwise non-interacting neutral atoms. These interactions form the foundation for implementing quantum simulation and quantum computation protocols in this platform. As discussed in Sec. 5.2, the precise transition wavelength depends on the principal quantum number n of the targeted Rydberg level.

Chapter 4

Optical tweezers array and single-atom trapping

The ability to generate arrays of optical tweezers represents a key step toward scalable quantum simulation platforms: on the one hand, it requires precise control over the spatial structure of the trapping light, while on the other it demands reliable techniques to load, cool, and organize atoms within the traps.
It is necessary to shape laser beams into complex configurations and focus them through a high–numerical aperture objective, creating tightly localized trapping potentials. Achieving deterministic single-atom occupancy, also calls for careful control of the stochastic loading process, efficient laser cooling strategies, and methods to overcome the randomness of atom distribution by arranging the atoms into defect-free arrays.

4.1 Optical Tweezer

An optical tweezer is realized by tightly focusing a laser beam. This can be achieved with a simple lens or, more effectively, with a microscope objective. Since the trap operates on microscopic length scales, the optical system must be designed with great precision to minimize aberrations that could otherwise distort the potential. For this reason, diffraction-limited aberration-corrected microscope objectives are commonly employed. Compared to achromatic lenses, they generally provide superior performance and can be optimized for multiple wavelengths. This capability is essential, as it enables the objective not only to generate the optical tweezer but also to simultaneously collect the imaging light and produce site-resolved images of the trapped atoms (See Sec. 8.2).

A laser beam can be described as a Gaussian beam if the paraxial approximation holds, i.e. if the amplitude $A(\mathbf{r})$ of the electromagnetic wave traveling along the z-direction varies slowly compared to the wavelength λ [63]:

$$\frac{\partial A}{\partial z} \ll kA \tag{4.1}$$

where $k = \frac{2\pi}{\lambda}$ is the wave number. In the paraxial approximation the expression of

the electric field $E(r,z,t) = A(r,z)e^{i(\omega t - kz)}$ traveling along the z-axis is [63]:

$$A(r,z) = A_0 \frac{w_0}{w(z)} e^{-\frac{r^2}{w^2(z)}} e^{-ikz - ik\frac{r^2}{2R(z)} + i\zeta(z)} \tag{4.2}$$

where A_0 is the amplitude peak value, r is the radial coordinate, and w_0 is the beam waist, i.e. the minimum beam radius at the focal plane. The transverse beam radius evolves as:

$$w(z) = w_0 \sqrt{1 + \left(\frac{z}{z_R}\right)^2} \tag{4.3}$$

where $z_R = \frac{\pi w_0^2}{\lambda}$ is the Rayleigh length, defined as the distance along the propagation axis at which the beam area doubles (equivalently, the radius increases by a factor $\sqrt{2}$). $R(z) = z\left[1 + \left(\frac{z_R}{z}\right)^2\right]$ is the curvature radius of the wavefront, while $\zeta(z) = \arctan\left(\frac{z}{z_R}\right)$ denotes the Gouy phase.

However, the paraxial approximation begins to break down for a tightly focused laser beam, such as that in an optical tweezer, because the intensity varies over a distance on the order of the Rayleigh range z_R, which can be just a few microns, comparable to the laser wavelength. In Ref. [64] the limits of the paraxial approximation are investigated, introducing higher-order effects that lead to aberrations and providing a detailed description of different optical aberration effects.

Even when considering a system with no aberration, a focused laser beam will always have a finite size due to the diffraction limit, which arises from the diffraction induced by the finite size of the optical elements of the system.

How an imaging system represents a point-like source of light is described by the point spread function (PSF), which gives the spatial distribution of light in the image produced by that system for a single point source. If we consider an imaging system with no aberration and a circular aperture with a finite diameter $D = 2a$ the PSF is a diffraction pattern called Airy disk (Fig. 4.1), with an intensity profile given by [65]:

$$I(\theta) = I_0 \left(\frac{2J_1(ka\sin\theta)}{ka\sin\theta}\right)^2 \tag{4.4}$$

where $J_1(x)$ is the first-order Bessel function, k is the wave number and $\theta = \arctan\frac{w_0}{z_R}$ is the Gaussian beam divergence in the paraxial approximation.

The minimum spot size is conventionally defined as the distance between the central peak and the first minimum, which occurs at

$$ka\sin(\theta) \approx 1.22\pi \tag{4.5}$$

For a system with numerical aperture NA, we have:

$$NA = n\sin(\theta_{\max}) \tag{4.6}$$

where the maximum aperture angle of the lens or objective is $\theta_{\max} = \arctan\left(\frac{D}{2f}\right)$, f the focal length and n is the refractive index of the medium (in vacuum $n = 1$). Solving for the radius of the diffraction-limited spot in the image plane, we obtain:

$$a_0 = \frac{0.61\lambda}{\mathrm{NA}} \tag{4.7}$$

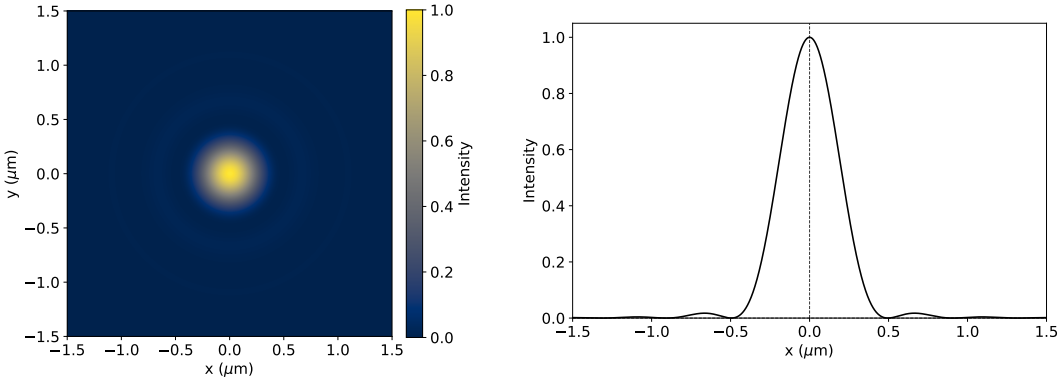

Figure 4.1. Airy disk profile in 2D and 1D. The intensity profile is characterized by a central peak surrounded by concentric fringes arising from the diffraction due to the finite aperture of the objective.

This sets the theoretical lower bound, however real systems have imperfections that might produce a larger PSF. The best resolution achievable in the real imaging system for a point source is defined as the distance r_0 between the Airy disk central peak and the first minimum. If $r_0 = a_0$ the system is said to be diffraction limited. This generally happens only at specific wavelengths for which the imaging system has been designed.
Having the smallest PSF possible is very important in our experiment to produce the tightest optical tweezer possible to have large trap depths and trapping frequencies, but also to have the highest resolution possible in the detection process. Our objective, described in Sec. 4.1.1, is designed to be diffraction limited at 813 nm (optical tweezers) and 461 nm (fluorescence imaging), the diffraction limit spots for this two wavelength are:

$$a_0(461\,\text{nm}) = 502\,\text{nm}, \qquad a_0(813\,\text{nm}) = 902\,\text{nm} \tag{4.8}$$

4.1.1 High-NA objective

The high-numerical-aperture microscope objective (NA = 0.55) employed in this experiment is a custom device manufactured by Special Optics. Its function is twofold: to generate the optical tweezer array by focusing the trapping laser at 813.4 nm, and to collect the fluorescence emitted by individual atoms. To this end, the objective is optimized across several wavelengths (461 nm, 689 nm, 698 nm, and 813 nm). In particular, it operates in the diffraction-limited regime at 461 nm, 698 nm, and 813 nm, with no focal shift between 461 nm and 813 nm, and only a $\sim 4\,\mu$m shift between the tweezer light and 689 nm. The objective features a working distance of 14 mm and is corrected for the 3.5 mm thickness of the fused-silica science cell. Its measured transmission is 92.6%, 94.8%, and 96.6% at 461 nm, 689 nm, and 813 nm, respectively. The housing is made of Ultem, a thermoplastic polymer with high dielectric strength, which has been blackened both internally and externally to suppress reflections. This choice of material also ensures reliable operation in an environment subject to magnetic fields on the order of several hundred Gauss. All the properties of the microscope objective can be found in Tab. 4.1.

Property	Value
NA	0.56 @461 nm, 0.55 @813 nm
Effective focal length (EFL)	24 mm @461 nm, 24.5 mm @813 nm
Aperture	27 mm
Field of view (FOV)	0.36 mm @813 nm, 0.24 mm @461 nm, 0.25 mm @689 nm
Working distance (WD)	9 mm vacuum + 3.5 mm fused silica + 1.5 mm air
Diffraction limited	461 nm and 813 nm
Transmission	92.6% @461 nm, 94.8% @689 nm, 96.6% @813 nm

Table 4.1. Microscope Objective Properties

The objective is mounted on a 5-axis assembly made combining a pitch and yaw platform (PY004/M from Thorlabs) that enables the tip and tilt control, a linear translation stage (L-509.44AD00 manufactured by PI) and a two-axes translating lens mount (CXY2 from Thorlabs) that allow control over the three spatial directions. The translation stage was chosen with a travel distance of 102 mm, which allows the objective to be completely extracted from the coil support structure surrounding the glass cell, which is convenient both during the alignment phase and in case in the future there is a need to remove it for changes or maintenance. The detailed description of the alignment procedure of the objective can be found at [66].

4.2 Optical tweezer arrays

The realization of optical tweezer arrays relies on the ability to tailor the spatial profile of a laser beam and project it onto the focal plane of a high–numerical aperture objective. Different strategies can be employed to split and shape the incoming light into multiple diffraction-limited spots, each acting as an individual trap for a single atom. Among the different possible approaches, two technologies have become the most widely used and are now fundamental tools in experiments with neutral atom arrays: acousto-optic deflectors (AODs) and spatial light modulators (SLMs). Both enable the generation of multiple traps from a single laser beam, but they rely on different physical mechanisms and offer complementary advantages.

4.2.1 Acousto-Optic Deflectors (AODs)

Acousto-Optic Deflectors (AODs) are optical devices that exploit the interaction between light and acoustic waves inside a crystal [67]. When a radiofrequency (RF) signal is applied to a piezoelectric transducer attached to the crystal, it generates an acoustic wave that propagates through the material. This acoustic wave periodically modulates the refractive index of the crystal, creating what can be regarded as a dynamic diffraction grating. An incident laser beam traversing this medium is then diffracted, and the deflection angle depends directly on the acoustic frequency applied to the crystal. The deflection angle θ of the first-order diffracted beam is

given by [68]:

$$\theta(\nu) = \frac{\lambda}{v}\nu \tag{4.9}$$

where λ is the wavelength of the light, v is the speed of sound in the crystal, and ν is the applied radio-frequency (RF) signal driving the acoustic transducer. This linear frequency-to-angle mapping allows precise control over the laser beam deflection by modulating the RF signal electronically [63]. Having no moving parts AODs are robust and highly reliable, while offering extremely fast scanning speeds with fine angular resolution.

The AODs that we employ in our experiment are manufactured by AA Opto-Electronics (DTSX-400-810 for $\lambda = 813\,\text{nm}$). They have a measured bandwidth of $\pm 20\,\text{MHz}$ around the central frequency $\nu_0 = 101\,\text{MHz}$. Using Eq. 4.9 is possible to calculate the angular separation between the zeroth and first order at the central frequency which turns out to be $\theta_0 = 0.13\,\text{rad} = 7.2°$.

By driving the AOD with multiple RF frequencies simultaneously, it is possible to generate multiple diffracted beams at different angles, whereas by driving the AOD with a time-dependent RF frequency, a single diffracted beam can be dynamically steered in time, producing either a scanning beam or, if scanned sufficiently fast, an effectively continuous distribution. In addition to beam deflection, AODs can also modulate beam intensity via RF amplitude, and perform rapid beam switching on sub-microsecond timescales.

Placing a scan lens at its focal length from the AOD will transform the angular separation of the beams in spatial separation (see Fig. 4.2 top). In this way every beam deflected by the AOD with a different angle will be focused in a different point of the focal plane of the lens: after passing through the focal plane, the beams propagate parallel to each other, forming a one-dimensional array of spatially separated beams. These beams are then focused by a tube lens and an objective into an array of optical tweezers, all propagating in parallel and focused into the focal plane of the objective. This is how it is possible to realize a 1D array of optical tweezers using an AOD.

As a practical example, let's consider to dive the AOD with two RF frequencies, ν_1 and ν_2, then two beams are deflected out at angles θ_1 and θ_2. The effect of a telescope with magnification $\mathrm{M} = \frac{f_{\text{tube}}}{f_{\text{scan}}}$ is a demagnification of the angular separation by a a factor $\frac{1}{\mathrm{M}}$. The distance between the two tweezers focused by the objective with focal length f_{obj} can be described as [69]:

$$d = 2f_{\text{obj}} \tan\left(\frac{\theta_1 - \theta_2}{2\mathrm{M}}\right) = 2f_{\text{obj}} \tan\left(\frac{(\nu_1 - \nu_2)\lambda}{2v}\frac{1}{2\mathrm{M}}\right) \tag{4.10}$$

It is possible to generate a two-dimensional square or rectangular array of tweezers using two orthogonal AODs (See Fig. 4.2 bottom) that causes deflection along two axis. A 1:1 relay telescope in 4f configuration is necessary in between the two AODs in order to match the deflection planes of the two devices and ensure that angular deflections are mapped exactly into spatial shifts at the object plane.

Driving the AODs with static radio frequencies allows the generation of one- or two-dimensional arrays of optical tweezers at fixed positions in the objective's focal plane. In this configuration, each frequency tone applied to the AOD corresponds to

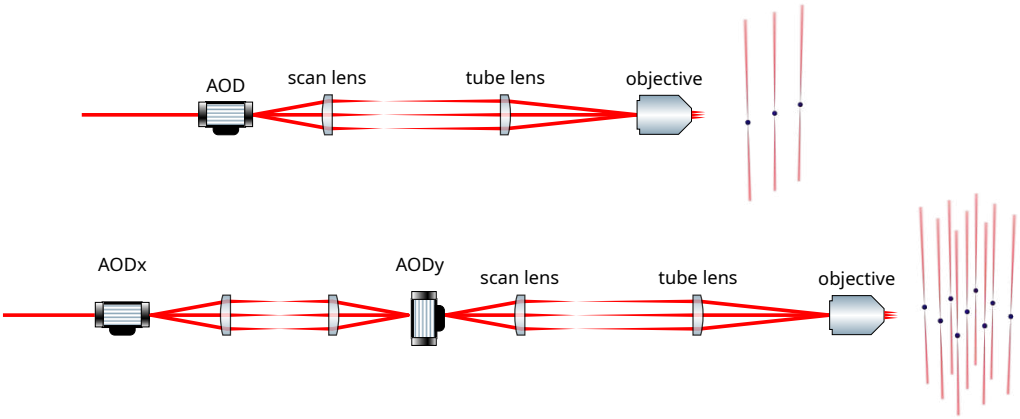

Figure 4.2. Optical layout for generating arrays of optical tweezers using AODs. (Top) A single AOD creates a one-dimensional array of laser beams by mapping different radio frequencies to different diffraction angles. A scan lens and a tube lens relay the angular separation to the back aperture of the objective, which focuses the beams into a 1D array of optical tweezers in the focal plane. (Bottom) Two orthogonal AODs (AODx and AODy) enable independent control along both axes, producing a two-dimensional array of optical tweezers at the focal plane of the objective.

a distinct diffraction angle, and thus to a single trap location. However, by modulating the driving frequencies in time, the position of each trap can be dynamically controlled, enabling the creation of moving optical tweezers.

4.2.2 Spatial Light Modulators (SLMs)

The other device that is commonly used to modulate a laser beam in order to produce an array of optical tweezer is the Spatial Light Modulator (SLM). In the context of quantum optics and atomic manipulation, SLMs are most commonly employed as phase-only devices, where they enable precise shaping of the incident wavefront to generate arbitrary intensity patterns in the focal plane of a high–NA objective.
Among the various architectures, Liquid Crystal on Silicon Spatial Light Modulators (LCOS-SLMs) are widely used because they combine high spatial resolution with phase-only modulation and relatively low optical losses. Applying a certain voltage to each pixel of the liquid crystal is possible to reorient the liquid crystal molecules, modifying the effective refractive index experienced by the incident light polarization in that pixel. As a result, the device introduces a controllable phase delay on the reflected wavefront, thereby realizing a programmable two-dimensional phase mask $\phi(x, y)$. When a lens is placed at a distance equal to its focal length from the SLM, the phase modulation imprinted on the wavefront in the SLM plane is converted into a spatial modulation in the focal plane of the lens (Fourier plane) [70]. In this way, the lens effectively performs the Fourier transform of the phase mask, projecting its spatial frequency content onto the conjugate plane.
The propagation of the field after modulation can be described within the paraxial

approximation by Fourier optics. If the incident field at the SLM plane is written as:

$$U(x, y) = A(x, y)e^{i\phi(x,y)} \tag{4.11}$$

where $A(x, y)$ is the amplitude profile of the incoming beam and $\phi(x, y)$ is the programmed phase mask, then in the focal plane of the lens or microscope objective the field distribution is proportional to the two-dimensional Fourier transform of the modulated wavefront:

$$\tilde{U}(k_x, k_y) = \mathcal{F}\left[U(x, y)\right] \tag{4.12}$$

with (k_x, k_y) the spatial frequency coordinates.
By controlling the pixel voltages of the SLM it is possible to realize arbitrary far-field intensity profiles [71], included different geometries of 2D optical tweezers array.
The central challenge lies in determining the appropriate phase mask $\phi(x, y)$ that generates a desired target intensity distribution $I_{\text{target}}(k_x, k_y)$ in the Fourier plane. Since only intensity can be directly measured, while phase information is not easily accessible, the design of phase masks requires iterative phase retrieval algorithms. The most widely used method in this context is the Gerchberg–Saxton (GS) algorithm, introduced by Gerchberg and Saxton in 1972 [72].
The Gerchberg–Saxton algorithm is an iterative method used to compute a phase mask that generates a desired intensity pattern in the target plane. Starting from a known input amplitude in the source plane, an initial random phase is assigned, and the field is propagated to the target plane via a Fourier transform. At each iteration, the algorithm evaluates the difference between the projected field and the target pattern, updating the phase to minimize this discrepancy until the generated pattern closely matches the desired one.
The initial field at the SLM plane is:

$$U_0(x, y) = A(x, y)e^{i\phi_0(x,y)} \tag{4.13}$$

The field is then propagated to the target plane using a Fourier transform:

$$\tilde{U}_0(k_x, k_y) = \mathcal{F}\left[U_0(x, y)\right] \tag{4.14}$$

At the target plane, the desired intensity pattern I_{target} is imposed:

$$\tilde{U}_0'(k_x, k_y) = \sqrt{I_{\text{target}}(k_x, k_y)}e^{i \arg \tilde{U}_0(k_x,k_y)} \tag{4.15}$$

The field is then propagated back to the SLM plane via the inverse Fourier transform:

$$U_1(x, y) = \mathcal{F}^{-1}\left[\tilde{U}_0'(k_x, k_y)\right] \tag{4.16}$$

To start the next iteration, the known input amplitude is reimposed while keeping the updated phase:

$$U_1'(x, y) = A(x, y)e^{i \arg U_1(k_x,k_y)} \tag{4.17}$$

This iterative loop goes on until the difference between the obtained and target amplitude is below a certain threshold. The GS algorithm is computationally efficient and sufficiently robust for practical implementations, making it a standard tool in holographic beam shaping.

We plan to implement an SLM in our experiment, as illustrated in Sec. 4.3. We are currently testing the performance of two SLM devices, both from Meadowlark Optics. The first is the E-19x12-500-1200-HDM8, featuring a resolution of 1920 × 1200 pixel with a pixel pitch 8 × 8 µm, resulting in an array size of 15.36 × 9.6 mm, and it is driven at 60 Hz by a HDMI controller with output trigger. The second one is a UHP SLM 1024×1024 with 1024 × 1024 pixel and a pixel pitch 17 × 17 µm, giving an array size of 17.40 × 17.40 mm, featuring analog data addressing and a refresh rate of 1.4 kHz.

4.3 Our tweezer generation scheme

The results presented in this thesis were obtained using two-dimensional arrays of optical tweezers generated by means of two crossed AODs, producing a static array. In the near future, however, the setup will be upgraded to combine an SLM for the generation of the static array with the two crossed AODs, which will enable dynamic rearrangement of atoms among the tweezers. A schematic of the final setup is shown in Fig. 4.3.

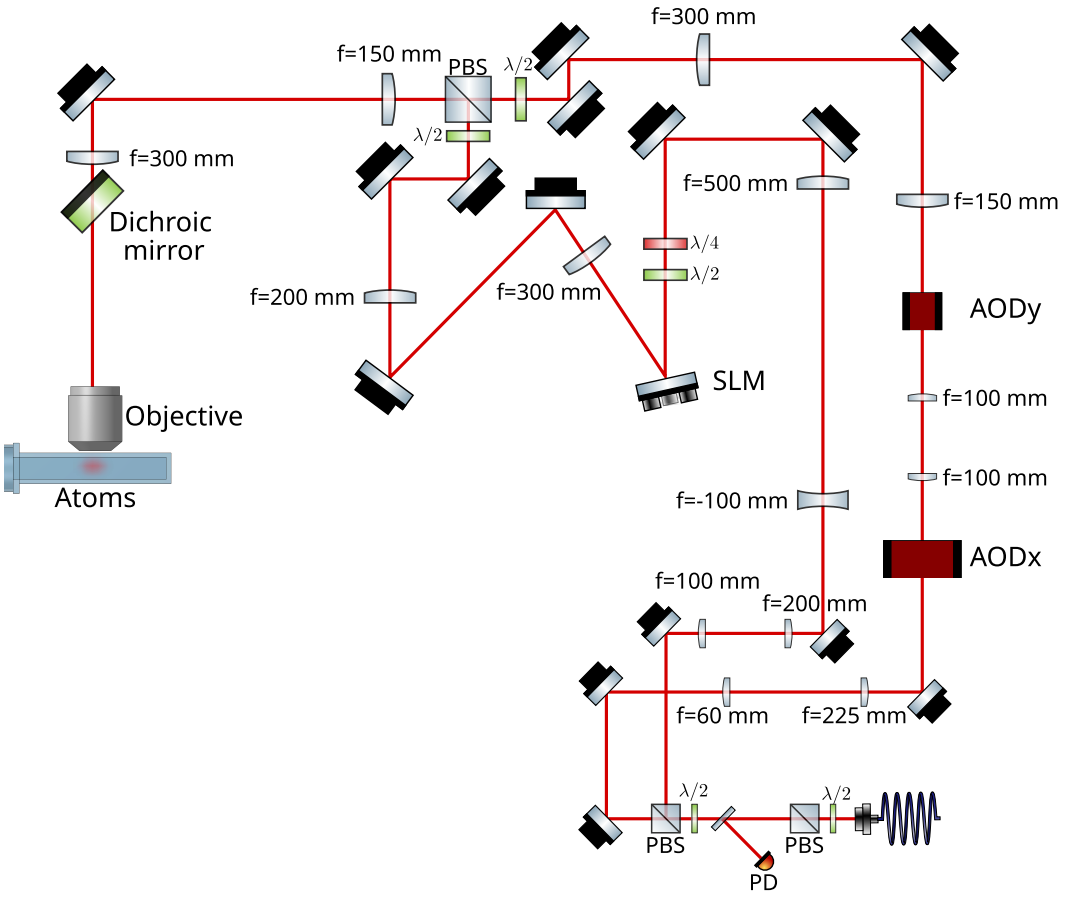

Figure 4.3. Sketch of the setup for the optical tweezer generation employing two crossed AODs and an SLM.

A laser beam at 813 nm (see Sec. 6.3.3) is split into two paths: one directed to the

SLM and the other to the two crossed AODs. The two beams are then recombined using two waveplates and a polarizing beam splitter (PBS) in a section of the beam path where the beam is collimated to minimize possible distortions. The two paths share a common telescope before the objective. To minimize aberrations, 2 inch achromatic lenses are employed throughout the setup. At present, only the AOD-based part of the system has been fully implemented and is operational. The SLM branch is currently under testing and characterization and will be integrated in the near future.

At the fiber output (60FC-SMA-T-4-M20-10 collimator), the laser beam has a waist of $w = 0.9\,\text{mm}$. A waveplate and a PBS are used to convert polarization fluctuations into power fluctuations, which are monitored by a photodiode (PD). The photodiode signal is then employed in a feedback loop to stabilize the power delivered by the fiber with a PID.

Along the AOD branch, a telescope expands the beam waist by a factor of 3.75 ($f = 60\,\text{mm}, f = 225\,\text{mm}$), to match the active aperture of the AODs ($7.5 \times 7.5\,\text{mm}$). The beam is sequentially deflected in the x and y directions by the two orthogonal AODs, with a $1:1$ relay telescope ($f_1 = f_2 = 100\,\text{mm}$) in between to match the planes of the two AODs.

To recombine this path with the SLM branch and accommodate two steering mirrors and a dichroic mirror before the objective, a second relay telescope is introduced prior to the scan and tube lenses. This telescope increases the beam waist by an additional factor of 2 ($f = 150\,\text{mm}$, $f = 300\,\text{mm}$), while the scan and tube lenses further enlarge it by a factor of 2 ($f_{\text{scan}} = 150\,\text{mm}$, $f_{\text{tube}} = 300\,\text{mm}$). With this configuration, the beam waist at the back focal plane of the objective is $w = 13.5\,\text{mm}$, which matches the aperture radius ($R = 13.5\,\text{mm}$). The maximum extent of the tweezer array, obtained by considering two frequencies at the edges of the RF bandwidth in Eq. 4.10, is approximately $\sim 150\,\mu\text{m}$.

In the SLM path the laser beam is expanded by a factor of 10 using two telescopes ($f = 100\,\text{mm}$, $f = 200\,\text{mm}$ and $f = -100\,\text{mm}$, $f = 500\,\text{mm}$) to match the dimensions of the UHP SLM 1024×1024 display. This configuration represents a compromise between maximizing the active display area available for generating the tweezer pattern and minimizing power losses by preventing beam clipping. The phase-modulated light is then relayed to the back focal plane of the objective using an additional telescope ($f = 300\,\text{mm}$, $f = 200\,\text{mm}$) and the last common telescope, magnifying the phase-modulated image to approximately 24 mm at the back focal plane of the objective. A Semrock dichroic mirror with a 3 mm substrate is placed before the objective to transmit the tweezer light while simultaneously separating the collected blue fluorescence, which is reflected along a different optical path (see Sec. 8.2.2); the substrate thickness minimizes the aberrations introduced by the mirror to below $\lambda/4$.

The magnifications in the setup are designed to match the beam size to the apertures of the devices used (AODs and SLM), achieving an optimal compromise between efficiency and losses. Additionally, the system is arranged so that the beam incident on the back focal plane of the objective matches the objective's aperture. If the beam waist is smaller than the aperture radius, the effective numerical aperture of the objective is reduced to the size of the beam, producing a larger tweezer in the focal plane. Conversely, if the beam waist is bigger than the aperture radius

of the objective part of the laser power is lost as the Gaussian profile is clipped by the aperture. Numerical simulations reported in Ref. [48] show that the optimal compromise, assuming constant input power, is achieved when $w/R \approx 1$.

4.3.1 Going 3D

In the future, we aim to further improve our tweezer setup in order to generate three-dimensional arrays of optical tweezers. Such an advancement would not only open new possibilities for the study of many-body physics, but also significantly enhance the scalability of the system. The concept of the setup we envision is illustrated in Fig. 4.4.

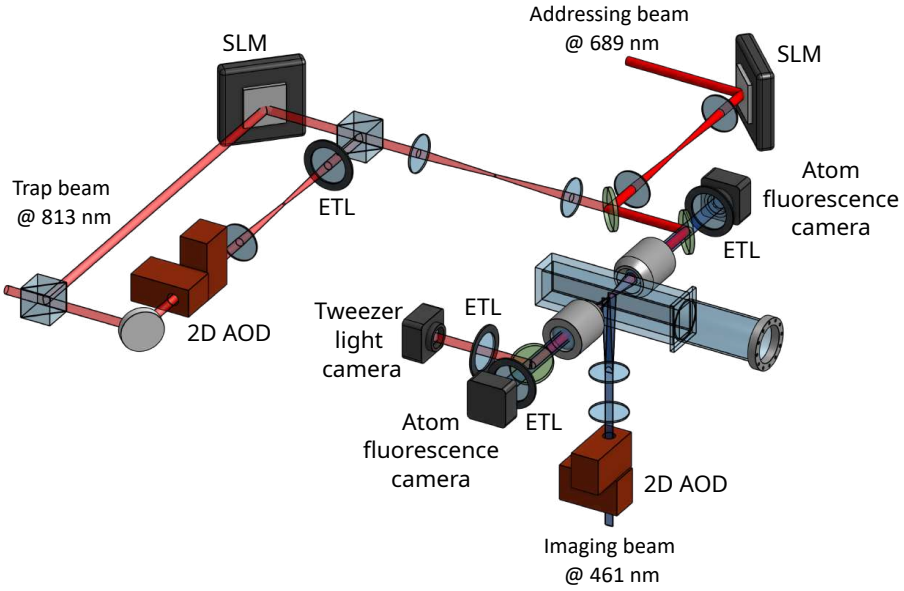

Figure 4.4. Proposed optical layout for the generation and imaging of three-dimensional arrays of optical tweezers. The trapping beam at 813 nm is shaped by a spatial light modulator (SLM) and focused into the vacuum cell through a high-NA objective, which is also used to collect atomic fluorescence. An electrically tunable lens (ETL) in the trapping path allows for axial positioning of the tweezers, while a second ETL in the detection path enables imaging of different planes of the array. A second high-NA objective, aligned from the opposite side, is dedicated to fluorescence collection and imaging of the tweezers, thereby increasing the detection efficiency. Local addressing is provided by a 689 nm beam shaped by an additional SLM. Imaging beams at 461 nm are coupled through acousto-optic deflectors (AODs) to illuminate the atoms for fluorescence detection.

The idea is to add Fresnel lens patterns on top of the phase pattern for generating the static tweezer array on the SLM and employ electrically tunable lenses (ETLs), whose focal length can be dynamically adjusted by varying the applied voltage, on the AODs path. This approach would allow us to shift the focal plane of the tweezer beam within the vacuum cell, thereby controlling the position of the optical tweezers along the beam propagation axis. Similarly, incorporating an ETL in the imaging

path would enable the detection of different planes of the three-dimensional array during fluorescence imaging.
In this configuration, the AODs can be used to dynamically reorder the optical tweezers within a given focal plane (see Sec. 4.6). In combination with the ETL, which shifts the imaging and trapping planes axially, this approach would enable three-dimensional rearrangement schemes based on fast beam deflection within a plane and sequential addressing of multiple planes.
In the scheme shown in Fig. 4.4, two high-numerical-aperture objectives are included: One objective is used both to generate the optical tweezers and to collect atomic fluorescence. The second objective, placed on the opposite side, is used for imaging the tweezers and collect the atomic fluorescence. This dual-objective configuration will be used to increase the collected solid angle, thus improving signal-to-noise ratio and reducing exposure times during single-atom detection. Additionally, a light-sheet illumination scheme is planned for fluorescence imaging, generated by scanning a 461 nm beam with a pair of AODs (or AOMs). This configuration would allow selective illumination of a single plane of the three-dimensional array, synchronized with the ETL position and camera acquisition, thereby minimizing background fluorescence from out-of-focus planes.
A second SLM is also included in the scheme driving a 689 nm beam to enable local addressing within the three-dimensional array (e.g., for site-selective control or state preparation).

4.4 Dynamical spatial light modulation in the ultraviolet spectral range

M. Ammenwerth, H. Timme, **V. Giardini**, R. Tao, F. Gyger, O. Lib, D. Berndt, D. Kourkoulos, T. Rom, I. Bloch, and J. Zeiher, *"Dynamical spatial light modulation in the ultraviolet spectral range,"* **Physical Review Applied 24**, 034031 (2025).

During my PhD, I carried out a four-month research stay at the Max Planck Institute of Quantum Optics (MPQ) in Munich, where I worked on the characterization of a novel class of devices for ultraviolet light modulation. Although the technology described in this section is not directly employed in the experimental work presented elsewhere in this thesis, it represents a promising development for the future of neutral-atom quantum platforms.

The device under investigation is a novel spatial light modulator based on a piston micro-mirror array (MMA) used to demonstrate arbitrary beam shaping in the ultraviolet regime at a wavelength of 322 nm [73]. Conventional SLMs can operate over a wavelength range covering visible and the near-infrared region, but are limited in the ultraviolet due to liquid crystal degradation under UV light exposure [74]. In piston type MMA each pixel is a mirror element that can be displaced in a piston-like motion, imprinting a controllable phase shift onto the reflected wavefront. Unlike liquid-crystal devices, this mechanism is polarization-independent and intrinsically broadband, the wavelengths that it can support depending on the mirror coatings used. As a result, MMAs are well suited for ultraviolet operation.

The possibility to dynamically modulate light fields at UV wavelengths is highly relevant for experiments with alkaline-earth atoms, such as Strontium, and for new applications in trapping atoms at ultra-small distances [75], or for homogenizing UV beams for zone-based quantum computing and quantum simulation architectures [76].

The prototype tested at MPQ consisted of a micromirror array system (64k customer evaluation kit piston MMA α-module by Fraunhofer) with 256×256 square mirrors with a pitch of 16 µm. The individual mirrors can be axially displaced by up to 350 nm, such that a full phase modulation contrast of $\phi(x, y) \in [0, 2\pi)$ is possible for wavelengths up to 700 nm.

To characterize the device, a series of measurements were carried out using two different wavelengths: 688 nm and 322 nm. While operating with the UV laser light the MMA surface was continuously flushed with a weak flow of nitrogen to prevent any damage of the chip from ozone, which forms from ambient oxygen under intense UV irradiation.

The beam was expanded and shaped to illuminate the active area of the array, and the reflected light at an angle of approximately 7° was collected with a UV-sensitive CCD camera (see Fig. 4.5).

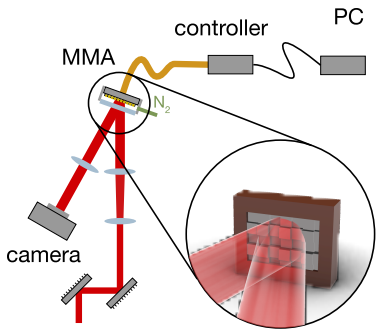

Figure 4.5. The optical setup to generate configurable beam shapes with a phase-only spatial light modulator based on a micro-mirror array (MMA). The generated patterns are characterized on a camera.

In order to achieve diffraction-limited optical potentials phase-shifting interferometry was employed to measure a spatially resolved, stationary phase correction map to compensate for aberrations introduced by the optical system. This map reflects the optical aberrations present in the entire beam path and can be directly used to correct the wavefront [77, 78].

A blazed grating is displayed on the screen of the MMA and overlapped with a total black mask except for two circular regions, each with a radius of 10 pixels. This two regions are the reference superpixel and the probe superpixel. The two superpixels diffract the incoming beam into different paths through the optical system, leading to an interference fringe on the detection camera (see Fig. 4.6a). The relative phase accumulated by the probe beam, with respect to the fixed reference, appears as a shift of the interference fringe. By keeping the reference superpixel fixed at the center of the MMA and scanning the position of the probe superpixel, we reconstructed the spatially varying phase profile of the aberrations across the entire aperture.

The initial wavefront error, shown in Fig. 4.6b was found to be dominated by

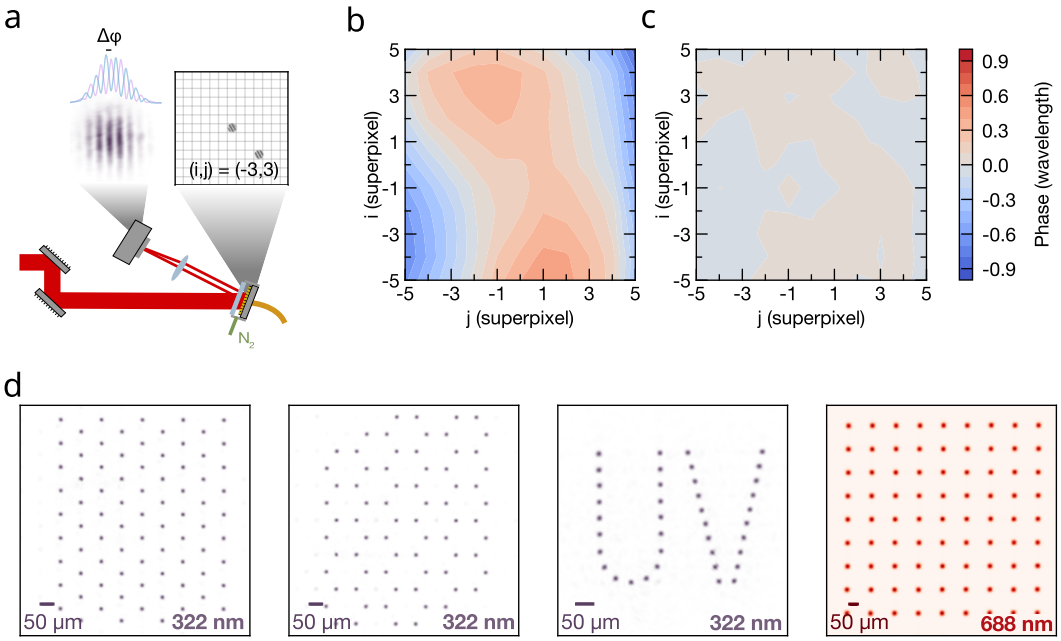

Figure 4.6. a) Measurement scheme: the phase of probe superpixels on the MMA is varied with respect to a fixed reference, producing interference fringes on the camera. b) Unwrapped and interpolated phase map across the MMA. c) Corrected wavefront after applying the retrieved phase mask, showing a flat phase profile. d) Various tweezer arrays: triangular, honeycomb, and in a UV-letter shape at 322 nm and rectangular at 688 nm with normalized peak-to-peak homogeneity of the intensity of 0.3%

astigmatism. Applying the measured phase correction to the MMA and repeating the interferometric measurement, after a single round of correction, we achieved a root-mean-square (RMS) wavefront flatness of $\lambda/100$ at 322 nm. The residual curvature of the corrected wavefront is shown in Fig. 4.6c.

With this corrected system, arbitrary beam shapes could be generated by computing a hologram corresponding to the desired intensity distribution (see Fig. 4.6d). To further equalize the intensity of the individual traps the amplitudes of the individual tweezers were adjusted according to the measured image until a target uniformity was reached. This procedure allowed us to achieve an intensity inhomogeneity (standard deviation over mean) of 0.3% in both the visible and UV spectral ranges.

Each mirror of the device is mounted on a spring-like suspension and is actuated electrostatically to realize a piston displacement; in principle, this architecture could introduce excess mechanical or electronic noise that would compromise its suitability for precision experiments. Applications of arbitrary light patterns for trapping and manipulating individual atoms are particularly sensitive to fluctuations in the optical potentials, since even small amounts of phase or amplitude noise can translate into heating, decoherence, or uncontrolled atomic motion [79]. For this reason, it is essential to assess the stability of the phase patterns generated by the MMA. To quantify this aspect, a phase noise characterization using a Mach–Zehnder interferometer was carried out (the scheme is illustrated in Fig. 4.7a. A collimated input beam at 688 nm was split into two paths, one of which was directed onto the MMA which displays a flat phase profile with a π stroke. The other beam (reference)

was frequency-shifted by 80 MHz using an AOM to avoid contamination of the signal by low-frequency environmental noise. The two beams are then recombined with a beam splitter and sent to a photodetector. The phase noise of the MMA modulates the phase of the beat signal which was analyzed with an electrical phase noise analyzer (Keysight N9020B spectrum analyzer).

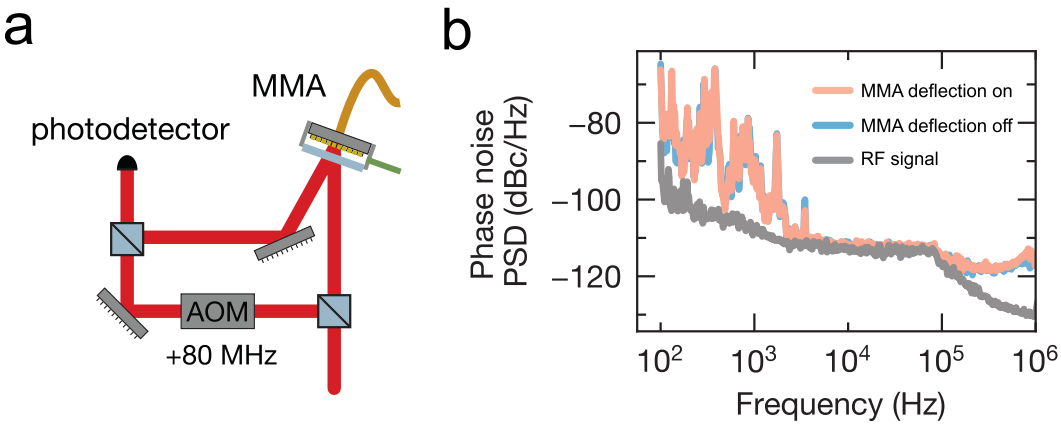

Figure 4.7. a) Schematic of the interferometric setup used to measure the phase noise induced by the micro-mirror array. A Mach–Zehnder interferometer is employed, where the reference arm is frequency shifted by 80 MHz using an AOM. The recombined beams generate a beat signal on a fast photodetector, from which the phase noise of the MMA is extracted. b) Measured phase noise spectra for the MMA in the deflected state (blue) and in the off-state (orange). No significant difference is observed between the two conditions, indicating that the MMA does not introduce additional noise within the sensitivity of the measurement. For comparison, the phase noise of the RF source used to drive the AOM is also shown (gray).

For each measurement a deflection window of 500 ms was chosen and the sweep of the analyzer was synchronized with the activation of the MMA. The procedure was performed with the MMA in the on and off state to directly compare the phase noise spectra. The results, displayed in Fig. 4.7 b, show no noticeable difference between the active (blue) and inactive (orange) states of the device. This observation establishes an upper bound to the phase noise imprinted by the MMA, which is negligible compared to mechanical instabilities of the bulk interferometer up to a few kilohertz. At higher Fourier frequencies in the range between 10 kHz and 100 kHz, the sensitivity of the measurement was limited by the intrinsic noise of the RF signal driving the AOM (gray), and we have no indication of significant contributions from the MMA in this regime. So the phase noise of the micro-mirror array is compatible with the requirements of state-of-the-art optical trapping setups. In particular, the absence of characteristic switching noise suggests that the MMA architecture may offer distinct advantages for extremely noise-sensitive applications such as holographic tweezer arrays for neutral atoms.

In the final set of measurements carried out during this project, the investigation was directed toward the generation of flat-top beams using the MMA. This capability is of particular importance for neutral-atom quantum information processing, where homogeneous illumination is required to maximize the number of qubits that can be manipulated in parallel while reducing sensitivity to beam pointing and intensity

fluctuations. The need for such beams is especially pronounced in the ultraviolet regime, where Rydberg excitations in alkali [80, 81] and alkaline-earth-like atoms such as Strontium and Ytterbium [82, 83, 84] underpin the implementation of high-fidelity entangling gates.
Using the MMA flat-top beams were generated both at 322 nm and at 688 nm.

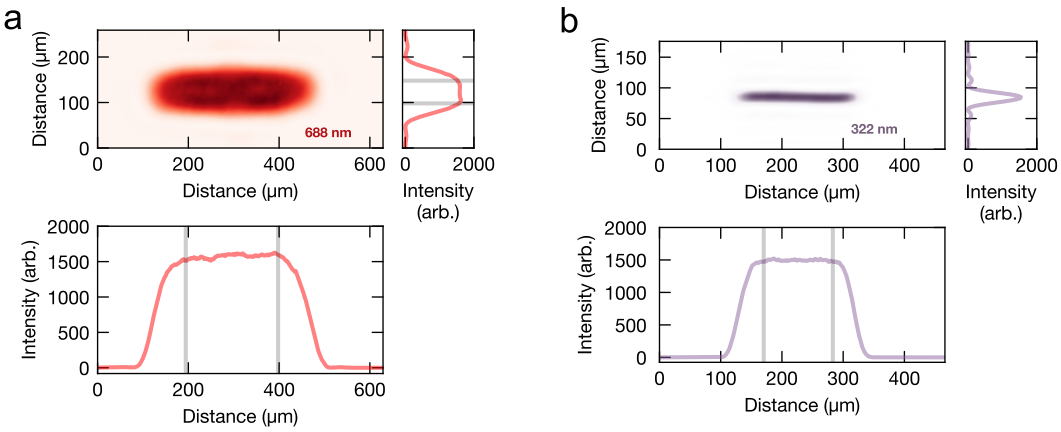

Figure 4.8. a) Measured flat-top beam profile at a wavelength of 688 nm, optimized through iterative phase correction of the micro-mirror array. (b) Measured flat-top beam profile at a wavelength of 322 nm, demonstrating homogeneous illumination suitable for ultraviolet gate operations.

At 322 nm, we obtained a one-dimensional flat-top profile with a residual RMS inhomogeneity of 0.75% and a peak-to-peak variation of 3.65% across a region of 113 µm, with a power efficiency of 28%. These values are compatible with reaching state-of-the-art logical gate fidelities across large-scale atomic registers [85]. At 688 nm, a two-dimensional flat-top beam with a flat intensity plateau in both spatial directions was produced, characterized by RMS inhomogeneities of 1.8% (1.4%) and peak-to-peak variations of 7.4% (6.2%) along the x- (y-) axes, respectively, with an overall efficiency of 38%. The resulting profiles, illustrated in Fig. 4.8 a and Fig. 4.8 b, represent the culmination of this investigation and establish piston-type MMAs as a promising technology for high-quality beam shaping in both the visible and ultraviolet spectral ranges, with direct relevance for future scalable quantum simulation and computation.

4.5 Light-assisted collisions and single-atom loading

A key feature of optical tweezer platforms is the ability to isolate a single atom in each trap. To load atoms into the optical dipole traps, we spatially overlap the traps with the cold atomic cloud generated by the narrow-line red MOT described in Sec. 7.4. The traps typically have depths on the order of tens to hundreds of µK, while the atoms in the MOT have a thermal energy of only about 5 µK. The number of atoms that are loaded from the MOT into a tweezer follows a Poisson distribution [86]. However, the mean atom number is essentially impossible to be measured directly with fluorescence imaging. This is due to two main limitations: first, the detection camera allows for a precise discrimination of zero and one/many

atoms but does not allow to clear out multiple occupations; second, the fluorescence imaging process itself may induce losses that affect the atom number during the measurement. For a Poisson distribution of a mean atom number $\tilde{N}$, the probability of loading zero atoms is $P(0) = e^{-\tilde{N}}$, the fraction of images determined to contain an unoccupied tweezer give an upper bound $P(0)$, from which we can get a lower bound on the mean occupation number $\tilde{N} = -\ln(P(0))$. In order to have one atom per tweezer one strategy might be to fine-tune the red MOT and traps parameters to maximize the probability of loading only one atom. However, the maximum possible probability of loading a single atom under Poissonian statistics is only about 37%, for the rest of the tweezers, 37%; would be empty and 26% would be loaded with multiple atoms [48]. To prepare exactly one atom in each trap a mechanism widely used in single-atom physics is pairwise loss [87, 88, 89] via light-assisted collisions (LACs).When two atoms occupy the same trap and are illuminated, the light can couple the pair into an excited molecular potential. The atoms then accelerate along this potential and gain kinetic energy. If the acquired energy exceeds the trap depth U_0, both atoms are lost from the trap in a single collision event. This process is schematically illustrated in Fig. 4.9.

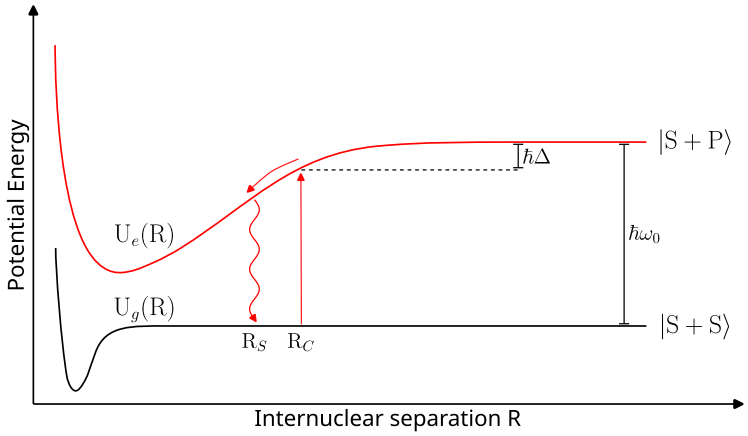

Figure 4.9. The molecular interaction potentials are shown as a function of the internuclear separation. The molecular potential of two atoms in the S angular momentum state scale as R^{-6}, when the red light excite one of the two atoms to the P state, the molecular potential scale as a dipole-dipole potential R^{-3}. This leads to an acceleration of the atoms towards each other and subsequent loss from the trap once the acquired energy exceeds the trap depth.

With this mechanism of pairwise losses, two atoms are lost from each tweezer at every collision. Therefore, after a certain number of collisions, the tweezers will be left with either 0 or 1 atom depending on whether the initial number of atoms contained in each individual optical trap was even or odd. The loss process thus naturally terminates with a binary occupation, where each trap is either empty or hosts a single atom, since no further pairwise collisions can occur.
Assuming that the initial atom number distribution in each tweezer is Poissonian with mean $\tilde{N}$, the probability of ending with a single atom corresponds to the probability of having started with an odd number of atoms: The single-atom loading

probability can be estimated as

$$p_{\text{single}} \approx \frac{1}{2}\left(1 - e^{-2\tilde{N}}\right)$$

For large $\tilde{N}$, the even and odd occupations become nearly equal, and already for $\tilde{N} \gtrsim 5$ the difference is negligible. As a result, on average about 50% of the tweezers are expected to end up empty, while the remaining 50% contain a single atom.

4.6 Defect-free arrays

The LAC process ensures binary occupation, resulting in traps being randomly loaded with a 50% filling fraction. Even when more elaborate schemes are employed to push the single-site filling fraction above 80% [90, 91, 92], defects remain unavoidable. To obtain defect-free arrays deterministically, atoms must be rearranged using an additional movable optical tweezer superimposed onto the static array, which picks up atoms from initially occupied sites and transports them to vacant target sites [29]. While an SLM can generate static tweezer arrays, usually it is too slow to perform dynamical rearrangement, having a refresh rate on the order of tens of milliseconds. Instead, a pair of orthogonal AODs can be driven with time-dependent RF signals to create a dynamically movable tweezer deeper than the static traps that can be used for rearrangement. Using a Spectrum M4i.6631-x8 AWG we can generate both the static frequencies and the frequency sweeps required for reordering. The AWG can control independently its two channels with 400 MHz bandwidth, $1.25\,\text{GS}\,\text{s}^{-1}$ sampling rate, 16-bit resolution, and 2 GS on-board memory for storage of pre-calculated waveforms. The signals are filtered (low-pass at 150 MHz, high-pass at 5 MHz), amplified with Mini Circuits ZHL-5W+ RF amplifiers, and then sent to the AODs. The attenuators placed before the amplifiers ensure safe operation by matching the required2 W input power.
The optimal reordering sequence will be computed based on the fluorescence image of the initial atom distribution, and a number of algorithms have been proposed in the literature to minimize the number of moves and so the required time for the process [93, 29, 94]. We are still working on our rearrangement process. A sketch of the reordering sequence is shown in Fig. 4.10.
A typical single move takes about 1 ms to transport an atom with high fidelity. For large arrays, exceeding few hundred atoms, this results in a total reordering time that becomes comparable to the vacuum lifetime. To address this limitation, some groups have adopted cryogenic environments to extend atom lifetimes [37], while others have pursued faster, parallelized rearrangement schemes using high-speed SLMs. Notably, a modified Gerchberg–Saxton algorithm implemented on a Meadowlark XY-series SLM operating at 2 kHz enabled parallel reordering with near-unity filling for arrays up to 30 atoms [95].

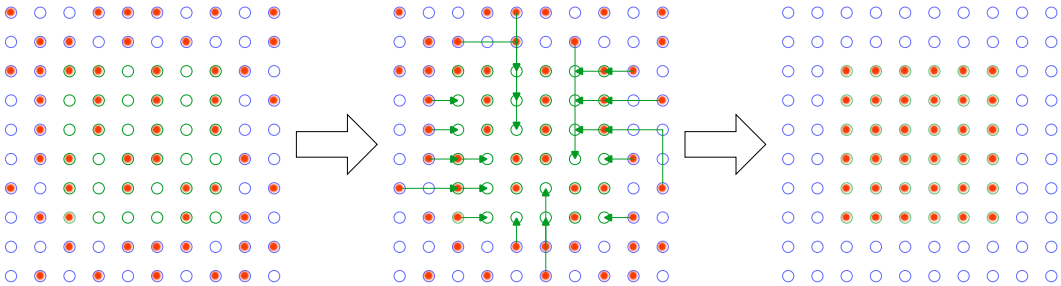

Figure 4.10. Schematic of the atom rearrangement process. Left: probabilistically loaded tweezer array after collisional blockade, showing random single-atom occupancy. Center: movable tweezers generated by AODs transport atoms from occupied to empty sites, as indicated by the arrows. Right: resulting defect-free, fully filled target array.

Chapter 5

Rydberg atoms

Arrays of individually trapped neutral atoms in optical tweezers provide a scalable and highly controllable platform for quantum simulation. In their ground state, however, the atoms are separated by several micrometers and do not naturally interact on relevant timescales, which strongly limits the range of many-body phenomena that can be explored. To overcome this limitation, strong and controllable long-range interactions can be introduced via excitation to Rydberg states.
Rydberg states are highly excited electronic states with large principal quantum number n, where one electron occupies a very extended orbital. Their large spatial extent make them an ideal resource for engineering long-range atomic interactions and probing correlated quantum phenomena.

5.1 Rydberg physics: scaling laws and blockade

Rydberg atoms are defined as atoms in which a valence electron is promoted to a state with very high principal quantum number n. In this regime, the atom resembles a hydrogenic system, with a single electron moving far from the nuclear core. The influence of the inner electrons on the Rydberg electron is not negligible and is described through the quantum defect $\delta_{n,\ell,j}$, which depends on n, the orbital angular momentum ℓ, and the total angular momentum j. The binding energy of a Rydberg state can therefore be written as [96]:

$$E_{\text{bind}} = \frac{Ry}{(n - \delta_{n,l,j})^2} \tag{5.1}$$

where Ry is the Rydberg constant corrected for the reduced mass of the electron–nucleus system:

$$Ry = \left(\frac{m_e}{M + m_e}\right)\left(\frac{m_e e^4}{8\varepsilon_0^2 h^2}\right) \tag{5.2}$$

with M the atomic mass, m_e the electron mass, e the elementary charge, h Planck's constant, and ε_0 the vacuum permittivity. From Eq. 5.1 one can see that the binding energy scales as n^{-2}, which in turn implies that the level spacing between adjacent Rydberg states decreases as n^{-3}. These scaling behaviors, as well as several

other characteristic properties, have been extensively studied both theoretically and experimentally [96, 97, 98] and are reported in Tab. 5.1.

Property	n-scaling
Binding energy	n^{-2}
Energy between adjacent n states	n^{-3}
Radiative lifetime τ	n^3
Orbital radius $\langle r \rangle$	n^2
Dipole moment $\langle np \vert er \vert nd \rangle$	n^2
Scalar polarizability α	n^7
Dipole-dipole coefficient C_3	n^4
van der Waals coefficient C_6	n^{11}

Table 5.1. Scaling of key Rydberg atom properties with principal quantum number n.

The spontaneous emission rate towards a lower state is given by:

$$\Gamma \propto \frac{|\mu|^2 \omega^3}{3\pi\varepsilon_0 \hbar c} \tag{5.3}$$

where μ is the transition dipole moment and ω is the transition frequency. Spontaneous decay into neighboring Rydberg states is strongly suppressed due to the small transition frequency ω, while decay into the ground state is inhibited by the very small dipole matrix element μ, which originates from the negligible overlap between the corresponding wavefunctions.

The most interesting feature of Rydberg atoms in the context of quantum simulation is the strength of their mutual interactions. For two atoms separated by a distance bigger than the typical size of the electronic wavefunction $R \gg \langle r \rangle$, the dominant term is the electric dipole–dipole interaction Hamiltonian [30]:

$$\hat{V}_{dd} \sim \frac{\hat{d}_1 \cdot \hat{d}_2}{4\pi\varepsilon_0 R^3} \tag{5.4}$$

where the dipole operator is defined as $\hat{d} = -e\hat{r}$ and its matrix element between states with the same n is $d \sim n^2 e a_0$.
Two important regimes of Rydberg–Rydberg interactions can be distinguished. When both atoms are excited to the same spherically symmetric state, such as $|nS\rangle$, the average dipole moment vanishes and the first-order contribution of the dipole–dipole interaction is zero. In this case, the interaction appears only at second order in perturbation theory, through the virtual coupling of the pair state $|nS, nS\rangle$ to opposite-parity states like $|nP, nP\rangle$, which are detuned by an energy Δ. The resulting potential takes the form of a Van der Waals interaction:

$$V(R) \propto \frac{C_6}{R^6}, \quad C_6 \propto \frac{d^4}{\Delta} \propto n^{11} \tag{5.5}$$

and can reach values on the order of megahertz for atoms separated by only a few micrometers between high-n Rydberg states [99, 100].
If the two atoms are prepared in states of different parity, for instance one in $|nS\rangle$

and the other in $|nP\rangle$, the dipole–dipole term contributes already at first order in perturbation theory. In this case, the interaction is a dipolar interaction:

$$V(R) \propto \frac{C_3}{R^3}, \quad C_3 \propto d^2 \propto n^4 \tag{5.6}$$

The coexistence of these two mechanisms, van der Waals and resonant dipole–dipole, provides an exceptional degree of flexibility in neutral-atom experiments. By tuning the quantum numbers of the excited Rydberg state or adjusting the separation of the optical tweezers, one can control both the strength and the functional form of the interaction, which is a crucial feature for implementing programmable quantum simulators.

The strong distance-dependent interactions between Rydberg atoms, not only determine the energy shifts of pair states but also give rise to a collective phenomenon of fundamental importance: the Rydberg blockade. We consider the resonant laser excitation of atoms initially in the ground state $|g\rangle$ to a Rydberg state $|r\rangle$. When two atoms are sufficiently close, the van der Waals interaction between them shifts the doubly excited state $|rr\rangle$ out of resonance with the excitation laser. As a consequence, the simultaneous excitation of both atoms is prevented, and only one of them can be promoted to the Rydberg level (see Fig. 5.1b).

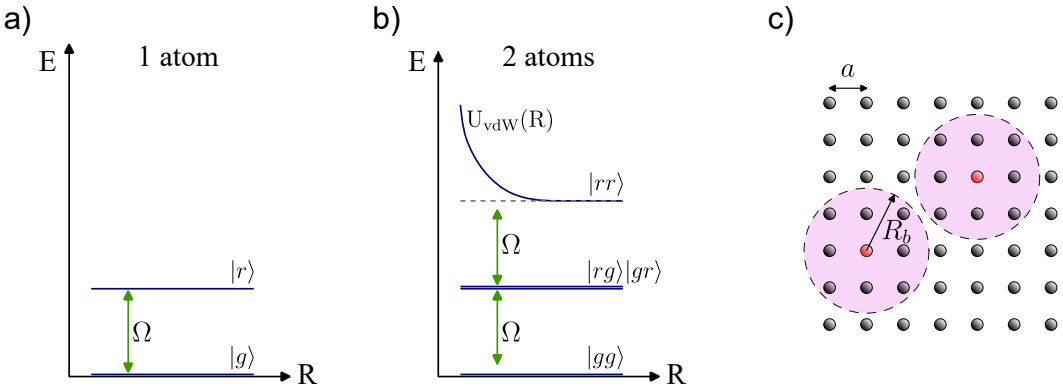

Figure 5.1. Schematic illustration of the Rydberg blockade mechanism. a) A single atom undergoes resonant laser excitation that couples the ground state $|g\rangle$ to the Rydberg state $|r\rangle$ with Rabi frequency Ω_R. (b) For two atoms separated by a distance $R < R_b$, the collective ground state $|gg\rangle$ is coupled only to the symmetric singly excited state $|\psi^+\rangle = (|gr\rangle + |rg\rangle)/\sqrt{2}$, while the doubly excited state $|rr\rangle$ is shifted out of resonance due to the strong van der Waals interaction. (c) In an extended ensemble of atoms, such as a regular array with lattice spacing a, the excitation of one atom to the Rydberg state (red dot) blocks the excitation of all atoms contained within a blockade sphere of radius R_b, thereby enforcing strong spatial correlations and collective dynamics.

This effect defines a characteristic distance known as the blockade radius R_b, inside which the excitation of a single Rydberg atom blocks the excitation of its neighbors (see Fig. 5.1c). Although the van der Waals interaction decreases continuously as $1/R^6$, it is convenient to define R_b as the distance at which the interaction energy equals the Rabi coupling of the laser:

$$\frac{C_6}{R_b^6} = \hbar\Omega_R \tag{5.7}$$

which leads to

$$R_b = \left(\frac{C_6}{\hbar\Omega_R}\right)^{\frac{1}{6}} \tag{5.8}$$

Since the coefficient C_6 grows rapidly with the principal quantum number n, the blockade radius can be tuned by selecting different Rydberg states.
The blockade mechanism plays a central role in many proposals and realizations of quantum simulation and quantum information protocols. Consider, for instance, two atoms initially prepared in the ground state $|gg\rangle$. Under global laser excitation, the doubly excited state $|rr\rangle$ is energetically inaccessible because of the blockade, and the system is restricted to evolve in the symmetric subspace spanned by $|gr\rangle$ and $|rg\rangle$. This results in the creation of a maximally entangled state,

$$\left|\psi^+\right\rangle = \frac{1}{\sqrt{2}}(|gr\rangle + |rg\rangle) \tag{5.9}$$

with an enhanced collective Rabi frequency $\sqrt{2}\Omega_R$ [101].
The same feature can be extended to ensembles of N atoms confined within a blockade sphere. In this case, at most one excitation is allowed, and the system evolves into a symmetric superposition of all possible single excitations:

$$|\psi_N\rangle = \frac{1}{\sqrt{N}}\sum_{i=1}^{N}|g...r_i...g\rangle \tag{5.10}$$

driven at a collectively enhanced Rabi frequency $\sqrt{N}\Omega_R$. In arrays of optical tweezers, where both the trap separation and the choice of Rydberg level can be controlled with high precision, the blockade mechanism thus allows the engineering of tunable long-range correlations extending across several sites.

5.2 Optical excitation pathways

Direct excitation of Strontium atoms to Rydberg states with a single photon from the ${}^1S_0$ ground state is experimentally impractical, since it would require deep-ultraviolet laser sources. A more convenient strategy is to use multi-step excitation schemes. Two relevant approaches are illustrated in Fig. 5.2.

In the first scheme (Fig. 5.2a), atoms are transferred to the long-lived metastable clock state $5s5p\,{}^3\mathrm{P}_0$, which can be treated as an effective ground state. From there, a single ultraviolet photon at $\sim 318.5\,\mathrm{nm}$ couples directly to a Rydberg state. This method has the advantage of effectively realizing a single-photon excitation without the drawbacks of intermediate state decay, while enabling relatively large Rabi frequencies ($\Omega \approx 10\,\mathrm{MHz}$ [48]).

An alternative approach (Fig. 5.2b) exploits a two-photon process via the $5s5p\,{}^3\mathrm{P}_1$ level, where the first laser at 689 nm couples off-resonantly to the intermediate state, and a second photon around 316.6 nm nm completes the excitation to a Rydberg state. Despite the apparent complexity, this method can drive the transition with coherence comparable to a single-photon process, at MHz frequencies [102], provided that the detuning from the intermediate state is sufficiently large.

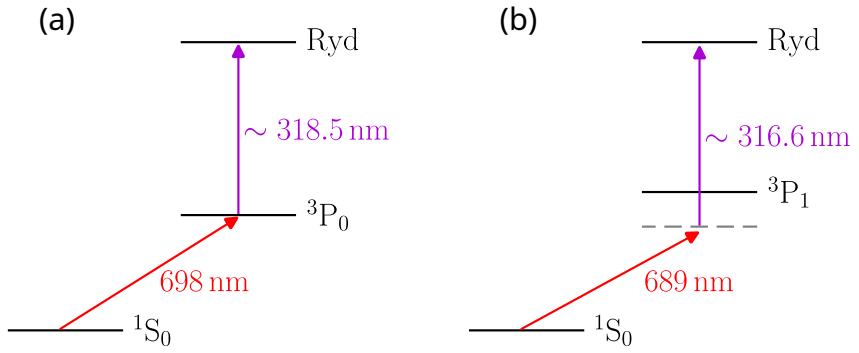

Figure 5.2. Two excitation schemes to access Rydberg states in Strontium. (a) A first step excites atoms to the $^3P_0$ state via the clock transition at 698 nm, followed by a second photon at 318.5 nm. (b) A two-photon transition via the $^3P_1$ intermediate state, using 689 nm and 316.6 nm light.

These two excitation schemes are the most widely used in neutral Strontium experiments, although alternative pathways involving both triplet and singlet states have also been demonstrated [103, 104, 105]. Our UV laser described in Sec. 6.3.4 can be tuned between 316 nm and 319 nm, allowing us to span the energy difference between the $^3P_0$ and $^3P_1$ states, making both these excitation accessible.

Chapter 6

Experimental apparatus

This chapter outlines the architecture and key components of the experimental system employed throughout this work. Our apparatus is designed to enable trapping, cooling, manipulation and imaging of ultracold Strontium atoms. At the core of the setup lies the vacuum system, which ensures the necessary ultra-high-vacuum (UHV) environment essential for minimal background collisions. To produce and manipulate cold atomic ensembles, we employ a magnetic field system based on a pair of high-field coils in anti-Helmholtz configuration, which generates the magnetic field gradient required for magneto-optical trapping. This primary coil pair is complemented by a set of three pairs of compensation coils aligned along all three spatial axes, whose role is to suppress ambient stray magnetic fields and thereby ensure a stable and well-defined magnetic environment in the experimental region. The apparatus is integrated with a comprehensive optical system, comprising the laser setups required for each stage of atom preparation and control, including slowing, cooling, trapping, coherent manipulation, and imaging.

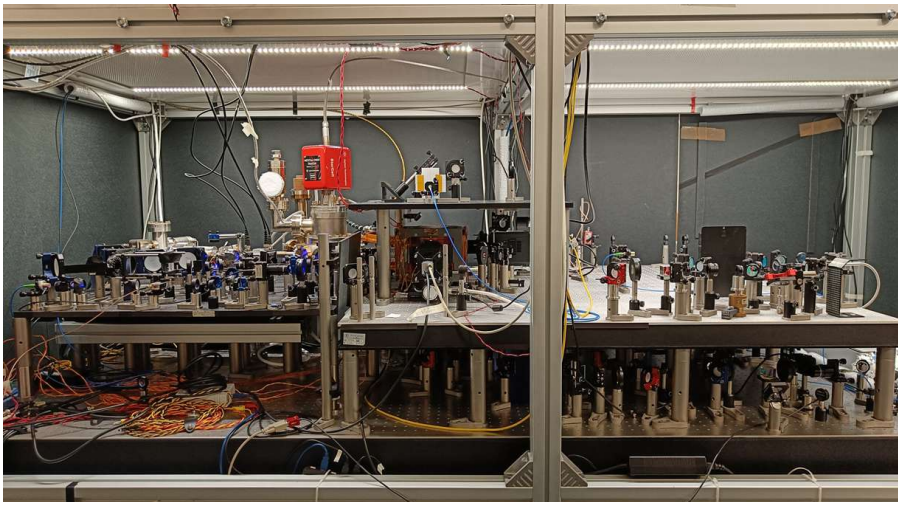

Figure 6.1. Side view of the experimental optical table. On the left side we have the vacuum system, mounted on a separate breadboard on a translation stage. The optical setups for trapping, manipulating and detecting the atoms are assembled on this optical table on three levels.

For practical and organizational reasons, the experiment is distributed over two separate optical tables: one dedicated to the laser systems (laser table), and the other hosting the experiment (experimental table Fig. 6.1). On the experimental table, two main breadboards are mounted: one supports the vacuum apparatus, and the other hosts optics for laser cooling and manipulation. The vacuum system itself is placed on a separate breadboard equipped with a translation stage, which allows the entire assembly to be moved forward and backward with high precision. This arrangements provides mechanical decoupling from the rest of the apparatus and facilitates alignment and maintenance.

6.1 Vacuum system and atomic source

The vacuum system, shown in Fig. 6.2, is composed of three main sections: an atomic source, a pumping chamber and a rectangular glass cell. The whole assembly is just 105 cm long from the oven at the back of the atomic source to the end of the glass cell.

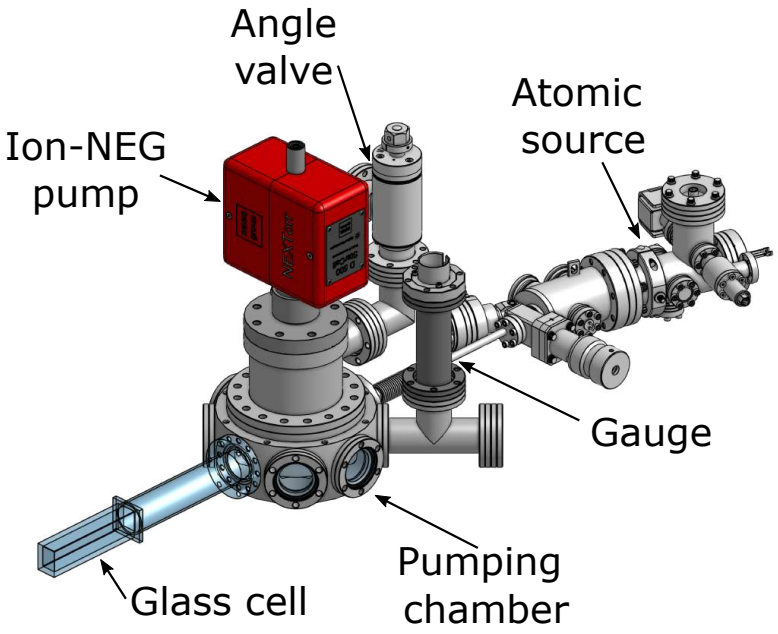

Figure 6.2. 3D render of the vacuum apparatus.

The atomic source used is a commercial Sr Beam RevC unit from AOSense, designed as a compact plug-and-play vacuum subsystem shown in Fig. 6.3. It includes a Strontium oven, some permanent magnets for the Zeeman slower and the 2D MOT, viewports for optical access and spectroscopy, an angled differential pumping tube, a mini ion pump, and an angle valve to isolate the source from the rest of the vacuum system. The oven is powered through two electrical feedthroughs and heats a resistive element to reach 420 °C, vaporizing the Strontium atoms. The emitted atomic beam passes through an array of microtubes that pre-collimate it by selecting

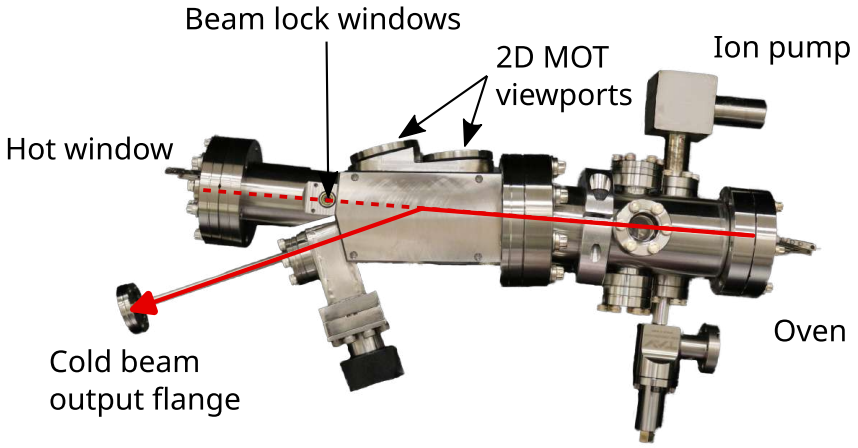

Figure 6.3. Sr Beam RevC unit from AOSense.The dashed line indicates the trajectory of undeflected atoms, while the solid line represents the trajectory of deflected atoms.

a narrow range of transverse velocities. Immediately downstream, three viewports allow for spectroscopic measurements of the atomic beam (for further details on the spectroscopic measurements see Ref. [106]). From the viewports, the magnet assembly appears to be a 5 cm long block positioned between the oven and the 2D MOT region. The Zeeman slower beam at 461 nm enters through the "Hot" window, which is a sapphire viewport heated to 300 °C to prevent a layer of atoms from coating the window and progressively reducing its transparency. The beam counter-propagates with respect to the atomic flux and slows down atoms via the magnetic field gradient created by the permanent magnets. In addition to the Zeeman slower deceleration, atoms are transversely deflected and cooled by two sets of 2D MOT beams, which enter through two large side viewports and are retro-reflected using in-vacuum optics. These beams further collimate and redirect the atomic beam to match the angle of the differential pumping tube before the cold beam output flange. Successful coupling into this tube requires precise optimization of beam geometry, polarization, detuning, and power. AOSense provides recommended parameters for beam alignment and optimization that proved to be an effective starting point. During the first year of operation, we implemented minor adjustments to maximize the atom number in the 3D MOT and minimize its temperature. The optimized values can be found in Tab. 6.1.

Beam	Waist	Power	Detuning	Polarization
Zeeman slower	8 mm (round)	50 mW	−580 MHz	σ^-
2D MOT (1)	25 mm × 5 mm	16 mW	−40 MHz	σ^+
2D MOT (2)	25 mm × 5 mm	8 mW	−40 MHz	σ^+

Table 6.1. Optimized beam size, power, detuning and and polarization for atomic source beams.

Spectroscopy on the atomic beam, used to frequency-lock the 461 nm laser to the atomic transition, is performed using a retro-reflected 461 nm beam, aligned orthogonally to the atomic flux via dedicated vertical viewports ("Beam Lock

Windows"). The retroreflection eliminates transverse Doppler shifts due to residual velocity components and doubles the absorption signal. The 461 nm laser is locked to the $^1S_0 \leftrightarrow {}^1P_1$ transition in ^{88}Sr using a double-pass AOM for fine frequency control. The diode laser current is modulated at 150 kHz, and the resulting signal is demodulated by the internal electronics to produce an error signal for laser locking (see Sec. 6.3.1). Due to the large natural linewidth of this transition ($\Gamma/2\pi = 32$ MHz) and the geometry, no saturation dips are observed (only a single broad absorption peak).
The Zeeman slower beam, delivered through an optical fiber and collimated using a Schäfter-Kirchhoff collimator (model 60FC-L-4M50L-01), yields a waist of 8 mm, as recommended by AOSense. A slight focusing along the Zeeman slower region enhances the slowing efficiency. Polarization is adjusted via a half-waveplate and a quarter-waveplate placed in front of the Hot window.
The 2D MOT beam requires a 5 : 1 elliptical profile. This is achieved using a pair of cylindrical lenses to expand the horizontal direction. The beam is then split in two using a half-waveplate and a PBS, allowing power balancing. Each resulting beam has its polarization set by an additional waveplates pair. The optical setup of the Zeeman slower, 2D MOT and spectroscopy beams is shown in Fig. 6.4.

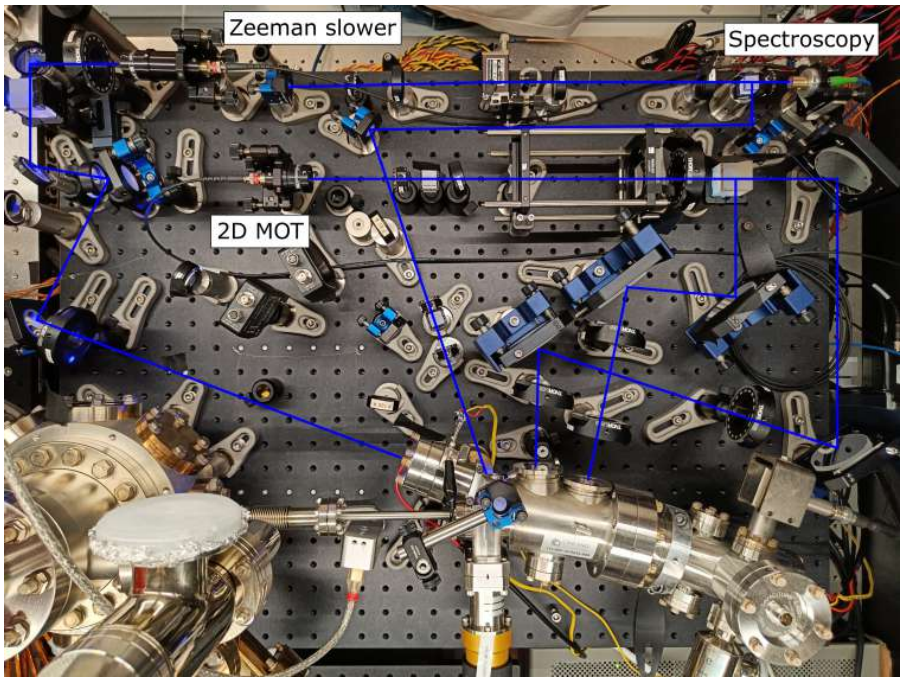

Figure 6.4. Zeeman slower, 2D MOT and spectroscopy optical setup.

The remaining part of the vacuum system consists of a custom octagonal pumping chamber, and a rectangular glass science cell.
The octagonal chamber (pumping chamber in Fig. 6.2) acts as an intermediate section between the atomic source and the science cell, and hosts all the devices required to maintain and diagnose ultra-high vacuum (UHV) conditions, around 8×10^{-12} Torr during standard operation: a NEXTorr D500 StarCell pump, which combines an ion pump and a non-evaporable getter (NEG), and a Bayard-Alpert gauge (UHV-24P,

Agilent), which provides pressure readings in the 10^{-3} to 5×10^{-12} Torr range. Achieving such low pressures requires an initial multistage pumping approach, each stage optimized for a different vacuum regime. More details about the vacuum assembly and bakeout of our system can be found in Ref. [66].
The heart of the experiment is a rectangular fused silica cell, manufactured by Japan Cell, with internal dimensions of 33 mm × 25 mm × 120 mm. The surfaces are optically polished to a flatness of $\lambda/10$, ensuring minimal distortion of the laser beams. The two largest faces are anti-reflection (AR) coated on the external side for the $460 - 815$ nm spectral range at normal incidence (AOI $= 0°$), while all the other surfaces are uncoated. The cell is connected to the octagonal chamber via a glass-to-metal junction mounted on a CF40 flange. This connection allows for a small degree of rotational freedom around the longitudinal axis of the cell. To align the cell correctly, we used a reference blue beam (1 mm waist) and two fixed-height alignment targets. By rotating the flange slightly, we matched the reflections from the glass surfaces to the beam path, ensuring that the optical axis of the cell was parallel to the optical table.

6.2 Magnetic field control

Magnetic field control plays a fundamental role in several aspects of atomic physics experiments. Although the bosonic isotope ^{88}Sr has no nuclear magnetic dipole moment in its ground state and is insensitive to magnetic fields, a precise control of the magnetic field is still essential for multiple operations involving exciting to high-energy states: creating Magneto-Optical Traps (MOTs), shifting the position of the red MOT, driving the atoms to the clock state, and tuning their polarizabilities. To meet these experimental needs, we designed a dual system composed of a pair of high-field coils and a set of three orthogonal compensation coil pairs, all mounted on a dedicated structure surrounding the science cell. The design was guided by the following key requirements:

- the ability to generate a magnetic field gradient exceeding 50 G cm^{-1} in all directions, required for the operation of both blue and red MOTs;
- the ability to reach magnetic fields above 900 G along a single axis, necessary to excite the bosonic isotope on the doubly forbidden clock transition;
- a geometry which maximizes optical access to the atoms through the glass cell;
- independent magnetic field control along all three spatial directions, enabling fine-tuned compensation of ambient stray fields and control of the MOT position;
- high field uniformity over the typical size of a tweezer array (hundreds of micrometers), crucial for experiments involving spatially resolved atom arrays;
- efficient thermal dissipation to minimize resistive heating and avoid temperature-induced misalignment of sensitive optics or air turbulence that could degrade imaging quality.

To achieve these goals, we opted for a pair of custom hollow-core copper coils, which are capable of producing high magnetic fields and can be water-cooled. These coils are currently operated only in anti-Helmholtz configuration to generate the MOT quadrupole field. However, we are developing an H-bridge-like electronic circuit that will allow fast switching between anti-Helmholtz (equal currents in opposite directions) and Helmholtz (equal currents in the same direction) configurations. On top of that three orthogonal pairs of compensation coils are used to cancel residual background magnetic fields and apply controlled bias fields. These are especially useful for precisely positioning the red MOT and for experiments requiring magnetic tuning of atomic states. The two sets of coils are mounted together on an custom 3D printed plastic support that surrounds the glass cell. We used plastic and aluminum mounts to avoid inducing Eddy currents during operation.

6.2.1 High field coils

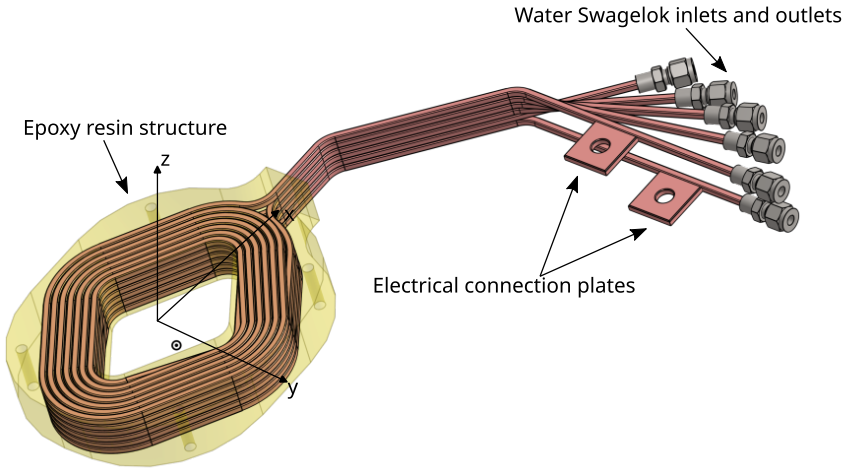

Figure 6.5. CAD rendering of one of the two high field coils: three pairs of layers of windings are embedded in an epoxy resin structure that serves as mounting structure too. The water Swagelok inlets and outlets and the electrical connection plates are visible. The electrical connections between the windings are in series while the hydraulic connections are in parallel. The rhomboidal shape is the one that leaves most of the optical access clear while guaranteeing high and uniform fields (in Helmholtz configuration) and gradients (in anti-Helmholtz configuration) at the center of the glass cell

The high-field coils used in the experiment were designed by me manufactured by Oswald Elektromotoren GmbH. A CAD rendering of one of the two coils is shown in Fig. 6.5. Each coil consists of 7×6 windings of insulated hollow-core copper wire, with a square cross-section of $4\,\text{mm} \times 4\,\text{mm}$ and a circular internal core of 2.5 mm in diameter. The wire is coated with a 0.3 mm thick Kapton insulation layer. Each coil features two connection plates for the power supply (input and output). All the windings are electrically connected in series with electrical connections between the layers. These solder joints were made in the straight sections of the wire located outside the winding structure.

The cooling circuit is divided into three separate sections, each composed of two

winding layers that are connected in parallel. Each section has its own dedicated water inlet and outlet, for a total of three pairs of water connectors. The entire coil core is embedded in an epoxy resin cage, which includes four mounting holes that allow the coils to be assembled together with the compensation coils. The two high-field coils are vertically spaced by 51 mm, this distance is mainly limited by the size of the objectives that have an outer diameter of 44 mm, leaving a 3.5 mm clearance on both sides.

The magnetic field that this system can produce was simulated on COMSOL Multiphysics in a previous work [106], using the AC/DC module and Magnetic Fields interface, which numerically solves Ampère's law via the magnetic vector potential. Three coil geometries were compared: rhomboidal (as built), circular, and elliptical. For all designs, we kept the internal aperture constant along the longitudinal axis of the science cell to ensure comparable optical access. The rhomboidal geometry produced the highest and most uniform magnetic field for the same current in Helmholtz-like configuration. The result of the simulation for the Helmholtz configuration with the rhomboidal geometry are shown in Fig. 6.6. According to the simulations, a field exceeding 900 G can be generated at the center of the coil pair when driven with 190 A (lower than the maximum current of 200 A that our generator can provide). This is sufficient to drive the bosonic clock transition with a Rabi frequency of $\Omega \sim 2\pi \times 10\,\mathrm{kHz}$ for an excitation beam intensity of $I = 10^3\,\mathrm{W\,cm^{-2}}$.

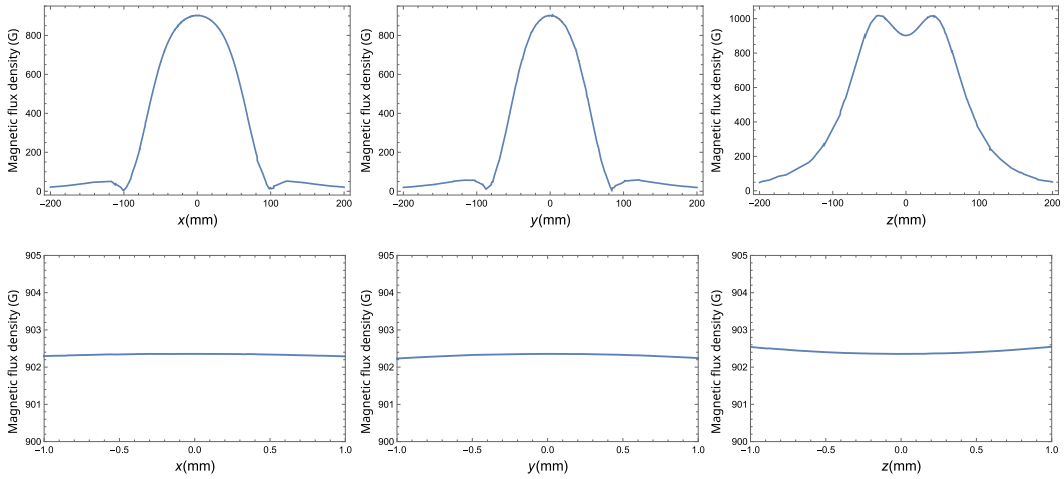

Figure 6.6. Absolute value of the magnetic field profile along three orthogonal axes for the coils in Helmholtz configuration with a current of 190 A and a distance of 51 mm between the two coils.

The field value is uniform around the center, ensuring a high degree of homogeneity across a typical tweezer array. Specifically, for displacements of ±500 µm from the center, the fractional magnetic field variation is $\frac{\Delta B}{B} = 2 \times 10^{-5}$ along the x and y directions, and $\frac{\Delta B}{B} = 4 \times 10^{-5}$ along the z direction. This variation reduces to $\frac{\Delta B}{B} = 1 \times 10^{-5}$ uniformly along all three axes when considering a ±100 µm range, which is closer to the scale of most optical tweezer configurations. Since the Rabi frequency of the clock excitation scales linearly with the magnetic field, we expect a corresponding uniformity in excitation across the array. This level of homogeneity

ensures that magnetic field inhomogeneity contributes negligibly to dephasing effects, provided the tweezers are well centered within the field.
To drive the coils we use a Delta Elektronika SM30200 power supply, capable of delivering up to 200 A at 30 V (6 kW), ensuring sufficient overhead for both Helmholtz and anti-Helmholtz operation. The results of our experimental characterization showed good agreement with the simulations. In the Helmholtz configuration, we verified the linear dependence of the magnetic field on the current by performing a series of measurements, as shown in Fig. 6.7a. The data yields a linear fit with a slope of $5.2\,\mathrm{G\,A^{-1}}$, demonstrating that magnetic fields even higher than 1000 G can be reached at 200 A, which corresponds to the maximum output of the power supply. To further confirm the spatial distribution of the field, we measured its profile along the y-axis at a fixed current of 100 A. Fig. 6.7b shows a comparison with the simulated field, rescaled to the same current. The shape and amplitude of the experimental data match the simulation, with slightly improved performance observed in the measurements.

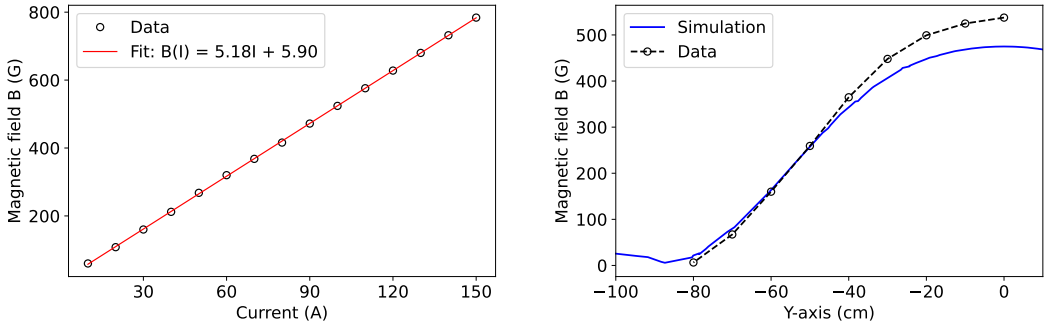

(a) Measured linear response of the coils, producing a magnetic field B proportional to the driving current I in Helmholtz configuration. The slope is $5.2\,\mathrm{G\,A^{-1}}$, allowing us to reach field higher than 1000 G at the maximum current provided by the power supply.

(b) Spatial B field profile along the x-axis for a current of 100 A and the coils connected in Helmholtz configuration. The x-coordinate measures the distance from the coils axis. The experimental data overcome the simulation, meaning that the coils over-perform what we expected from their design.

Figure 6.7. Characterization of the magnetic field generated by the coils in Helmholtz configuration.

The same COMSOL simulations were repeated with the coils driven in anti-Helmholtz configuration (i.e., currents flowing in opposite directions), producing a quadrupole field, Fig. 6.8. Due to the lack of cylindrical symmetry in the rhomboidal geometry, the resulting field gradients differ along the three principal axes. For a current of 190 A, the simulated gradients were $125\,\mathrm{G\,cm^{-1}}$ (x-axis), $90\,\mathrm{G\,cm^{-1}}$ (y-axis), and $215\,\mathrm{G\,cm^{-1}}$ (z-axis). Since the magnetic field scales linearly with the current (as per Biot–Savart law), these values can be proportionally adjusted. For example, even at 100 A, the gradient remains above $50\,\mathrm{G\,cm^{-1}}$ in the weakest direction, meeting the MOT requirements.

We characterized the magnetic field gradients generated by the coils in order to compare the measurements with the simulation also in the anti-Helmholtz configura-

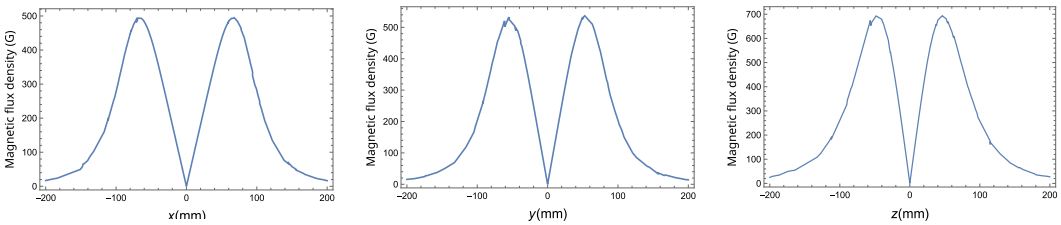

Figure 6.8. Absolute value of the magnetic field profile along three orthogonal axes for the coils in anti-Helmholtz configuration with a current of 190 A and a distance of 51 mm between the two coils.

tion. Measurements carried out at a current of 100 A are shown in Fig. 6.9. The gradients along the three axes slightly exceeded the simulated values in all directions. A summary of the comparison between simulated and measured field amplitudes and gradients, rescaled to 190 A, is reported in Tab. 6.2.

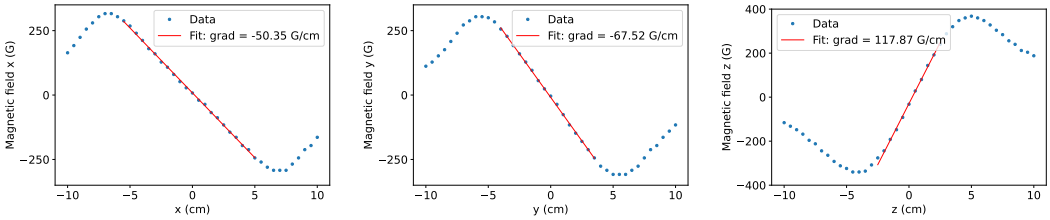

Figure 6.9. Magnetic field measurements along three orthogonal axes for the coils in anti-Helmholtz configuration with a current of 100 A and a distance of 51 mm between the two coils.

	Simulated value	Measured value
B field (Helmholtz)	902 G	988 G
x-axis B gradient (anti-Helmholtz)	125 G cm^{-1}	128 G cm^{-1}
y-axis B gradient (anti-Helmholtz)	90 G cm^{-1}	96 G cm^{-1}
z-axis B gradient (anti-Helmholtz)	215 G cm^{-1}	224 G cm^{-1}

Table 6.2. B field amplitude and gradients comparing the simulations and measurements.

The coil resistance is approximately 60 mΩ, leading to a voltage drop of 11 V and a power dissipation of 2.2 kW at the nominal operating current of 190 A. Such a system cannot be cooled by air; thus, a dedicated water-cooling circuit is necessary. Simulations were carried out to ensure that the capability of the system to effectively cool the coils during operation [106]. Based on the results of these simulations, each coil was designed with three double-winding planes, connected in parallel to the cooling system. This configuration was chosen because, similarly to electrical circuits, operating the cooling circuit in parallel rather than in series reduces the pressure drop (analogous to voltage drop) while increasing the overall water flow rate. The cooling system consists of a P30300 chiller manufactured by Technotrans systems GmbH, connected to a network of pipes and fittings that circulate water through the hollow-core conductors of the coils. The chiller is capable of dissipating up to

3 kW via a water-to-water heat exchange mechanism. Experimental measurements using the full setup, including 20-meter-long, 50 mm^2 cables, yield a total resistance of 75.7 mΩ, which is consistent with the expected value when accounting for contact resistances. At 190 A of continuous current, the power that needs to be dissipated by the cooling system reaches 2.7 kW, with approximately 2.2 kW dissipated within the coil windings. The parallel design permits a total water flow of 4.2 L min^{-1}, with 0.7 L min^{-1} flowing in each of the 6 blocks consisting of two layers of 7 windings, each approximately 3 m in length. COMSOL Multiphysics simulations, as detailed in Ref. [106], suggest that under these conditions (in continuous operation of the coils) the water experiences a temperature rise of 8.4 °C and a pressure drop of 2.2 bar per block. We highlight, however, that the conditions in which this simulation was conducted are extreme compared to the actual operation of the coils, which run at a lower currents and for only a fraction of the experimental cycle.
When operating the coils in anti-Helmholtz configuration, 100 A are sufficient for producing a 50 G cm^{-1} gradient, which is enough for the MOT operation, so the total power dissipation is only 750 W, and the observed temperature increase, monitored with thermistors, remains below 2 °C during experimental use, relative to ambient temperature.
Although the coils have not yet been employed in Helmholtz configuration for clock excitation, they are expected to dissipate the full 2.7 kW when operated at maximum current. However, since the clock excitation is applied in short pulses (∼ 10 ms), the high instantaneous power has a negligible effect on the experimental duty cycle, which typically spans several hundreds of milliseconds. Thus, the available cooling time far exceeds the heating period, ensuring stable thermal performance even under pulsed high-current conditions.
To test the performance of the cooling system under extreme conditions, the coils were operated at a constant current of 190 A for approximately 15 minutes. As

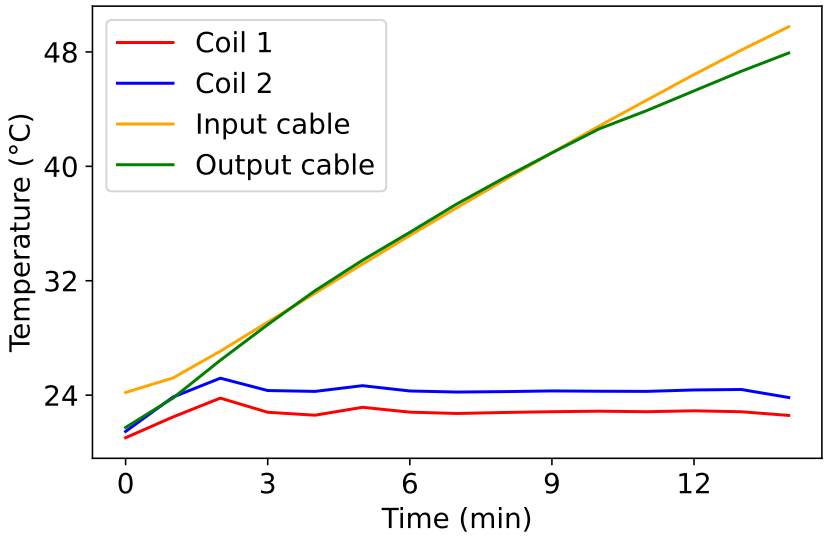

Figure 6.10. Thermal response of coil and cable components under a constant 190 A current. The plot shows temperature variations recorded by four sensors over time.

shown in Fig. 6.10, the temperature of the coils increased by about 4 °C relative to ambient temperature, before reaching a stable plateau thanks to the efficiency of the cooling circuit. In contrast, the temperature of the connecting cables, which are not actively cooled, continues to rise under these conditions, highlighting their thermal limitations. This test was conducted to validate the cooling system's performance under stress, significantly exceeding the conditions expected during normal operation, and confirms its effectiveness in maintaining thermal stability.

6.2.2 Coils control electronics

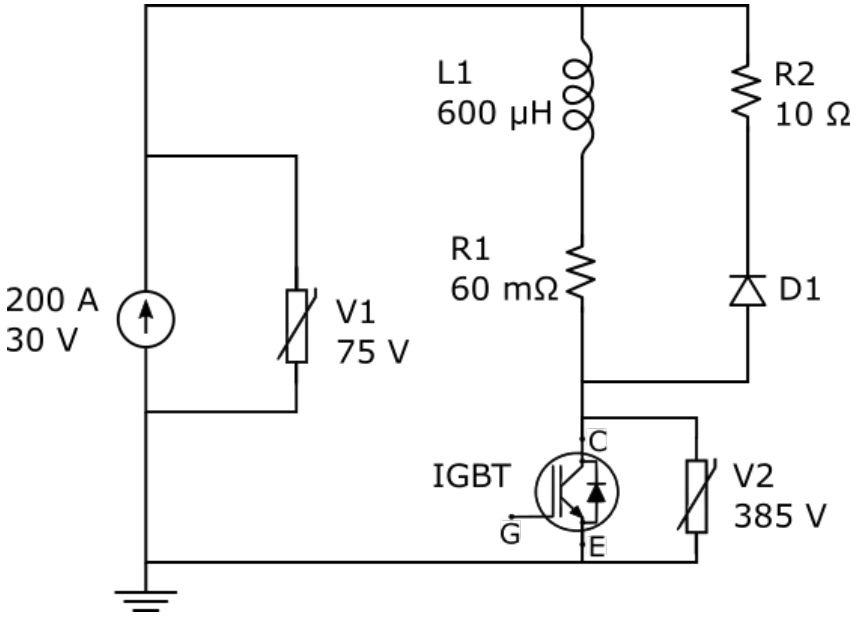

Figure 6.11. Schematic circuit for fast switch-off of the coils. The current generator supplies the coils, represented by the inductance L1 and resistance R1. To control the current flow, an IGBT, which is activated with a control gate voltage, is connected in series. When the IGBT is closed, the current flows through the coils only. By switching the control voltage to open the IGBT, the current starts to flow through R2 too, thus introducing a higher resistance to speed up the circuit discharge

The electrical connection of the windings is made in series: each 2×7 windings block is soldered to the next, as shown in Fig. 6.5. The output of the first coil is connected to the input of the second, forming a single current path. The two coils are powered through a pair of 20 m long cables with a cross section of 50 mm, rated for high voltage and current. These cables were chosen for their low resistance ($0.386\,\Omega\,\mathrm{km}^{-1}$), ensuring only a minor contribution to the total resistance of the circuit. The power supply can deliver up to 200 A and 30 V, which is suitable for our experimental requirements. With a total circuit resistance of 75.7 mΩ, the voltage drop at maximum current reaches approximately 15 V. From preliminary tests, where the coils were connected to the power supply via short cables, we measured a time constant $\tau \sim 9.9\,\mathrm{ms}$ for 60 mΩ, corresponding to an estimated inductance of $L \sim 600\,\mu\mathrm{H}$. This relatively long time constant limits the system's ability to switch off the magnetic field quickly, an important requirement in many atomic physics

experiments. To overcome this limitation, we implemented a fast discharge snubber circuit (shown in Fig. 6.11), which drastically reduces the switching-off time. In this design, the coils are modeled as an inductor L_1 and a resistor R_1, connected in series. When the IGBT (Insulated-Gate Bipolar Transistor) is turned on, the current flows clockwise through the inductor, storing energy in its magnetic field. At this stage, the parallel resistor R_2 (with $R_2 \gg R_1$) is effectively bypassed. When the IGBT is switched off, the current path is interrupted, and the energy stored in the magnetic field is released. This sudden interruption generates a high voltage across the inductor, in accordance with Faraday's Law. The voltage is clamped by a varistor, which becomes highly conductive under such conditions, protecting both the IGBT and the power supply. The current is then redirected through a diode D_1, establishing a counter-clockwise path through the resistor R_2 ($R_2 = 10\,\Omega$), which dissipates the stored energy quickly.
This setup allows for a much faster decay of the current: the discharge time constant is given by $\tau_d = \frac{L_1}{R_1+R_2} \simeq 60\,\mu s$. In practice, the measured switch-off time is around $300\,\mu s$, as shown in Fig. 6.12, likely limited by parasitic elements and transient effects. This fast switching capability is crucial for operations such as turning off the magnetic field between the blue and red MOT stages, or during the imaging process, where residual fields could induce Zeeman shifts.

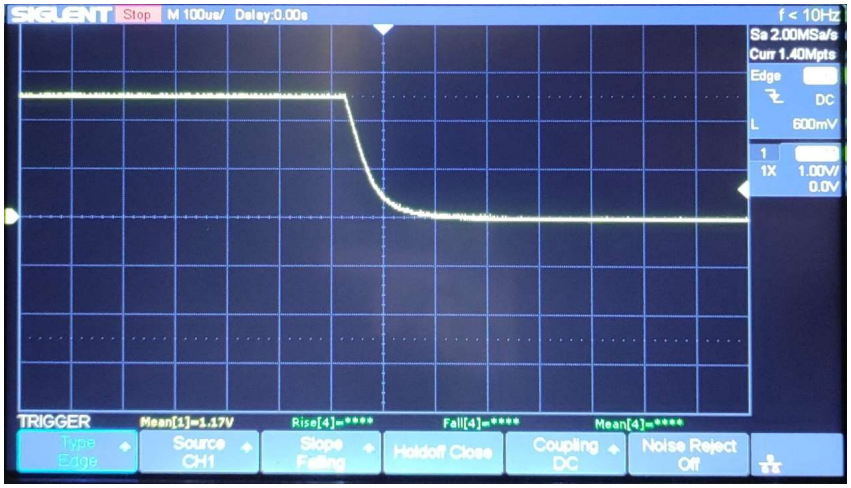

Figure 6.12. Oscilloscope signal of the current in the high-field coils measured with a Danisense DS400UB-10V current probe. The signal shows the rapid switch-off dynamics of the coils using the custom-designed fast switch-off circuit. The current drops to zero within approximately $300\,\mu s$, ensuring complete extinction of the magnetic field for subsequent experimental stages.

To further improve the system's versatility, we are currently developing a new circuit that will not only allow for fast current switch-off, but will also enable dynamic switching between Helmholtz and anti-Helmholtz configurations by reversing the current in one of the coils. This design is inspired by the work of I. Madjarov [48].

A simplified schematic of the intended configuration is shown in Fig. 6.13.
The new design is based on an H-bridge architecture, employing four IGBT switches to fully control the current path through the two coils, each modeled as a series of an inductor and a resistor. Two high-power resistors, R_3 and R_4, will be placed in parallel with the coils to ensure fast energy dissipation during the switch-off phase. The IGBTs are labeled according to their function: HHI and HLO for operating in Helmholtz mode, and AHHI and AHLO for the anti-Helmholtz configuration. By selectively switching the appropriate pair of transistors, it will be possible to invert the current in one coil, allowing seamless transition between the two configurations. This design will enable a fast and flexible control of the magnetic field configuration, removing the constraints imposed by the coil inductance. Its implementation will be essential for future stages of the experiment, particularly when fast switching of the magnetic field is required.

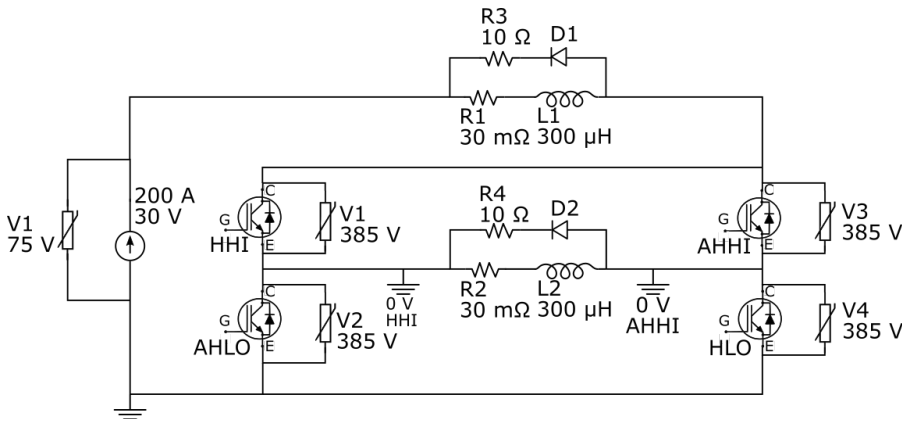

Figure 6.13. Sketch of half of the H-bridge circuit to control the high-field coils. The basic idea is to use separate IGBTs to selectively control the flow through the two coils. When the high-side IGBT (HHI) is closed and the low-side IGBT (HLO) is open, the current flows through both L1 and L2, which represent the two coils separately, in the same direction. If instead HHI is open and HLO is closed, the current will flow in opposite direction through the coils. This will allow us to switch from Helmholtz to anti-Helmholtz configuration, still enabling a fast switch-off of the coils that is achieved by opening both the HHI and HLO.

6.2.3 Compensation coils

A set of three orthogonal pairs of low-field compensation coils is employed both to cancel stray magnetic fields and to apply controlled offset fields. These offset fields are crucial to finely tune the position of the red MOT and to define a quantization axis during the experiment. All coils were hand-wound using single-conductor Kapton-insulated wire on 3D-printed coil holders that allow the three pairs to be mounted orthogonally. Each pair is aligned along one of the laboratory frame axes, where the x axis is horizontal along the glass cell's axis, the y axis lies horizontally along the objective axis and the z axis is vertical. The main properties measured for these coils are reported in Tab. 6.3.
The coils differ in geometry depending on their orientation: the x-axis coils are

rectangular, with inner side lengths of 144 mm × 138 mm and a separation of 192 mm; the y-axis coils are also rectangular, with inner side lengths of 166 mm × 138 mm and a separation of 138 mm; the z-axis coils have an elliptical shape, with inner full major and minor axes of 138 mm and 98 mm respectively, and are separated by 138 mm.

Property	**X coils**	**Y coils**	**Z coils**
Resistance (R)	1.8 Ω	2.5 Ω	2.1 Ω
Time constant (τ)	11.56 ms	12.8 ms	14.35 ms
Number of turns	70	100	120
Nearest separation	192 mm	138 mm	138 mm
Helmholtz field	4.2 G A^{-1}	5 G A^{-1}	7 G A^{-1}

Table 6.3. Properties of the compensation coils.

Each coil pair is independently driven by a low-noise power supply (Delta Elektronika ES 015-10) capable of delivering up to 15 V and 10 A. The current flows in the same direction in both coils of a pair, establishing a Helmholtz configuration that produces a uniform offset magnetic field of a few Gauss at the center. The measured time constant for each pair is on the order of 15 ms, a value that includes contributions from the power supply, whose switching time, as reported in the datasheet, is a few milliseconds.

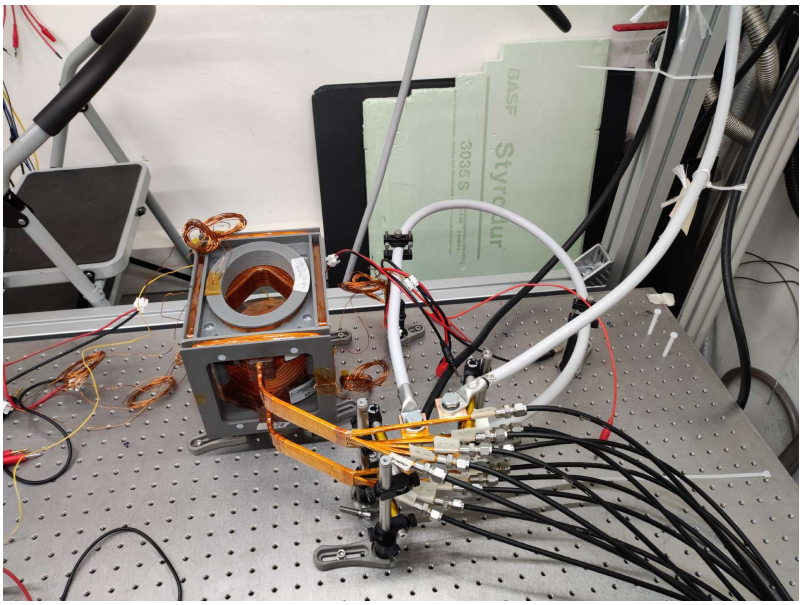

Figure 6.14. Assembly of the magnetic coil system. The high-field coils are mounted on the structure sustained by the three orthogonal pairs of compensation coils. Cylindrical spacers ensure the correct separation between the main coils.

After characterizing the ambient magnetic field at the trap center using a magnetic field probe (Stefan Mayer Instruments FCL 100, with 0.5 mG V^{-1} sensitivity and 2.5 V*range*), the current through the coils can be tuned to apply arbitrary offsets. This is crucial for adjusting the center of the red MOT, which is highly sensitive to

even sub-Gauss fields. Since the MOT is centered at the zero-field point, applying a bias field along any direction displaces this point. If a uniform magnetic offset δB is applied along a direction with a field gradient b, the zero-field position shifts by $\delta x = \frac{\delta B}{b}$. Typical gradients for the red MOT are around 5 $\frac{\mathrm{G}}{\mathrm{cm}}$ in the weakest direction, so a 0.5 G offset moves the MOT by 1 mm along that axis. This displacement capability is essential for overlapping the MOT with the tweezer array. However, the high sensitivity also implies that any noise in the applied field causes fluctuations in the MOT position. For this reason, the use of low-noise power supplies is critical. In contrast, the blue MOT, which operates at a magnetic gradient approximately 10 times higher, is much less sensitive to field offsets.
The main high-field coils and the low-field compensation coils are integrated into a single structure, which is built upon the custom 3D-printed supports used to wind the wires. The complete assembly is shown in Fig. 6.14. The compensation coils along the three axes are wound in advance and serve as a mechanical support for the high-field coils, which are positioned with a fixed separation of 51 mm using four cylindrical spacers.

6.3 Laser system and stabilization

In this section I will describe the laser systems employed in the experiment. At present we are using:

- a blue laser, addressing the $^1\mathrm{S}_0 \rightarrow {}^1\mathrm{P}_1$ transition at 461 nm;
- a red laser for the $^1\mathrm{S}_0 \rightarrow {}^3\mathrm{P}_1$ transition at 689 nm;
- a tweezer laser at 813 nm, far-detuned from any transition, used for optical dipole trapping;
- an UV laser tunable between 316 nm and 319 nm, employed for the excitation to Rydberg states;
- two repumper lasers at 679 nm and 707 nm used for repumping the atoms from the $^3\mathrm{P}_0$ and $^3\mathrm{P}_2$ states in order to close the cooling cycle by depopulating the dark state when performing the blue MOT.

In the near future, a laser addressing the clock transition will also be integrated into the system.

6.3.1 Blue 461 nm laser

The blue laser system, addressing the $^1\mathrm{S}_0 \rightarrow {}^1\mathrm{P}_1$ transition at 461 nm, is based on an Injection-Locked Amplifier (ILA) laser system manufactured by MOGLabs. The seed source is a Nichia NDB4916T diode, tunable between 450 nm and 465 nm, delivering up to 250 mW in an external cavity diode laser (ECDL) configuration. About 30 mW of this output are used to injection-lock the ILA diode, while the remaining $\sim$ 200 mW are available from a separate port on the chassis. The ECDL is typically driven at 290 mA, while the ILA diode operates at 700 mA, producing over 650 mW of laser power, delivered via an optical fiber.

A schematic of the optical layout is shown in Fig. 6.15. Two main branches are derived: one from the ECDL (seed) and one from the amplified output (ILA). Both beams are shaped to have a nearly Gaussian, circular profile with a waist of approximately 1 mm. On the seed side, one branch is sent to a wavelength meter (WS8-10 by HighFinesse, 10 MHz absolute accuracy) to monitor the free-running laser frequency. A second branch is sent to the main optical table for Doppler-free spectroscopy on the AOSense Strontium source, providing the error signal for laser locking. The final branch is used to generate the beams for the 2D MOT delivering 30 mW after the optical fiber on the experiment table.
The ILA output is primarily used to generate the high-power beams for the Zeeman slower ($\sim$ 60 mW) and the 3D MOT ($\sim$ 20 mW), delivered through optical fibers to the main table. Two additional branches serve as imaging beams: one for time-of-flight absorption imaging of the blue and red MOTs, and the other for fluorescence imaging of atoms trapped in tweezers. The latter is slightly red-detuned to compensate for the light shift induced by the tweezers. Both imaging beams deliver $\sim$ 0.5 mW on the experiment side.

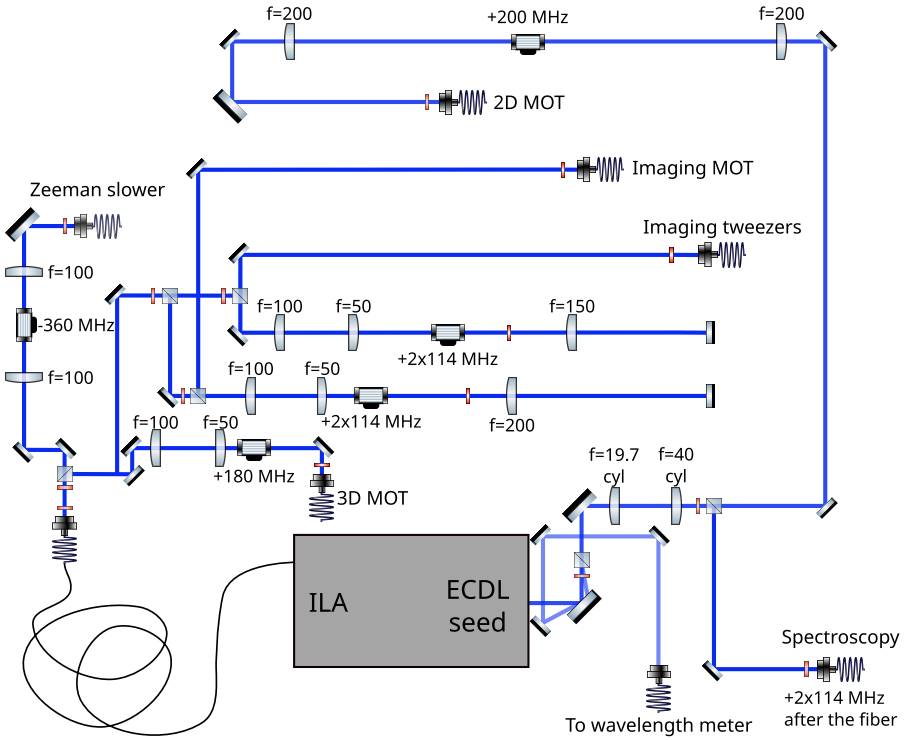

Figure 6.15. Schematic layout of the optical setup for the 461 nm laser.

The laser is frequency-locked to the atomic transition by modulating the diode current at 250 kHz and scanning the piezo of the external cavity. The spectroscopy signal is detected with a balanced photodiode, and demodulated by the ECDL driver to produce a dispersive error signal. A built-in PID controller acts on both current and piezo to stabilize the laser frequency. PID parameters are tunable directly from the laser controller.
To achieve the large detuning required for the Zeeman slower (-580 MHz), we lock

the laser about 230 MHz below resonance and use a single-pass AOM at 350 MHz (model 3350-199 by G&H), operating on the -1 diffraction order. This strategy avoids the need for double-pass AOMs, which typically have lower efficiency, and higher-frequency AOMs, which are more lossy. The spectroscopy and imaging branches use double-pass AOMs centered at 110 MHz (model 3110-120 by G&H), while the 2D MOT and 3D MOT beams use single-pass AOMs at 200 MHz (model 3200-121 by G&H), all operated in the +1 order. The exact driving frequencies used for each AOM are indicated in Fig. 6.15.

6.3.2 Red 689 nm laser

The red laser used to address the $^1S_0 \rightarrow {}^3P_1$ intercombination transition at 689 nm is a Titanium:Sapphire (Ti:Sa) laser system from MSquared, composed of a SolsTiS pumped by an Equinox laser. The pump source delivers up to 18 W at 532 nm, which is used to excite the Ti:Sa crystal emitting tunable radiation in the red to near-infrared (NIR) range. The output frequency is selected and stabilized via intracavity optical elements, including birefringent filters and an etalon. A Ti:Sa laser was chosen to have low phase noise at high frequencies matching the Rabi frequencies [107]. Under typical operating conditions 100 mW of optical power at 689 nm are sufficient to lock the laser to an ultra-low expansion (ULE) cavity, operate the red MOT, perform Sisyphus cooling in the optical tweezers, and simultaneously monitor the frequency on a wavelength meter. However, for the for two-photon Rydberg excitation (see Sec. 5.2), higher power is required to achieve a high Rabi coupling. In such cases, the system can be pushed to its full capacity, yielding up to 1.3 W of red light when pumped at maximum power.
The optical setup for this laser is illustrated in Fig. 6.16. The output is split into several branches: one for frequency locking to the ULE cavity, one for the 3D MOT, one for Sisyphus cooling, one for the two-photon Rydberg excitation scheme, and a final one for the wavelength meter.

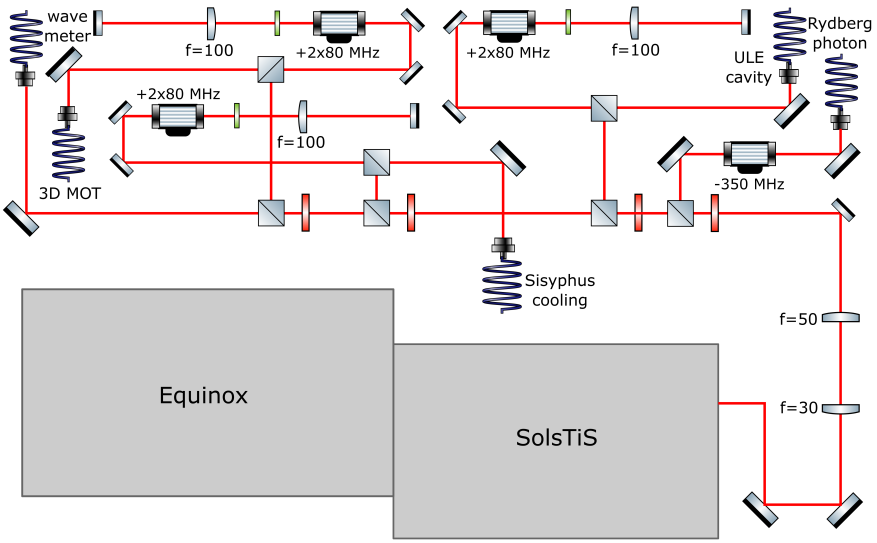

Figure 6.16. Schematic layout of the optomechanic setup for the 689 nm laser.

The ULE lock, Sisyphus cooling, and MOT branches are frequency-shifted using a double-pass AOM at 80 MHz (model 3080-125 by G&H). The Rydberg excitation branch uses a single-pass AOM at 350 MHz (model 3350-199 by G&H). The wavelength meter branch does not include any frequency shifting, providing a direct reading of the laser frequency. The frequency stabilization of the red laser is achieved via Pound-Drever-Hall (PDH) locking technique [108] to a notched ultra-low expansion (ULE) optical cavity manufactured by Stable Laser Systems. The cavity has a length $L = 100\,\text{mm}$, and its mirrors are coated for high reflectivity at 633 nm, 689 nm, and 698 nm, allowing simultaneous stabilization of the red MOT laser, the clock laser, and the Rydberg excitation laser. The latter, in particular, benefits from this design since the UV light is generated through two sequential SHG stages, with an intermediate wavelength around 633 nm (see Sec. 6.3.4), well within the coating range of the cavity. The cavity is housed under ultra-high vacuum at a pressure of 1×10^{-7} Torr and thermally shielded by two nested in-vacuum layers. These thermal shields feature a time constant exceeding 30 hours, ensuring highly stable temperature control. The cavity operates at its zero thermal expansion point, which, in our system, corresponds to 37.63 °C. Laser stabilization is realized using the PDH technique, which employs the optical resonance of the cavity as a frequency discriminator. A phase modulation at $f_1 = 8\,\text{MHz}$ is applied to the laser light via a fiber-coupled electro-optical modulator (EOM, model PM705b by Jenoptik). The resulting modulated light contains a carrier and sidebands, which interact with the cavity modes. The reflected signal, detected by a fast photodiode, is demodulated to obtain a dispersive error signal proportional to the laser–cavity detuning. This signal is then processed by a PID controller and fed back to the laser via two piezoelectric actuators mounted on an internal cavity mirror. The "slow piezo" features a range of $\pm 15\,\text{GHz}$ with a tuning sensitivity of $1.5\,\text{GHz}\,\text{V}^{-1}$, effective up to 50 Hz , while the "fast piezo" operates within $\pm 40\,\text{MHz}$, at $4\,\text{GHz}\,\text{V}^{-1}$, and responds up to 100 kHz. To compensate for the offset between the cavity resonance and the atomic transition frequency, an offset sideband locking scheme is employed. An additional modulation at $f_2 = 643\,\text{MHz}$, generated by a Marconi 2019A signal generator, is combined (with a power combiner Minicircuits ZFSC-2-4+) with the 8 MHz PDH modulation and sent to the EOM. This effectively generates two new sideband triplets centered at offset frequencies, one of which is locked to a cavity mode, enabling fine frequency control relative to the atomic transition (Fig. 6.17a). Given the cavity's free spectral range of 1.5 GHz, this approach allows us to bridge up to 750 MHz between a TEM00 cavity mode and the atomic resonance. The performance of the locking system has been characterized by measuring the frequency noise spectrum of the laser after the PID loop is engaged. As shown in Fig. 6.17b, three components are evaluated: the electronic noise floor (photodiode and electronics only), the amplitude noise (including residual reflected light not involved in the lock), and the actual locked laser spectrum. The *Beta Line* [109] provides a threshold above which the frequency noise contributes to the linewidth. In our system, the frequency noise stays below this threshold for Fourier components above 500 Hz, consistent with a sub-kHz linewidth and sufficient for addressing the 7.6 kHz-wide red transition. Nonetheless, for applications requiring narrower linewidths—such as interrogation of the clock transition in Strontium—an improved lock system with reduced low-frequency noise will be required. The present low-frequency noise is already approaching the limit

imposed by the electronics, setting a lower bound on further improvements.

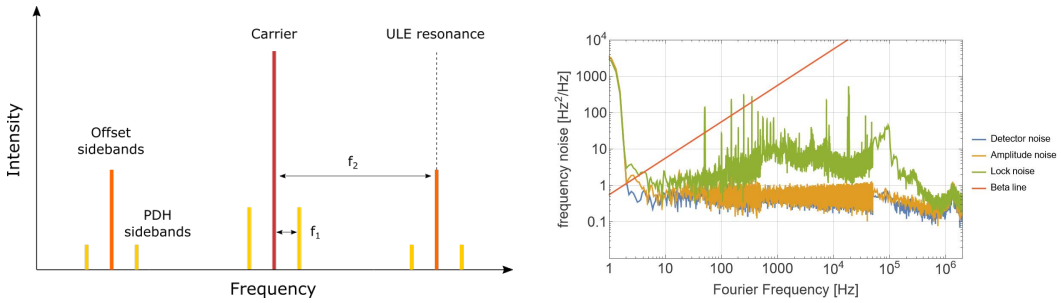

(a) Illustration of the frequency components generated for offset Pound-Drever-Hall locking. A high-frequency modulation at 643 MHz creates two main offset sidebands, each with a standard PDH sideband structure at 8 MHz. This configuration enables locking the laser to a cavity mode located up to 750 MHz away from the atomic resonance.

(b) Frequency noise power spectral density of the red laser locked to the ULE cavity via PDH technique. This spectrum is compared to the electronic noise and the amplitude noise of the circuit. The Beta Line indicates the noise level above which frequency noise contributes to the laser linewidth. In our case, the spectrum stays below the Beta Line above 500 Hz, corresponding to a linewidth sufficiently small to address the 7.6 kHz-wide red transition.

Figure 6.17. 689 nm laser frequency stabilization scheme using PDH locking to a ULE cavity (left) and corresponding frequency noise spectrum (right).

6.3.3 Tweezer 813 nm laser

The laser used to generate the optical tweezers at 813.4 nm is a Matisse by Sirah, a Ti:Sa laser pumped with 25 W of green light at 532 nm produced by a Millennia EV25S (Spectra-Physics Inc.). Up to 7.5 W of infrared power can be coupled into a photonic crystal fiber (LMA-PM-10 by NKT Photonics), which delivers the tweezer light to the experiment table. An acousto-optic modulator (AOM) placed before the fiber is used to control the power and can also act as a fast switch. The dipole traps are created using far-off detuned light; however, for stability reasons, the laser is locked in both power and frequency. The frequency lock is implemented using a HighFinesse WS8-2 wavelength meter, which provides the wavelength reading to the Matisse electronics that has a PID system for stabilization. The power lock is implemented by sampling the light after the output fiber and using a PID controller that sends a feedback signal to the RF generator, thereby adjusting the RF power driving the AOM located before the fiber.

6.3.4 Rydberg UV laser

To generate the UV light required for Rydberg-state excitation, we employ an infrared laser whose frequency is quadruplicated using a custom-built setup with two cascaded second-harmonic generation (SHG) stages.
The source laser is a VECSEL from Vexlum (model VALO SF), which is tunable in

the $1266 - -1276$ nm range and emits approximately 1.1 W of infrared power. The wavelength tuning range is halved after each SHG stage, as the frequency is doubled. Consequently, the light output from the final frequency-quadrupling (FHG) module can be tuned between Rydberg excitation starting from both 316.5 nm and 319 nm. This range allows us to span the energy difference between the $^3P_0$ and $^3P_1$ states, making both excitation schemes discussed in Sec. 5.2 accessible.
The FHG module is manufactured by Leos S.r.l. and uses the Hänsch–Couillaud locking technique [110] to maintain the SHG cavities on resonance with the laser frequency. A small portion of the 633 nm light (produced after the first SHG stage) is picked off before the second doubling stage and will be used to stabilize the laser frequency to the ULE cavity. We obtain about 110 mW of UV power from the FHG module. Since optical elements for UV light typically introduce a few percent loss per element, we have designed the beam path to include as few optical components as possible. This also reduces the risk of UV photon scattering, which is both hazardous to the experimentalists and detrimental to the experiment, even with appropriate shielding. For this reason, both the VECSEL and the FHG module are placed directly on the main optical table, minimizing the beam path length and eliminating the need for optical fibers. An AOM will be used as a fast switch and to control the laser power. The beam will be shaped into a light sheet to increase the intensity on the atoms and will be initially overlapped with *the*689 nm to implement the two-photon excitation scheme.

6.3.5 Repump lasers

We employ two repump lasers at 679 nm and 707 nm to depopulate the metastable $^3P_0$ and $^3P_2$ states, thereby closing the cooling cycle and preventing atoms from being lost into dark states during operation of the blue MOT (see Sec. 3.2). Both lasers are Toptica DLC pro systems, each delivering approximately 20 mW of power at their respective wavelengths. Each laser beam passes through an AOM for fast switching and intensity control. After modulation, the two beams are combined using a polarizing beam-splitter cube and coupled into a single optical fiber, which delivers around 5 mW of power for each wavelength to the main optical table, where the light is directed toward the science cell. The inclusion of these repumpers is crucial for enhancing the efficiency of the MOT, as they increase the number of trapped atoms by an order of magnitude by maintaining a closed cooling cycle (See Sec. 7.3).

6.4 Control System

In this section I briefly introduce the framework used for experimental control.
The experimental sequence is entirely managed using the Labscript Suite [111], an open-source framework, relatively recent, written in Python and designed to automate laboratory experiments, especially in atomic, optical, and quantum physics. It is widely used in laboratories that require precise control of devices such as AOMs, lasers, DAC/ADC modules, digital triggers, and so on.
Labscript is composed of four main Graphical User Interfaces (GUIs), each with a different role:

- BLACS (Buffered Laboratory Acquisition and Control System) is the component responsible for the direct interface between the software and the experimental hardware. Its main function is to execute the experimental sequences compiled in Python with precise, synchronized timing, sending control signals to all involved devices (such as NI-DAQ boards, digital signal generators, DDSs or lasers). Through a modular GUI, BLACS allows both automatic sequence execution and manual control of digital and analog lines, enabling direct intervention on devices between experimental shots. Each device is handled independently through separate threads. It is, therefore, the operational core of the Labscript system, where the logic written in code is actually translated into physical actions on the experimental setup.

- Runmanager is dedicated to managing experimental parameters. Its main function is to allow the definition, modification, and combination of variables used in the Python control code to generate experimental sequences. Through an intuitive graphical interface, it is possible to specify numerical, logical, or textual parameters, and to easily create multidimensional scans. Runmanager then injects these values into the code at compilation time, allowing automated execution of entire series of experiments with different configurations. All used parameters are saved in the output files (.h5), ensuring traceability and reproducibility of the collected data.

- Visualmanager is a graphical component used to visually represent the timing phases of an experiment controlled by Labscript. It is mainly used for debugging and analysis: it clearly shows when digital or analog signals are activated or acquisitions occur, according to the script that has been executed.

- Lyse is the Labscript Suite module dedicated to automatic data analysis. Its main function is to execute one or more Python analysis scripts immediately after the acquisition of data from each experimental shot. These scripts have access to both the parameters with which the shot was generated (i.e., the ones set in the Labscript control script) and the acquired data, such as images or analog signals. Lyse allows real-time monitoring of the experiment's progress, observation of trends, execution of fits, statistical analysis, and quantitative evaluations, all without the need for manual intervention between execution and data processing. Additionally, Lyse can provide feedback on parameters for the next experimental run, enabling automated adjustments or optimization of the experimental sequence based on the most recent results.

Chapter 7

Two-stage MOT of ^{88}Sr

This chapter is based on the publication under review: **V. Giardini**, L. Guariento, A. Fantini, S. Storm, M. Inguscio, J. Catani, G. Cappellini, V. Gavryusev, and L. Fallani, *"Single Strontium Atoms in Optical Tweezer Arrays for Quantum Simulation," arXiv*:2510.19816 [physics.atom-ph] (2025), `https://doi.org/10.48550/arXiv.2510.19816`.

In order to cool and trap Strontium atoms we exploit two magneto-optical traps (MOTs) operating on two optical transitions with very different linewidths. The first one is the broad $^1S_0 \rightarrow {}^1P_1$ transition at 461 nm (blue MOT), which provides a large capture velocity, allowing efficient loading of atoms from a thermal source. However, the Doppler limit associated with this transition is relatively high ($T_D \approx 770\,\mu K$). To further cool the atoms we exploit the narrow $^1S_0 \rightarrow {}^3P_1$ intercombination transition at 689 nm (red MOT), which allows us to reach µK temperatures and higher densities. However, the capture velocity of this transition is extremely small, which prevents direct loading of atoms from the blue MOT. To overcome this problem, we employ an intermediate stage of trapping: the broadband red MOT. We artificially broaden the laser spectrum in this stage to bridge the gap between the broad blue MOT and the narrow single-frequency red MOT, ensuring efficient transfer of atoms between the two. As a result we are able to generate a cold and dense atomic ensembles in the single-frequency red MOT, with phase-space densities enabling efficient loading of the atoms in optical tweezers.

7.1 Optical setup

The optical setup for the operation of the blue and red 3D magneto-optical traps are assembled directly on the main optical table, which is organized into three vertical levels, as schematically illustrated in Fig.7.1.
The trapping beams for both the blue and the red MOT are derived from a single polarization-maintaining fiber in each case, providing beams with a waist of $w_0 = 8\,mm$. Their power, maintained by measuring the intensity of pick-up beams, is actively stabilized by a feedback system based on a PID controller, which regulates the RF drive power of AOMs placed before the fibers. Using polarizing beam splitters (PBSs) in combination with half-waveplates ($\lambda/2$), the beams are split into three

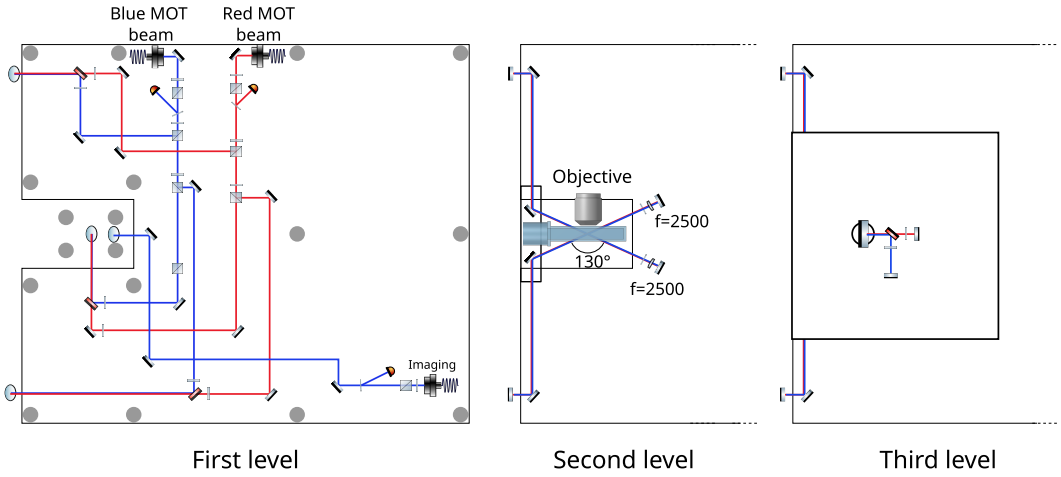

Figure 7.1. Layout of the optical setups for blue and red 3D MOT. In the **first level** both the blue and red MOT laser beams originate from a single optical fiber each. A small fraction of the laser power is sent to a photodiode for monitoring and feedback stabilization. Each beam is split into three branches (one for each spatial direction) using $\lambda/2$ waveplates and PBSs. Three dichroic mirrors overlap the blue and red paths, which are then directed vertically via periscopes to the higher levels. The blue imaging beam for absorption imaging is also integrated at this stage, monitored and stabilized, and sent vertically through another periscope. The **second level** hosts the glass cell, where the experiment is performed. Here, the two horizontal MOT branches intersect at 130° (instead of 90°), due to the size of the microscope objective. Two achromatic $\lambda/4$ waveplates rotate the polarization of both lasers before retro-reflection and two long-focal-length lenses ($f = 2500\,\mathrm{mm}$) refocus the reflected beams to compensate for intensity losses ($\sim 16\%$) caused by the large incidence angle on the cell. On the **third level**, the periscope collects the vertical 3D MOT beams, which are then separated by a dichroic mirror and are retro-reflected separately: $\lambda/4$ waveplates provide opposite polarization upon reflection, while a $\lambda/2$ waveplate allow for fine polarization tuning of the blue beam. The absorption imaging beam is detected with a Basler camera (Basler Ace acA4024-29um) installed on the bottom of the third level breadboard (not shown here).

orthogonal directions required to form the MOT. These beams are then recombined with dichroic mirrors and brought to the level of the science cell using periscopes. Both the blue and red MOTs are realized using three retro-reflected beams, which simplifies the optical layout and reduces the total laser power requirement by half, as compared to a six-beam independent configuration. The horizontal confinement beams enter the cell with an angle of 130°, instead of the conventional 90°, due to the presence of the high-NA objective which limits optical access on the horizontal plane (see Fig. 7.1). Because of the large incidence angle on the glass cell, the horizontal beams suffer a power loss of about 16%. To compensate for this effect, two long-focal-length lenses ($f = 2500\,\mathrm{mm}$) are placed in front of the retro-reflecting mirrors. These slightly reduce the beam waist at the MOT position, thereby restoring the intensity balance between the incoming and retro-reflected beams. The retro-reflected path also includes a double pass through an achromatic quarter-waveplate to rotate the polarization. The vertical confinement beams are separated in the third optical level by means of a dichroic mirror and are independently retro-reflected

after their polarization is flipped to the opposite state by a double passage in a quarter-waveplate.
The absorption imaging beam is integrated into the same optical setup. It exits from a fiber with a waist of $w_0 = 1\,\mathrm{mm}$ and, without additional shaping, is delivered to the science cell via a periscope. The transmitted light is collected with a Basler Ace acA4024-29um camera installed on the bottom of the third level breadboard (not shown in the figure). A magnetic field gradient of $50\,\mathrm{G\,cm^{-1}}$ produced by the high-field coils, described in Sec. 6.2.1, ensures efficient trapping.

7.2 Atom number and temperature

A quantitative characterization of a MOT requires knowledge of both the atom number and the cloud temperature. These quantities can be extracted from absorption images of the expanding cloud after a variable time of flight (TOF). Absorption imaging is one of the standard diagnostic tools in ultracold atom experiments, as it directly detect the spatial distribution of the sample and allows reliable determination of its size, atom number, and temperature [112, 113].
We use the 461 nm imaging beam to perform absorption imaging, which is tuned to be resonant with the $^1\mathrm{S}_0 \rightarrow {}^1\mathrm{P}_1$ transition. The trapping beams and the magnetic field gradient confining the atoms are instantaneously switched off, leaving the atoms to freely expand and fall under gravity, then the resonant light pulse is sent onto the atomic cloud. As the probe beam passes through the cloud, the atoms absorb light and imprint their spatial distribution onto the transmitted intensity, which is then imaged by the camera. For each experimental cycle, three images are acquired:

- Signal image (S): the probe beam transmitted through the atomic cloud, with the atomic shadow;
- Probe image (P): the probe beam without atoms, representing the incident intensity profile;
- Background image (B): recorded without atoms and without probe light, used to remove the background offset from the camera.

The atom number in the cold cloud can be extracted as [114]:

$$N = \frac{A}{\sigma(\Delta)} \sum_{x,y} \log\left(\frac{S_{x,y} - B_{x,y}}{P_{x,y} - B_{x,y}}\right), \tag{7.1}$$

where A is the pixel area, $\sigma(\Delta)$ is the absorption cross section, and $S_{x,y}$, $P_{x,y}$, $B_{x,y}$ are the pixel intensities of the three images at coordinates (x, y).
The absorption cross section is given by:

$$\sigma(\Delta, s) = \frac{3\lambda^2}{2\pi}\left(\frac{1}{1 + \left(\frac{2\Delta}{\Gamma}\right)^2}\right)\left(\frac{1}{1+s}\right), \tag{7.2}$$

where Δ is the detuning, s is the saturation parameter, λ is the wavelength, and Γ is the natural linewidth of the transition.

The attenuation of the probe beam is described by the Lambert-Beer law, which relates the transmitted intensity $I_t(x, y)$ to the incident probe intensity $I_0(x, y)$ via the optical density $\alpha(x, y)$:

$$I_t(x, y) = I_0(x, y)e^{-\alpha(x,y)}, \qquad \alpha(x, y) = \sigma\tilde{n}(x, y), \tag{7.3}$$

where $\tilde{n}(x, y) = \int n(x, y, z)dz$ is the atomic density integrated along the imaging axis z.
From this relation, the atomic density can be obtained directly as:

$$\tilde{n}(x, y) = -\frac{1}{\sigma}\log\left(\frac{I_t(x, y)}{I_0(x, y)}\right). \tag{7.4}$$

We obtain the atom number by fitting the absorption profile with a two-dimensional Gaussian (with σ_x^2, σ_y^2 variances), which after integration yields:

$$N = 2\pi\sigma_x\sigma_y\frac{n_0}{\sigma(\Delta)} \tag{7.5}$$

where n_0 is the optical density peak.
We acquire the absorption images 300 µs after switching off both the trapping beams and the magnetic field. This delay is necessary to ensure a complete turn off of the magnetic field and avoid any Zeeman shifts that could otherwise affect the absorption cross section. An example of such an image, together with the fitted Gaussian profiles, is shown in Fig. 7.2.

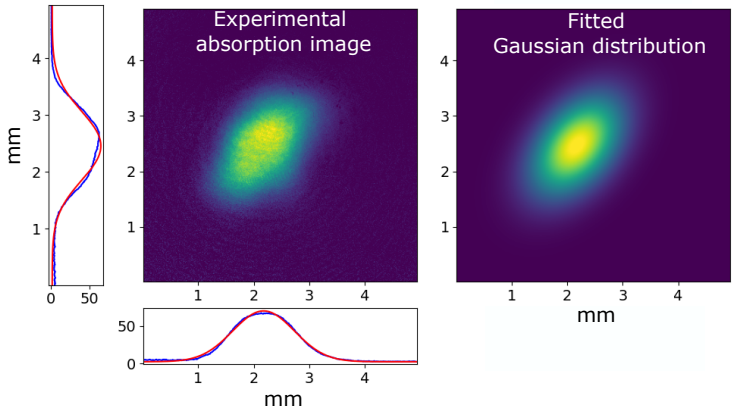

Figure 7.2. Absorption image of the blue MOT after 300 ms TOF. **Left**: Experimental image of the atomic cloud together with one-dimensional cuts along the x and y axes (blue) and fit with a rotated Gaussian (red). **Right**: Two-dimensional Gaussian fit used to extract the atom number and spatial widths. From the fit we obtain $N = 1.25 \times 10^7$ atoms, a 3D peak density of $3.8 \times 10^9\,\mathrm{cm}^{-3}$, and cloud sizes of $\sigma_x = 1.64(2)$ mm and $\sigma_y = 1.69(2)$ mm.

To measure the MOT temperature, we release the atoms from the trap and record the expansion of the cloud for different TOF, as shown in Fig. 7.3. The increase in cloud size with TOF is then used to extract the atomic temperature.
Since we are well above the regime of quantum degeneracy, the atomic velocity

distribution in the MOT follows a Maxwell–Boltzmann distribution, leading to a density profile at TOF t of the form [114]:

$$\tilde{n}(x, y, t) \propto \exp\left(-\frac{(x - x_0)^2}{2\sigma_x^2(t)} - \frac{(y - y_0)^2}{2\sigma_y^2(t)}\right),$$

with

$$\sigma_i^2(t) = \sigma_{0i}^2 + \sigma_v^2 t^2, \qquad \sigma_v^2 = \frac{k_B \mathrm{T}}{M}.$$

Here, $\sigma_i(t)$ is the cloud size along the i-axis at time t, which grows from the initial size σ_{0i} at $t = 0$ due to the thermal expansion characterized by σ_v. By measuring the cloud size at different TOFs, we can extract $\sigma_{v_x}^2$ and $\sigma_{v_y}^2$.
Experimentally, we verify that $\sigma_{v_x}^2 = \sigma_{v_y}^2$ within the measurement uncertainties, allowing us to obtain a more accurate determination of the MOT temperature from the average value $\sigma_{\mathrm{avg}}^2 = \frac{1}{2}(\sigma_{v_x}^2 + \sigma_{v_y}^2)$. By fitting the functional form of $\sigma_{\mathrm{avg}}(t)$ to the experimental data, we can extract the temperature of the MOT.

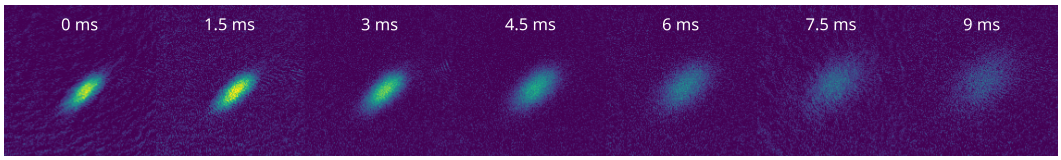

Figure 7.3. TOF images of the atomic cloud after release from the red MOT, taken at increasing expansion times from 0 to 9 ms. The growth of the cloud size with TOF is used to extract the temperature via Gaussian fits to the optical density profiles.

7.3 First Stage of Trapping: The Blue MOT

The first stage of atomic trapping is provided by the blue MOT, which operates on the ${}^1\mathrm{S}_0 \rightarrow {}^1\mathrm{P}_1$ transition at 461 nm. To enable efficient trapping, the atomic beam emerging from the oven is first decelerated using a combination of a Zeeman slower and transverse cooling that we refer to as 2D MOT. These elements perform longitudinal slowing and transverse cooling, while simultaneously deflecting the atomic beam toward the trapping region. Both the Zeeman slower and the 2D MOTs are integrated into the atomic source, as described in Sec. 6.1.
The atomic oven is operated at a temperature of 420 °C, which represents an optimal compromise between providing a sufficiently high atomic flux for robust MOT loading and ensuring a long operational lifetime of the atomic source. Based on our estimates, operating at this temperature allows for a daily use over a period of approximately ten years before depletion of the atomic reservoir. While higher oven temperatures would increase the atomic flux and consequently the MOT population, this would come at the cost of significantly reducing the lifetime of the source.

The blue 3D MOT in the glass cell was optimized by scanning the key experimental parameters affecting its performance, including the quadrupole magnetic field gradient, as well as the power and detuning of the 3D MOT beams, the 2D MOT beams, and the Zeeman slower. The goal was to maximize both the total number of trapped atoms and the peak atomic density. Further details on these

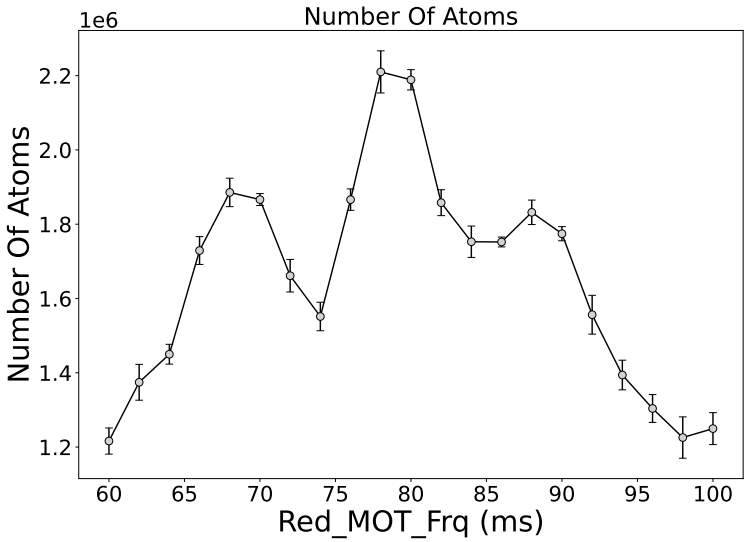

Figure 7.4. Relative enhancement of the atom number by the red-shielding beam as a function of the frequency detuning from resonance, assuming the far from resonance values as baseline.

parameter scans can be found in [66].
The optimal parameters for our setup were determined as follows: for the 2D MOT beams, the optimal powers are 9.4 mW ($s = 0.11$) and 4.7 mW ($s = 0.055$) for the two paths, with a common detuning of $-0.7\,\Gamma_{^1\mathrm{P}_1}/2\pi = -22$ MHz. The Zeeman slower optimal power is 40 mW ($s = 0.93$) with a detuning of $-19\,\Gamma_{^1\mathrm{P}_1}/2\pi = -580$ MHz. For the 3D MOT, the optimal power is 4.3 mW per beam ($s = 0.1$) with a detuning of $-2\,\Gamma_{^1\mathrm{P}_1}/2\pi = -60$ MHz relative to the atomic resonance. These values were chosen to be compatible with the total laser power available in our system. The optimal magnetic field gradient, providing the best compromise between atom number and density, was found to be 50 G cm^{-1}.

To further enhance the number of trapped atoms we exploit the Shielding effect [115]. This technique involves resonantly driving the red $^1\mathrm{S}_0 \rightarrow ^3\mathrm{P}_1$ transition during the blue MOT loading phase. In a highly saturated regime, the 689 nm light maintains the atoms in the 3P1 state for half of the time. This effect yields a 80% improvement in atom number with respect to the unshielded configuration (see Fig. 7.4).
Under these optimized conditions, we achieve a MOT with 1.25×10^7 atoms at a peak density of 3.8×10^9 cm^{-3}, as shown in Fig. 7.2.

Although the $^1\mathrm{S}_0 \rightarrow {}^1\mathrm{P}_1$ transition at 461 nm is nearly closed, atoms in the excited $^1\mathrm{P}_1$ state can decay into the $^1\mathrm{D}_2$ level, which subsequently can populate the $^3\mathrm{P}_2$ long-lived state. Atoms shelved in this dark state are removed from the cooling cycle, significantly reducing the MOT loading efficiency.
In order not to lose these atoms, we use repumping lasers at 707 nm and 679 nm. The 707 nm laser couples $^3\mathrm{P}_2$ to $^3\mathrm{S}_1$, from which atoms decay into all three $^3P_\mathrm{J}$ states, while the 679 nm laser repumps population from $^3\mathrm{P}_0$, ensuring that atoms eventually return to the ground state and reenter the cooling cycle. Fig. 7.5 shows the MOT loading curves under different repumping configurations. Without repumping, the

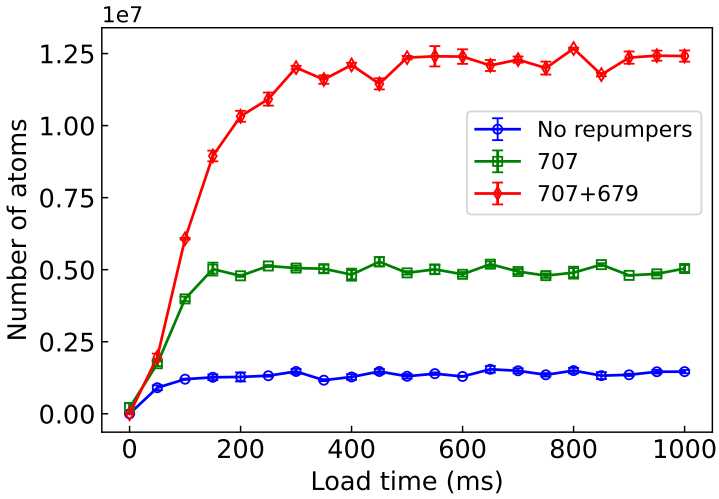

Figure 7.5. Number of atoms in the blue MOT of ^{88}Sr as a function of loading time for different repumping configurations. The blue curve shows the MOT loading without repumpers, while the green curve corresponds to using only the 707 nm repumper. The red curve shows the combined effect of 707 nm and 679 nm repumpers. Error bars indicate the standard deviation from repeated measurements. The 707 nm repumper significantly increases the atom number by recovering atoms trapped in the $^3P_2$ state; however, this also opens the $^3P_0$ state as an additional decay channel from $^3S_1$. The 679 nm repumper closes this channel, and together both repumpers eliminate the major loss pathways, leading to the highest atom number.

MOT saturates below 2×10^6 atoms. Using only the 707 nm repumper partially increase the atom number, while the simultaneous application of both repumpers increases the atom number by nearly an order of magnitude, reaching 1.2×10^7 atoms.

Finally, the MOT temperature was measured by monitoring the free expansion of the atomic cloud at different times of flight. Fig. 7.6 shows the average cloud radius σ_{avg} as a function of TOF. The experimental data (points with error bars) are fitted with the expansion model (solid line), from which we extract a MOT temperature of $T = 6.4\,\text{mK}$, in good agreement with literature results.

Under optimized conditions with repumpers and shielding applied, the trap contains 1.25×10^7 atoms at a temperature of 6.4 mK and a peak density of$3.8 \times 10^9\,\text{cm}^{-3}$. These results establish the performance of the first stage of our cooling sequence and provide the basis for the subsequent stages of cooling and trapping.

7.4 Narrow-line MOT

In order to efficiently load atoms into the optical tweezers, a cold and dense atomic ensemble is required. The blue MOT described above does not provide sufficiently low temperatures or high densities for this purpose. However, the presence of narrow intercombination lines in Strontium, such as the $^1S_0 \rightarrow {}^3P_1$ transition with a natural linewidth of only $\Gamma/2\pi = 7.6\,\text{kHz}$ offers the opportunity to introduce a second cooling stage after the blue MOT. This stage, commonly referred to as the narrow-line red

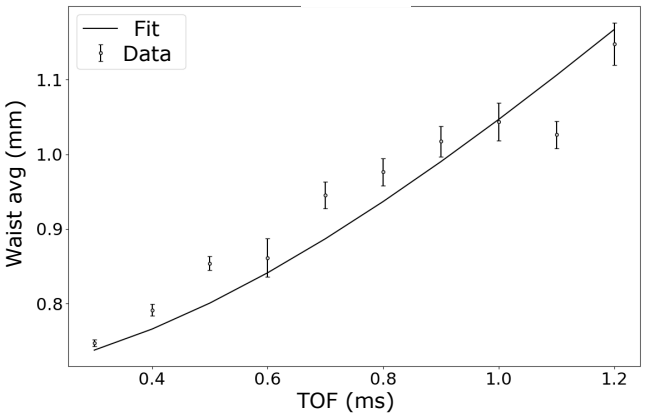

Figure 7.6. Time-of-flight expansion of the blue MOT. The plot shows the measured average width of the atomic cloud as a function of TOF (data points with error bars), together with a fit to the expansion model (solid line). From the fit we extract a temperature of $T = 6.4\,\mathrm{mK}$.

MOT allows further reduction of the atomic temperature and a significant increase in phase-space density.
A direct transfer from the blue MOT, which operates on the broad $^1\mathrm{S}_0 \rightarrow {}^1\mathrm{P}_1$ transition with a linewidth of $\Gamma/2\pi = 32\,\mathrm{MHz}$, into the narrow-line red MOT is not feasible. The linewidth of the $^1\mathrm{S}_0 \rightarrow {}^3\mathrm{P}_1$ transition is more than four thousand times narrower, and consequently the transition has a drastically reduced scattering rate and restoring force. The Doppler capture velocity of the red MOT is on the order of only a few cm/s, far below the typical atomic velocities in the blue MOT, on the order of several m/s. If atoms were released directly from the blue MOT into the red MOT beams, only a negligible fraction would be captured. To overcome this limitation, the red MOT is initially operated with artificially broadened light to extend the velocity capture range. Once the atoms are captured, the spectral broadening is reduced, compressing the MOT and enabling the ensemble to reach µK temperatures and high densities suitable for optical tweezer loading.

7.4.1 Broadband Red MOT

Among the various approaches for extending the capture velocity of narrow-line MOTs, two widely adopted methods are the broadband MOT and the SWAP (Sawtooth-Wave Adiabatic-Passage) MOT. The former relies on creating a multi-frequency laser spectrum to broaden the effective cooling range [116, 117], while the latter employs a frequency-chirped beam that sweeps from red to blue detuning during the cooling cycle [118, 119]. In this work, we implement the broadband (BB) MOT technique by modulating the RF signal driving the AOM used to control the frequency of the red 3D MOT beams. Specifically, a Siglent SDG6022X arbitrary waveform generator (AWG) produces a carrier frequency sinusoidally modulated at 30 kHz with a modulation depth of $\pm 2.4\,\mathrm{MHz}$, yielding a frequency comb approximately 4.8 MHz wide with 30 kHz spacing between spectral components. The AOM operates

in a double-pass configuration, resulting in a 9.6 MHz-wide frequency comb in the laser light.

In our implementation, all frequency components are kept red-detuned, with the upper edge set just below the $^1S_0 \rightarrow {}^3P_1$ resonance and the lower edge extending to larger detunings. The optimal bandwidth is determined empirically: the upper limit strongly affects loading efficiency, whereas the lower limit can be tuned with more flexibility. During loading from the blue MOT to the broadband red MOT, all the frequency components interact with the atoms, while atoms progressively cooled to lower velocities become insensitive to the most red-detuned frequencies. Ideally, one could reduce the comb bandwidth and power per frequency component during the cooling sequence to transition toward a single-frequency (SF) MOT. Nevertheless we achieve efficient loading into the SF MOT by power broadening the NARROW transition linewidth and switch directly from the BB to the SF MOT without modifying the broadband configuration.
Each 3D MOT beam delivers 4 mW of power distributed over 320 frequency components. For a beam waist of 8 mm and a saturation intensity of $I_{\mathrm{sat}} = 3\,\mu\mathrm{W\,cm^{-2}}$, this corresponds to a saturation parameter of $s \approx 4.2$ per tone and a power-broadened linewidth of $\Gamma_s/2\pi = 17\,\mathrm{kHz}$.
Regarding the quadrupole magnetic field, it is necessary to rapidly reduce the gradient from $50\,\mathrm{G\,cm^{-1}}$, required for the blue MOT, to just a few $\mathrm{G\,cm^{-1}}$, as a lower gradient is essential for trapping atoms using the narrow-line red transition. In our setup, the most effective approach is to completely switch off the MOT coils (operated at 100 A for the blue MOT) and then re-enable them at the lower current of 4 A. This method exploits the fast switch-off circuit of the coils described in Sec. 6.2.2, which allows the current to decay in less than 300 µs.

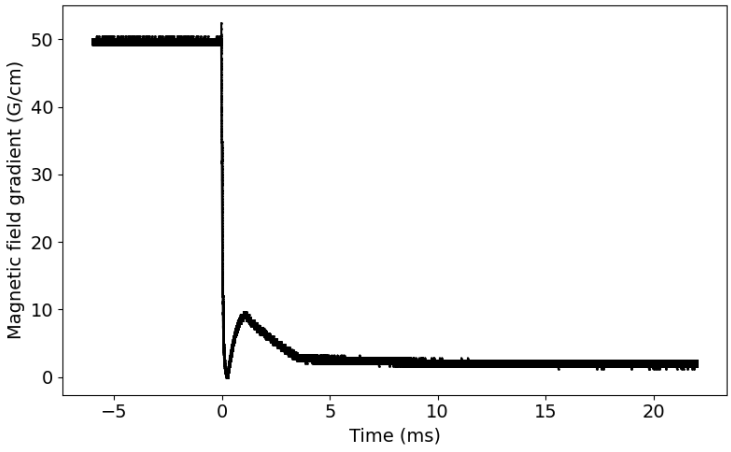

Figure 7.7. Measured magnetic field gradient during the transition from the blue MOT to the red MOT. The gradient is rapidly reduced from $50\,\mathrm{G\,cm^{-1}}$ to $2\,\mathrm{G\,cm^{-1}}$ by switching off the MOT coils and reactivating them at a lower current. The transient overshoot and subsequent damped oscillations are visible in the measurement of the coil current, taken using a current probe (Danisense DS400UB-10V). Despite the overshoot, the atom capture efficiency in the red MOT remains sufficient for our purposes.

To mitigate the overshoot that occurs when the current-controlled power supply is

switched back on, we implement a voltage limit on the power supply during the reactivation phase. This measure suppresses the transient competition between the voltage and current control loops, which otherwise would lead to damped oscillations in the current profile. Fig. 7.7 shows the measured magnetic field gradient during the transient, obtained from a measurement of the coil current with a current probe (Danisense DS400UB-10V). Although the overshoot is reduced by this approach, it is not completely eliminated. Still, the fraction of atoms captured in the red MOT remains sufficient for our purposes. The atoms experience free fall for only a few hundred microseconds before the gradient begins to rise, enabling gradual recapture. As the gradient increases it naturally compresses the atomic cloud since the effective trapping volume decreases with stronger field gradients. A gradient of $2\,\mathrm{G\,cm^{-1}}$ was found to maximize the number of trapped atoms. After achieving the single-frequency (SF) red MOT described in the next section, we optimized the multi-frequency red MOT parameters to maximize the atom number and density in the SF red MOT, rather than tuning each stage independently. The temperature of the red MOT during the broadband stage was measured using a TOF sequence, yielding $\mathrm{T} = 21\,\mu\mathrm{K}$.

7.4.2 Single frequency Red MOT

The final stage of the red MOT cooling sequence is the single-frequency (SF) MOT. While the BB MOT maximizes the capture efficiency by employing a multi-frequency spectrum, the SF MOT aims to achieve the lowest temperatures and highest densities by operating with near-resonant, single-frequency light. In principle, the optimal approach would involve gradually reducing the spectral width of the BB MOT, from a broad frequency comb to a single narrow line, as the atoms are progressively cooled. However, after about 250 ms of BB MOT loading, only a small subset of frequencies remains quasi-resonant with the already-slowed atoms, while the more detuned components no longer interact with the sample. For this reason, we implement a sudden switch from the BB to the SF MOT stage using a single, power-broadened frequency component rather than a gradual spectral narrowing. Experimentally, this approach is also easier to implement, as our AWG does not support fast reconfiguration of the output spectrum. We realize this step by changing the RF source from the Siglent AWG to a fixed frequency RF channel of the Moglabs QRF driver, leveraging a TTL-controlled Minicircuits switch.
Using a single frequency component with a saturation parameter of $s \approx 200$, corresponding to a power-broadened linewidth of:

$$\Gamma_s/2\pi = (\Gamma/2\pi)\sqrt{1+s} \approx 105\mathrm{kHz} \tag{7.6}$$

we achieve a transfer efficiency exceeding 80% from the BB MOT to the SF MOT. This power broadening effectively bridges the transition from the multi-frequency to the single-frequency regime and yields the highest peak density observed in our system.
Fig. 7.8 shows the atom number and peak density in the SF red MOT as a function of the BB MOT loading time. Each experimental cycle consists of a BB MOT stage of variable duration, followed by 50 ms of SF MOT stage, with all measurements taken at the end of the SF stage. As the loading time of the BB MOT increases, both

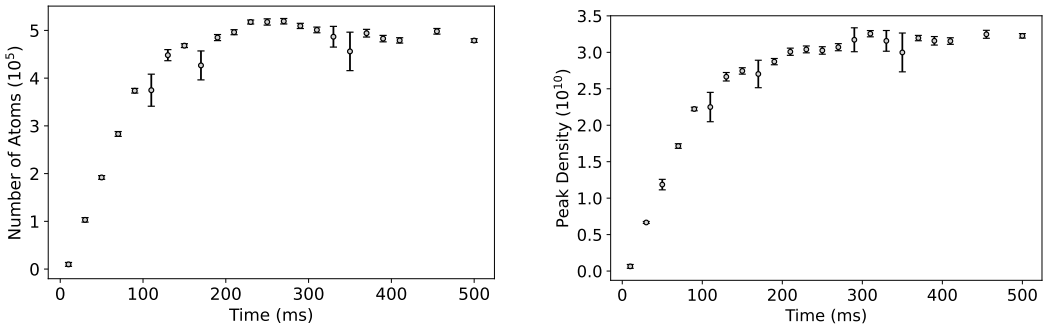

Figure 7.8. Atom number (left) and peak density (right) measured in the single-frequency red MOT as a function of the broadband MOT loading time. The single-frequency stage is fixed to 50 ms and is applied after each BB interval; the x-axis therefore reports only the BB MOT loading time. Both observables increase rapidly with the broadband MOT loading time, approaching an asymptotic value after a characteristic timescale of ~ 250 ms at values of $N \approx 5 \times 10^5$ atoms and $n_{\text{peak}} \approx 2.5 \times 10^{10}\,\text{cm}^{-3}$, beyond which additional cooling time yields no significant gain in atom number or density.

the atom number and peak density in the SF MOT rise and saturate after 200 ms, reaching $N \approx 5 \times 10^5$ atoms and $n_{\text{peak}} \approx 2.5 \times 10^{10}\,\text{cm}^{-3}$. Longer BB loading times do not lead to further improvements, indicating that steady-state conditions are achieved within this timescale.

The atomic density plays a crucial role in ensuring efficient loading of atoms into optical tweezers. Densities on the order of $10^{10}\,\text{cm}^{-3}$ are required to achieve high loading probabilities. Such densities are achieved only in the SF red MOT, whereas both the blue MOT and the BB red MOT operate at significantly lower densities, insufficient for efficient tweezer loading.

The temperature of the atomic cloud was determined through TOF measurements. Fig. 7.9 shows the measured average cloud radius as a function of the expansion time. Fitting the data with the expansion model described in Sec. 7.2 we obtain a temperature of 5.38 µK. For comparison, the Doppler cooling limit for the $|^1S_0\rangle \rightarrow |^3P_1\rangle$ power broadened ($s \approx 200$ and $\Gamma_s/2\pi \approx 100$ kHz) transition is $T_D = \frac{\hbar\Gamma_s}{2k_B} = 2.5$ µK, indicating that the achieved MOT temperature is approximately twice the theoretical limit. This temperature, while higher than the sub-microkelvin records achieved in pioneering narrow-line cooling experiments [117, 57], results from operating the red MOT at a high saturation parameter to maximize transfer efficiency and peak density. This operating regime, characteristic of modern Strontium tweezer platforms [34, 120, 49], deliberately trades lower temperatures for an increased capture volume and is consistent with typical ^{88}Sr parameters used as a starting point for loading deep micro-traps in quantum simulation experiments.

Fig. 7.10 shows the evolution of the atomic cloud throughout the three cooling stages: initial capture in the broad-line blue MOT, transfer to the BB red MOT, and final compression in the SF red MOT. Over this sequence, the atomic distribution evolves from a large, dilute ensemble to a much smaller and denser cloud, suitable for optical tweezer loading.

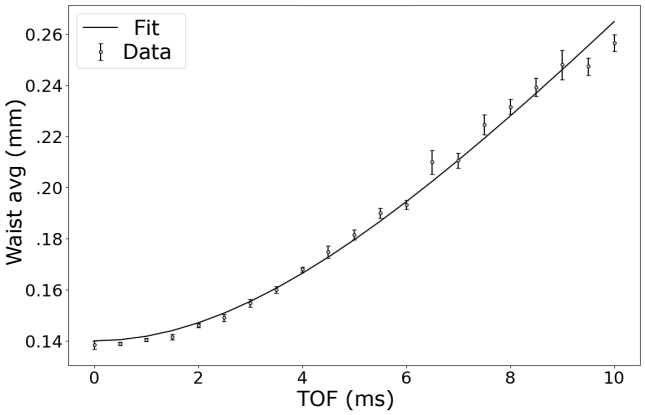

Figure 7.9. Time-of-flight measurement for ^{88}Sr atoms in the single-frequency MOT. The average cloud waist is shown as a function of time of flight (dot with error bars), together with the fit (black line) used to extract the temperature. From the fit we obtain a temperature of 5.38 µK.

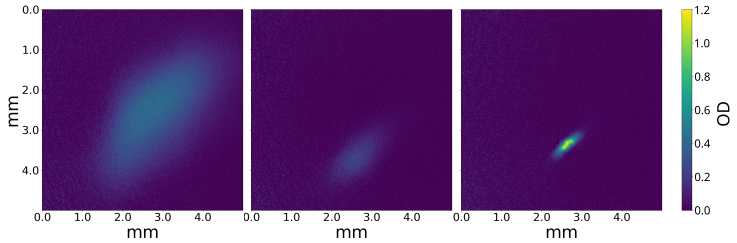

Figure 7.10. Absorption images of the Strontium MOT at different operating stages. From left to right: broad-line shielded blue MOT, broadband red MOT stage, and narrow-line red MOT. The reduction of the cloud size and the increase in density are clearly visible as the cooling sequence progresses. The MOT center coordinates differ between the blue and red MOT stages due to a slight spurious offset introduced by the different gradient that we didn't fully compensate with the compensation coils.

Chapter 8

Single atoms in optical tweezers

This chapter is partially based on the publication under review: **V. Giardini**, L. Guariento, A. Fantini, S. Storm, M. Inguscio, J. Catani, G. Cappellini, V. Gavryusev, and L. Fallani, *"Single Strontium Atoms in Optical Tweezer Arrays for Quantum Simulation," arXiv*:2510.19816 [physics.atom-ph] (2025), `https://doi.org/10.48550/arXiv.2510.19816`.

In the previous chapter we have explored the principles and practical implementation of magneto-optical trapping for preparing cold atomic ensembles. While a MOT can deliver large numbers of ultracold atoms with modest phase-space density, it remains a "collective" confinement method, the atoms are loosely bound in a cloud and interact with each other and the cooling light.
The next step is to isolate individual atoms in optical tweezers. In these traps, a single atom can be held, manipulated, cooled, and measured with high precision. This capability lies at the heart of many forefront applications: programmable quantum simulators, neutral-atom quantum computers, ultra-precise metrology, and studies of fundamental quantum dynamics.
However, guiding an atom from the MOT into an optical tweezer is nontrivial. One must carefully engineer the spatial and temporal overlap between MOT and tweezer, optimize cooling and capture parameters, and control heating and collisional losses. After being transferred into the optical tweezer the atom must be further cooled and detected while maintaining high survival probability and measurement fidelity.
This chapter describes the complete procedure for single-atom trapping in optical tweezers. We begin with the dynamics of loading from the MOT, proceed to describe the nature of the optical trap, then analyze collisional and cooling mechanisms that ensure single occupancy. We detail the imaging strategies used to detect single atoms and how the system is characterized via detection fidelity, survival probability and temperature measurements.

8.1 Tweezer generation

The optical setup used to generate the tweezer array is the one described in Sec. 4.3. In the current implementation, only the part involving the two crossed AODs has been realized and is actively employed, while the SLM module is still being tested. The crossed AODs allow to create static rectangular arrays. Although this

configuration does not provide the flexibility offered by an SLM, it nevertheless allows the generation of stable optical tweezers and the trapping of atoms. All the work presented in this chapter involving optical tweezers was carried out using a 3×3 array as shown in Fig. 8.1. Each tweezer has a waist of approximately 1.5 µm, with a center-to-center separation of 10 µm. Such waist is larger than the expected diffraction limited size (0.9 µm), most likely due to slightly underfilling the objective's back focal plane and to optical aberrations introduced by the optics we used and that we have already planned to overcome in a planned upgrade of the optical setup. Larger arrays with smaller spacings could in principle be produced, but the current configuration is enough for the initial characterization of the system and for single-atom trapping. Furthermore, such small array was chosen not due to technical limitations (such as limited FOV or laser power budget), but for ease of equalizing the trap depths among fewer tweezers. In future experiments we can easily reach 10×10 configurations and beyond.
To verify the correct projection of the optical tweezers, a second "service" objective, identical to the main one, is mounted on the opposite side of the glass cell. This objective forms an imaging system coupled to a Basler Ace acA4024-29um camera, allowing direct imaging of the tweezer array (which is shown in Fig. 8.1) and the evaluation of optical aberrations. Fine adjustments of the tweezer injection through the objective are used to minimize distortions. Careful parallel and coaxial alignment of the two objectives is essential, as any misalignment of the service imaging system could itself introduce mayor aberrations impacting the detected tweezer shape.

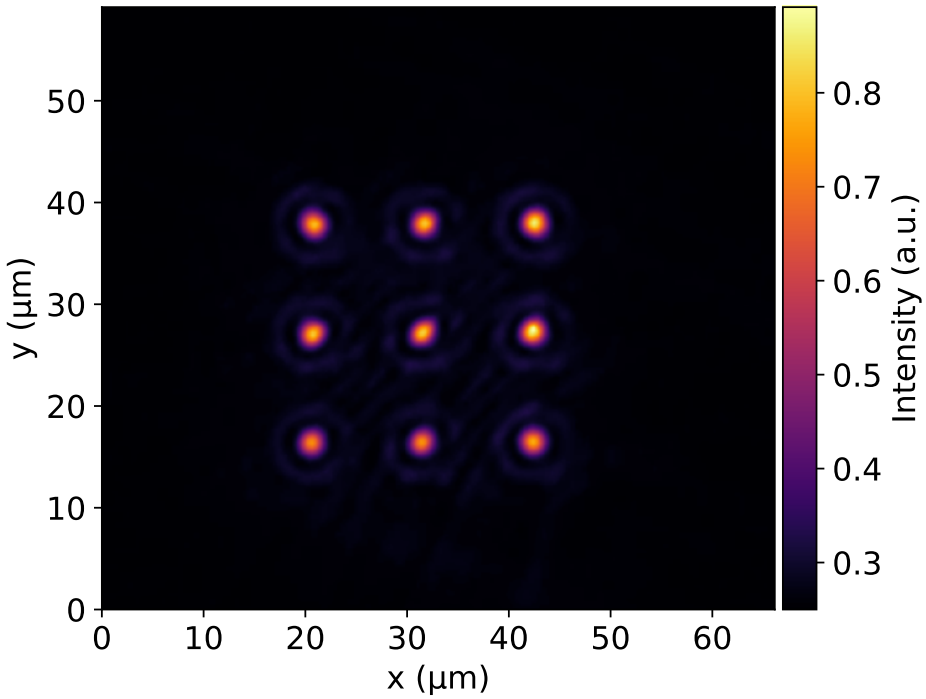

Figure 8.1. Image of the optical tweezer array recorded with the service imaging system. The array consists of 3×3 traps generated with crossed AODs. Each tweezer has a waist of ~ 1.5 µm and a center-to-center separation of 10 µm.

Loading atoms into optical tweezers requires precise spatial overlap between the tweezer array and the red MOT. Achieving this alignment is challenging, as the field of view of the high-NA objective is only a few hundred micrometers, comparable to the MOT size itself ($\approx 400\,\mu m$). To facilitate the alignment, we employed a 2 mm waist reference blue beam that intersects the red MOT orthogonally to the cell. This beam served as a guide for positioning the microscope objective on its translation stage (manual x, y + motorized z). The objective axial position was then fine-tuned by recording fluorescence images of the red MOT collected through the objective itself. Thanks to the axial translation stage's repeatability of 200 nm, the MOT can be scanned across different focal planes with sub-micrometer precision.
The overlap between the MOT and the tweezer array was achieved and optimized by displacing the MOT itself employing bias magnetic fields along the three Cartesian axes. These fields are applied via the compensation coils described in Sec. 6.2.3 with a sensitivity on the displacement of the MOT of $2\,\mu m/mG\,cm^{-1}$. This approach is more robust than moving the position of the tweezer array, since the optical traps are extremely sensitive to alignment and optical aberrations. The relative positioning of the MOT and the tweezer array is continuously monitored through the service imaging system, which simultaneously records the MOT fluorescence and the tweezer pattern.
Using this procedure, we achieved a good spatial overlap between the MOT and the tweezer array, allowing the detection of an initial fluorescence signal from atoms loaded into the optical traps. Subsequent fine-tuning of both alignment and experimental parameters was performed by directly maximizing the fluorescence signal of the trapped atoms.

8.2 Single-atom imaging

Precise, site-resolved imaging of single atoms is a key capability in modern quantum simulation platforms based on optical tweezer arrays. In our experiment, we employ fluorescence imaging to detect individual atoms, a technique that has become a standard tool [121, 122, 123, 124].
The main objective of the imaging sequence is twofold: to accurately determine whether an atom is present at a given site, and to do so in a non-destructive manner, allowing the atom to remain trapped and available for subsequent operations. The first goal is characterized by the detection fidelity, which quantifies how reliably an atom can be distinguished from background fluorescence. The second is described by the survival probability, representing the likelihood for the atom to remain trapped after the imaging sequence. Both benchmark parameters are closely related to the photon scattering process, which must produce enough photons to be clearly distinguished from the background signal in the imaging system. Two main mechanisms can prevent this from happening: heating induced by fluorescence scattering, which can lead to escape from the trap, and optical pumping into long-lived dark states, which take the atoms out of the imaging cycle. Therefore, in addition to addressing the atom with an imaging beam, we need to provide a mechanism for cooling as well as one for ensuring that no unwanted states are populated.
High-fidelity detection and survival of individual atoms are essential for the real-

ization of large-scale, defect-free arrays and for enabling controlled interactions to study many-body phenomena on such a platform.

8.2.1 Imaging scheme

So far, two distinct imaging schemes have been implemented for Sr atoms. The first is based on the strong dipole-allowed ${}^1S_0 \rightarrow {}^1P_1$ transition at 461 nm [120, 53, 54] while the second exploits the narrow intercombination line ${}^1S_0 \rightarrow {}^3P_1$ at 689 nm[62]. Both transitions enable single-atom imaging, but with fundamentally different trade-offs in terms of scattering rate, atom heating and experimental complexity. In our current implementation, we use the 461 nm scheme, but the red transition offers an interesting alternative pathway that may be explored in the future.

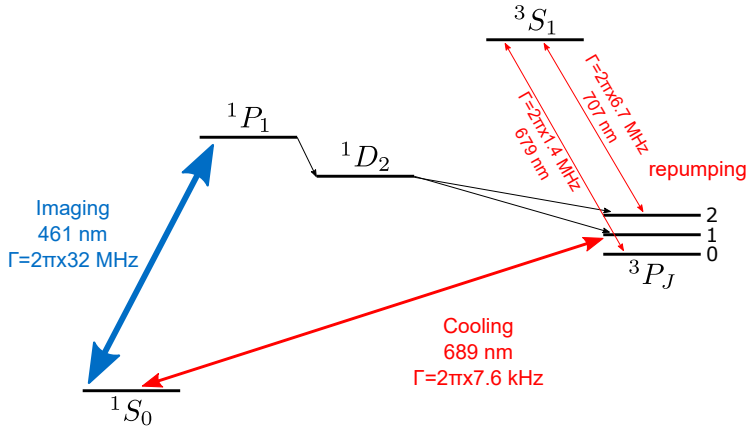

Figure 8.2. Relevant energy levels and optical transitions used for single-atom fluorescence imaging. We use the broad ${}^1S_0 \rightarrow {}^1P_1$ transition at 461 nm to scatter fluorescence photons. Due to the weak decay channel from ${}^1P_1$ to ${}^1D_2$ and then to the metastable ${}^3P_J$ states, two repumping lasers at 679 nm and 707 nm are used to maintain a closed optical cycle. A red cooling beam at 689 nm ensures atom retention by compensating for heating induced by blue scattering.

The blue imaging scheme is represented in Fig. 8.2. The 461 nm transition has a large natural linewidth ($\Gamma/2\pi \sim 32$ MHz), allowing for bright and fast imaging. However, it is not a perfectly closed transition, since the excited ${}^1P_1$ state has a small branching ratio to ${}^1D_2$, which subsequently decays into metastable ${}^3P_J$ states. As for the cooling process, atoms shelved in these long-lived states no longer scatter photons and are effectively lost from the detection cycle. To mitigate this, we employ the same repumper that we use for the blue MOT to repump population from ${}^3P_2$ and ${}^3P_0$, ensuring that atoms eventually return to the ground state and re-enter the imaging cycle. Concurrently, to counteract the heating induced by blue photon recoil during imaging, simultaneous cooling is implemented using the 689 nm red transition, realizing the Sisyphus cooling scheme (see Sec. 2.7.2), that requires careful tuning of detuning and intensity to ensure that the atoms remain trapped. While the maximum scattering rate is $R_{sc} = \frac{\Gamma}{2}$, it is convenient to work in a lower scattering rate regime for the imaging beam to allow the cooling beam to compensate for the heating induced by blue photon scattering, which could cause atom loss and therefore a lower detection fidelity. Since red cooling temporarily populates the ${}^3P_1$

state, the time during which blue photons are scattered is limited. To address this, the imaging sequence employs short pulses of blue light in the presence of continuous red cooling light, allowing fluorescence photons to be accumulated over multiple cycles, while minimizing heating and thus preserving the atom.
Additional considerations arise from light shifts induced by the trapping potential. In a tweezer at 813.4 nm, the excited $^1P_1$ state is more strongly confined than the ground state $^1S_0$, leading to a red shift of the resonance of about -12 MHz at 360 µK trap depth. This shift must be compensated by detuning the imaging light accordingly, and can even be exploited by detuning the imaging beam so that its resonance coincides with the trap center, the scattering rate naturally decreases toward the edges of the trap, helping to keep the atom confined and enhancing survival.
While the blue scheme offers simplicity and high scattering rates, the alternative red imaging scheme presents a compelling route to fully non-destructive detection [62]. In this approach, a single laser on the narrow $^1S_0 \rightarrow {}^3P_1$ line is used for both cooling and photon collection. Because of the narrow linewidth ($\Gamma/2\pi = 7.6$ kHz), the atom can remain in the motional ground state throughout the imaging process, and heating is negligible. Moreover, repumpers are not required, as the only pathway to metastable dark states is through off-resonant scattering of tweezer light, which is suppressed at shallow trap depths. However, this scheme demands a fine balance between detuning and intensity, since optimal imaging conditions (high intensity, low detuning) are incompatible with efficient cooling (low intensity, large detuning). One can alternate between imaging and cooling with millisecond duty cycles to optimize both. Additionally, the longer wavelength limits spatial resolution and the imaging time needs to be longer because of the reduced scattering rate.

8.2.2 Photon collection

To detect single atoms in tweezers we collect the fluorescence photons emitted by the atoms when illuminated by a resonant imaging beam that is orthogonal to the objective. Each photon plays a fundamental role in distinguishing the atomic signal from the background, so having a high collection efficiency is very important.
The optical setup used for fluorescence imaging is represented schematically in Fig. 8.3. A resonant blue beam at 461 nm, along the z axis, excites the trapped atoms and induces fluorescence, while a red beam at 689 nm provides Sisyphus cooling. The emitted photons are collected by the same high–numerical-aperture objective employed to generate the tweezers, as described in Sec. 4.1.1. A dichroic mirror separates the tweezer light from the atomic fluorescence, which is subsequently directed onto a camera for detection.
The polarization of the imaging beam plays a crucial role, as it defines the atomic dipole radiation pattern, which describes the probability distribution for photon emission on the unit sphere. For a classical oscillating dipole, the emission is anisotropic, with maximum intensity in the plane orthogonal to the direction of the dipole oscillation. The radiation pattern for a transition from an excited state with total angular momentum J_e to a ground state with J_g can be derived following Ref. [45]. In this formalism, the dipole operator is decomposed into spherical components d_q, with $q = 0, \pm 1$, corresponding to π ($q = 0$) and σ_+/σ_- ($q = \pm 1$) polarizations.

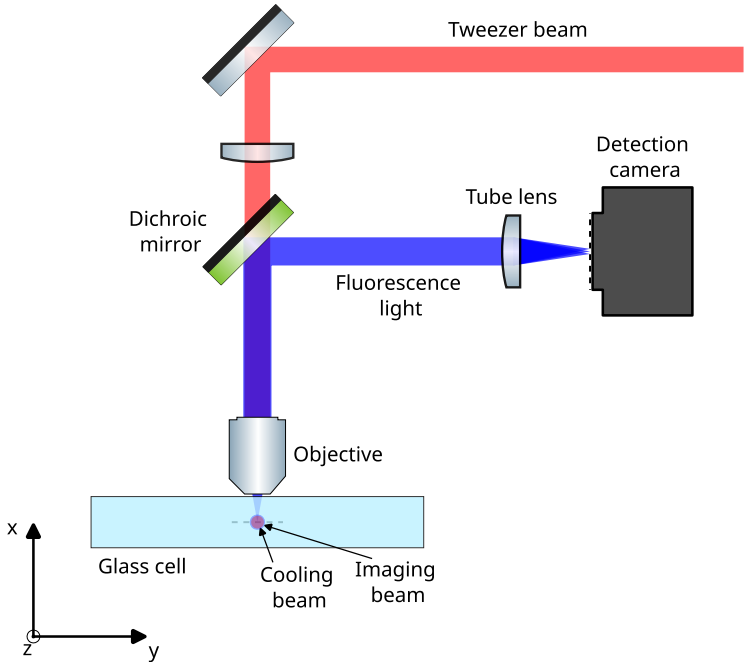

Figure 8.3. Optical setup for the detection of atoms in optical tweezers. The tweezer beam (red) is focused into the glass cell by a high–numerical-aperture objective. A resonant imaging beam along z (blue) excites the atoms, while a red cooling beam along the same direction provide Sisyphus cooling. The fluorescence light is collected by the same objective used for tweezer generation, separated from the tweezer beam with a dichroic mirror, and directed into a detection camera.

The radiation intensity involves sums over terms $\left\langle d_q d_{q'}^\dagger \right\rangle$, where q labels the emitting component of the dipole and q' the component that interferes or contributes to the intensity.In our case, the relevant transition involves $J_g = 0$ and $J_e = 1$, where only the $q = q' = -m_e$ terms contribute. The radiation pattern then simplifies to [48]:

$$D(\theta, \phi) = \frac{3}{8\pi} \sin^2(\theta) \qquad \text{for } \pi \text{ polarized light} \tag{8.1}$$

$$D(\theta, \phi) = \frac{3}{16\pi} \left(1 + \cos^2(\theta)\right) \qquad \text{for } \sigma_\pm \text{ polarized light} \tag{8.2}$$

where θ is the angle with respect to the quantization axis $\hat{z}$ and ϕ is the azimuthal angle. To maximize photon collection, the imaging polarization is chosen to align the emission pattern with the objective. For π-polarized light, emission is maximized at $\theta = 90°$, whereas for σ-polarized light the maximum occurs at $\theta = 0°$. In our implementation, the objective axis is defined as $\hat{x}$, the orthogonal horizontal axis as $\hat{y}$, and the vertical axis as $\hat{z}$. The imaging beam propagates along $\hat{z}$ and is linearly polarized along $\hat{y}$, which enhances fluorescence collection along the objective axis $\hat{x}$. The overall collection efficiency C can be expressed in terms of the numerical aperture of the objective:

$$C = \frac{1}{8} \left(4 + (NA^2 - 4)\sqrt{1} - NA^2\right) \tag{8.3}$$

For our objective with $NA = 0.56$ at 461 nm, this expression yields a maximum collection efficiency of $C = 0.118$. This value accounts only for the geometric solid angle of the objective. In future iterations of the experiment, we plan to use the service objective on the opposite side of the cell to collect florescence as well, effectively doubling the collected solid angle and thereby enhancing the fluorescence signal.
Maximizing the fluorescence signal from single atoms requires careful optimization of every element in the imaging setup. A crucial component is the detection camera, since the ability to resolve the signal of only a few scattered photons depends critically on low readout noise and high quantum efficiency. Two main technologies are commonly employed in single-atom experiments: electron-multiplying charge-coupled devices (EMCCDs) [125, 126, 127] and quantitative complementary metal-oxide-semiconductor cameras (qCMOS) [128, 39, 129]. Although based on different architectures, both rely on a pixelated sensor to reconstruct an image of the atomic array.
In our implementation, we employ a scientific qCMOS camera (Hamamatsu ORCA-Quest C15550-20UP). This device combines high quantum efficiency ($\sim 85\%$ at 461 nm and $> 55\%$ at 689 nm) with extremely low readout noise (< 0.3 electrons RMS per pixel), enabling photon-counting performance without the excess noise associated with EMCCD multiplication gain. Unlike CCDs, which rely on a single output amplifier, CMOS sensors read out pixels in parallel. This architecture reduces readout time, allows for large sensor formats (up to 4096×2304 pixels of $4.6\,\mu$m size in our case), and provides the flexibility to balance speed and sensitivity across different imaging scenarios. The low readout noise makes it possible to resolve photon-number peaks in the detection histogram with $< 5\%$ probability of misclassification, a key feature for quantitative atom detection in the presence of nonzero background.
The optical design ensures that atomic fluorescence is efficiently relayed onto the camera sensor. Since atoms in optical tweezers can be approximated as point-like emitters (their wavefunction spread in the trap being well below the optical resolution) the achievable image resolution is set by the imaging point spread function (PSF). To form a conjugate image on the camera plane, the fluorescence collected by the microscope objective is reimaged using a tube lens placed at its focal distance from the sensor (see Fig. 8.3). Additional relay telescopes can be introduced to adjust magnification between planes. In our setup, a tube lens with $f_{\text{fluo,tl}} = 100\,\text{mm}$ is aligned with the objective's optical axis, yielding a total magnification $M = \frac{f_{\text{fluo,tl}}}{f_{\text{EFL}}} \simeq 4.2$, where $f_{\text{EFL}} = 24\,\text{mm}$ is the effective focal length of the objective. With this configuration, the image of a single atom is projected onto approximately one camera pixel, maximizing signal concentration and facilitating atom identification.
The PSF observed in practice results from the convolution of the diffraction-limited PSF with any residual aberrations in the imaging path. These aberrations must therefore be minimized by employing aberration-corrected optics and careful alignment. In the conservative limit, the uncertainty in the atomic position within the image is taken to be the tweezer waist itself, magnified by the detection optics. This sets the relevant scale for distinguishing neighboring atoms according to the Rayleigh criterion.

Special attention must also be paid to background suppression. The fluorescence detection path is separated from the tweezer light by a dichroic mirror placed where the beam is collimated to avoid aberration. Despite this, intense reflections of the trapping light from the glass cell surfaces and the dichroic itself can leak through even high-quality dichroics. To reject this unwanted background, three additional bandpass filters are inserted in the imaging path, ensuring that only fluorescence photons can reach the detector.
Overall, the combination of a high-performance qCMOS sensor, diffraction-limited optics, and aggressive filtering yields an imaging system capable of resolving single atoms with high fidelity, as discussed in the following, while maintaining flexibility for future extensions to non-destructive red imaging.

8.3 From multiple to single atoms

Once a first fluorescence signal from atoms confined in the tweezers was obtained, the experimental parameters were further optimized to enhance the detected fluorescence. An example is shown in Fig. 8.4, where multiple tweezers are simultaneously loaded. In this particular realization, a 3×3 array of tweezers is employed, each with a trap depth of approximately $360\,\mu$K.

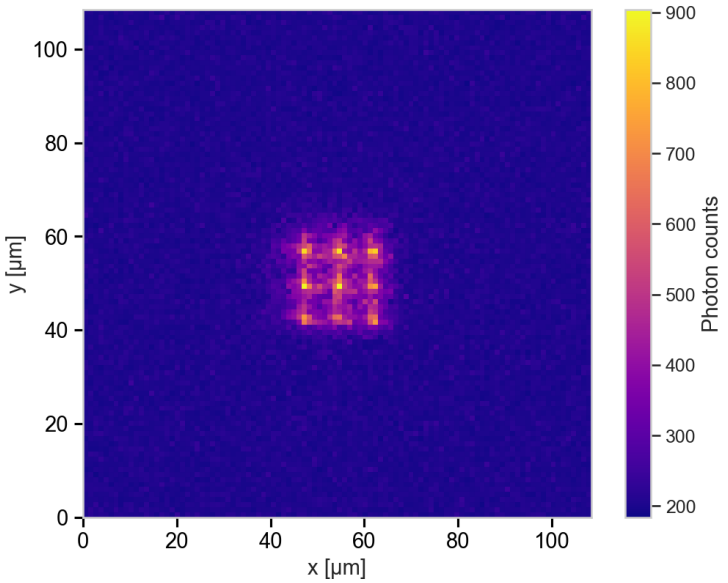

Figure 8.4. Fluorescence image demonstrating the simultaneous loading and detection of multiple atoms in a 3×3 array of optical tweezers, with a trap depth of approximately $360\,\mu$K per tweezer. The signal shows distinct trapping sites, with the color map indicating the detected Photon counts (intensity). The axes represent the spatial extent of the imaging region in micrometers.

In order to maximize the fluorescence signal, it is essential to reduce atom loss during the imaging stage. To this end, cooling is applied to the trapped ensemble, ensuring that the atoms remain confined while scattering photons. The fluorescence yield thus serves not only as an indicator of the atom number but also as a sensitive probe

of the efficiency of the cooling stage.
In addition to the measurements averaged over the 9 tweezers, individual tweezer signals were analyzed. This allowed for fine-tuning of the trap depths across the array. Specifically, by adjusting the amplitudes of the RF tone that generate the individual traps by AOD diffraction, the depths could be equalized to minimize inhomogeneities among the tweezers. Such balancing is crucial: small differences in trap depth can lead to different Stark shifts for the 461 nm and the 689 nm transition resulting in variations in loading probability, cooling efficiency, and fluorescence across the array. By carefully optimizing these parameters, a more uniform array of traps is achieved.
As for fluorescence imaging, we employed a sequence of pulsed blue light with a total duration of 250 ms, consisting of 1 ms pulses repeated at a frequency of 1 kHz. During the imaging sequence, the Sisyphus cooling beam was kept on, ensuring that atoms remained confined in the tweezers while scattering photons.

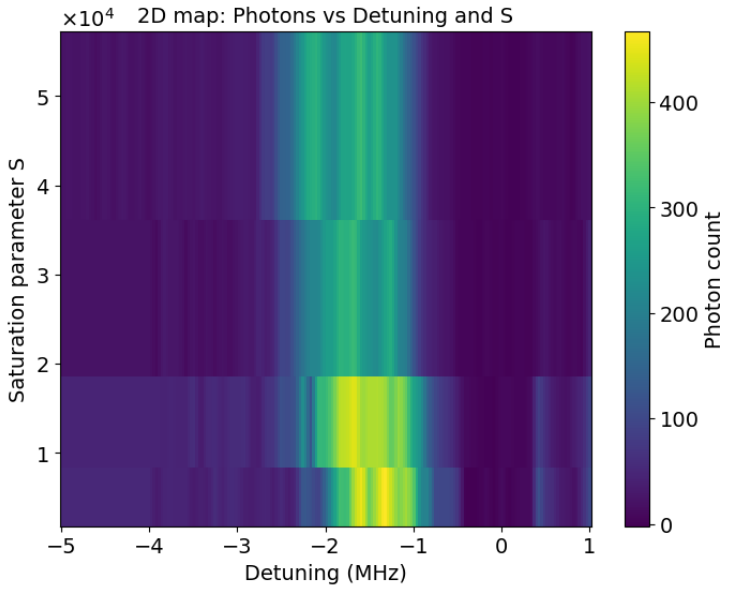

Figure 8.5. Two-dimensional map of fluorescence yield during Sisyphus cooling optimization. The Photon count (color scale) is plotted as a function of both the cooling beam Detuning (x-axis) and the Saturation parameter S (y-axis). The distinct bright region highlights the optimal operational window where maximum fluorescence is achieved, providing a clear map for simultaneously setting the ideal cooling frequency and intensity.

To identify the optimal cooling parameters, systematic scans of the Sisyphus cooling beam frequency and power were performed. The polarization of the Sisyphus beam was also empirically optimized to maximize the resulting signal. The results of these scans, shown in Fig. 8.5, represent averages over the 9 tweezers in the array and provide a clear picture of the parameter regions where the fluorescence is maximized. Based on the optimization scans, we operated the Sisyphus cooling beam at a detuning of -1.4 MHz relative to resonance and at a saturation parameter of approximately 5×10^3. The intensity of the imaging beam was also optimized in order to maximize the detected fluorescence signal, as shown in Fig. 8.6. The

fluorescence signal is observed to increase sharply at low imaging powers and then to saturate, with an optimal working point at $s = 0.1$. Operating in this regime provides a good compromise between achieving high photon counts and avoiding excessive perturbation of the trapped atoms.
It should be emphasized that fluorescence images obtained under these conditions

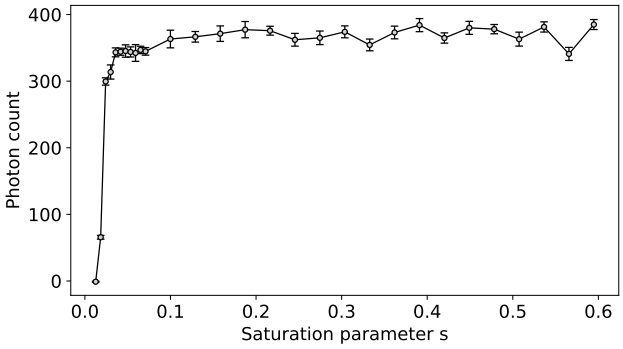

Figure 8.6. Fluorescence counts from multiple atoms in tweezers as a function of the imaging beam saturation parameter s. The signal rises steeply at low power and then reaches a plateau, indicating the onset of saturation. The optimal working point was chosen around $s = 0.1$, balancing photon collection efficiency with minimal heating and atom loss.

do not allow us to obtain the number of atoms trapped in each tweezer. The strong fluorescence signal indicates multiple-atom occupancy, but the detection does not provide the single-atom sensitivity required to distinguish between different atom numbers. These measurements therefore serve primarily as a diagnostic for optimizing trap loading and imaging conditions.

8.3.1 Single atoms

In order to reach the single-atom regime a light-assisted collisions (LAC) stage is introduced in the sequence. This procedure, described in Sec. 4.5, removes multiple occupancies and ensures that each tweezer is either empty or contains a single atom [86]. This additional step is implemented immediately after the initial loading, with parameters similar to those used for fluorescence imaging [34]. We scanned the Sisyphus beam frequency and power, the imaging beam power, and the LAC duration, to identify the operating conditions that yield a clear bimodal separation in the fluorescence count distribution (attributable to 0 or 1 atom) and simultaneously maximize the atom survival probability. Under these optimized conditions, we typically achieve a filling fraction of about 50%, consistent with the probabilistic nature of single-atom loading.
After this stage, the system enters the single-atom regime. Due to the nature of the collisions that lead to individual trapped atoms, not all sites are simultaneously occupied in a single shot as shown in Fig. 8.7. To visualize the array more clearly, we average over 1000 realizations, as shown in Fig. 8.8(a). A complementary view is provided by the fluorescence count histogram in Fig. 8.8(b), constructed

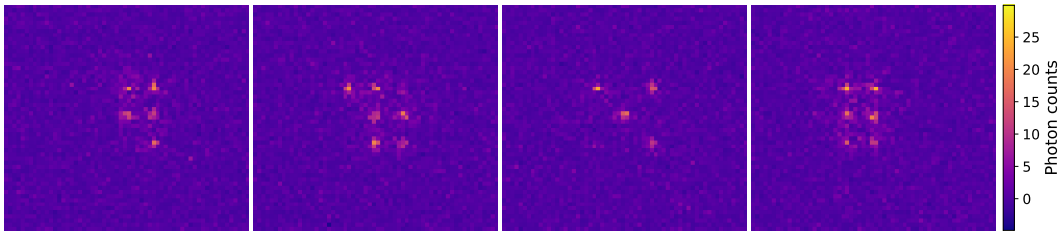

Figure 8.7. Fluorescence images of the 3×3 tweezer array in the single-atom regime taken in consecutive experimental realizations. Due to the LAC process not all the sites are occupied.

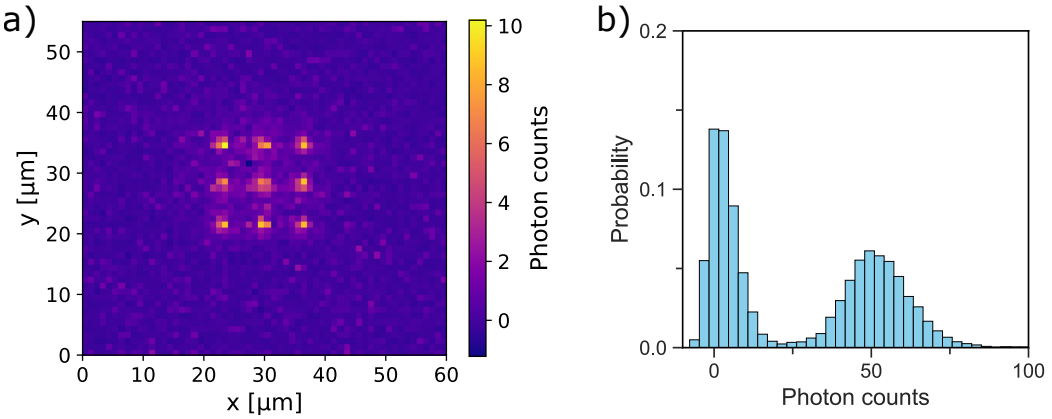

Figure 8.8. (a) Fluorescence image of a 3×3 tweezer array in the single-atom regime, obtained by averaging over 1000 experimental realizations after the LAC process. (b) Histogram of fluorescence counts from the same dataset, showing a bimodal distribution with two clearly separated peaks corresponding to empty and individually occupied tweezers. The absence of additional peaks confirms the suppression of multiple-atom occupancies.

from the same set of 1000 measurements analyzed as described in Sec. 8.4. The histogram exhibits a well-defined bimodal distribution with two clearly separated peaks corresponding to empty (0 atoms) and occupied (1 atom) tweezers. The absence of intermediate or higher-count peaks demonstrates that multiple-atom occupancies are effectively suppressed by the LAC process.

With these optimized conditions, the LAC procedure reliably prepares arrays of single atoms, enabling subsequent experiments that require deterministic single-particle control. The optimal parameter in for the LAC are $s = 0.15$ for the 461 nm beam and $s = 2 \times 10^4$ and a red detuning of 2 MHz from the free space resonance of the red transition for the 689 nm beam.

It is worth noting that the optimal Sisyphus cooling parameters and imaging power for imaging single atoms differ from those used in the many-atom regime. In particular, after adjusting the parameters in order to balance photon collection efficiency with minimal heating and ensuring high-fidelity single-atom detection, we found out that the optimal parameter for imaging single atoms in our experimental sequence are $s = 0.03$ for the 461 nm beam and $s = 1.3 \times 10^4$ and a red detuning of 2.1 MHz from the free space resonance of the red transition for the 689 nm beam.

The full experimental sequence used to prepare single atoms is summarized in Fig. 8.9. The protocol begins with a blue shielded MOT stage, which provides initial cooling and compression of the atomic cloud. This is followed by a multifrequency red MOT phase, further reducing the atomic temperature while maintaining a sufficiently large number of atoms. A subsequent single-frequency red MOT stage enables efficient transfer of atoms into the optical tweezers array, with a trap depth of 360 µK. We note that the duration of the blue MOT and red BB MOT stages are lower than the optimal values found while characterizing the MOT themselves, indeed, when we tried to optimize the sequence in order to keep it as short as possible to accumulate statistics, we found out that those timings where still good enough for the purpose of loading efficiently the atoms in the optical traps.
Immediately after loading, a light-assisted collisions (LAC) stage of about 30 ms is applied to remove pairs of atoms and thereby prepare the array in the single-atom regime. This is followed by the fluorescence imaging phase, consisting of pulsed blue light together with continuous Sisyphus cooling. Although the LAC and imaging stages appear similar in structure, their parameters (beam powers, detunings, and durations) are carefully optimized for their respective purposes: the LAC step maximizes single-atom preparation fidelity, while the imaging step ensures efficient photon collection without compromising atom survival.

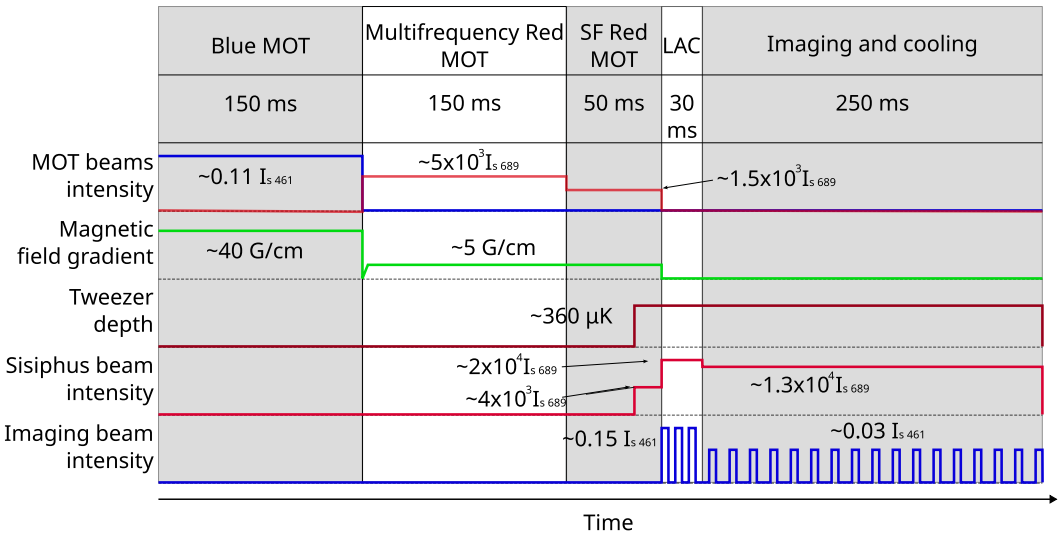

Figure 8.9. Experimental sequence for atom loading, preparation, and imaging. The timeline (horizontal axis) shows the successive stages: blue MOT, multifrequency red MOT, single-frequency red MOT, LAC, and imaging. The evolution of the key parameters is plotted as a function of time: MOT beam intensity, magnetic field gradient, tweezer depth, Sisyphus beam intensity, and imaging beam intensity. During the final imaging stage, 1 ms blue-light pulses at 1 kHz are applied for 250 ms, together with continuous Sisyphus cooling. This sequence ensures efficient loading into the tweezers, elimination of multiple occupancies, and high-fidelity single-atom fluorescence detection.

8.4 Signal analysis

The fluorescence signal, collected by the camera as described in Sec. 8.2.2, is analyzed to determine whether an atom is present in a given optical tweezer. IN the regime discussed in Sec. 8.3.1, the outcome of this analysis is inherently binary: an atom is either detected or not. To reliably discriminate the atomic signal from the background, a sufficient number of photons must be collected during the exposure. The first step in this procedure is to accurately identify the atomic positions within the acquired fluorescence images. For this purpose, a large dataset of single-shot images is acquired and averaged in order to obtain a clean reference image of the tweezer array (as the one shown in Fig. 8.8). The resulting averaged image exhibits well-defined point-spread functions (PSFs) corresponding to each trap position. To extract the precise spatial coordinates of the atoms, each PSF in this averaged image is fitted with a two-dimensional Gaussian function. This fitting procedure provides a robust estimate of the centroid position of the fluorescence distribution, accounting for the finite spatial spread of the atomic PSF across neighboring pixels.
For each identified centroid, a region of interest (ROI) is then defined. Given the magnification of our imaging system, the expected PSF width is on the order of a single pixel. We select ROIs of 3×3 pixels centered on each atom (Fig. 8.10).

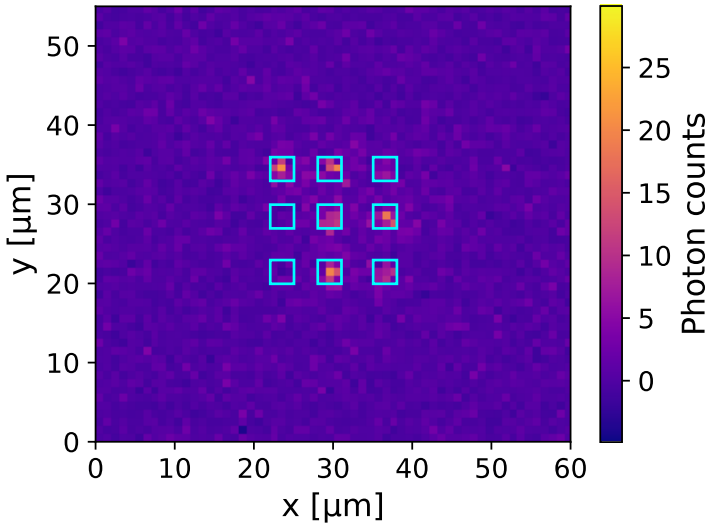

Figure 8.10. Example fluorescence image showing the selected ROIs of 3×3 pixels centered on the atomic array sites. The ROIs are used to extract the photon counts corresponding to each individual atom from a single experimental acquisition.

The choice of ROI size is crucial: a too small region would underestimate the total signal, while an excessively large region would introduce unnecessary background noise. Moreover, when atoms are closely spaced, large ROIs may include contributions from neighboring tweezers. For the data presented in this work, the atomic separation is sufficiently large to prevent any PSF overlap, making the ROI selection straightforward. In regimes where adjacent PSFs are not fully resolved, principal component analysis and several deconvolution methods has been demonstrated to serve as an effective disambiguation technique [130].

The background contribution is estimated by sampling regions of the image that contain no tweezers, and the mean background level is subtracted from the entire image to isolate the atomic fluorescence signal. The raw camera output, expressed in Analog-to-Digital Units (ADU), is then converted into the corresponding number of electrons using the system gain factor (0.11 electrons per ADU in our setup). Because not all incident photons generate an electron, this signal is further corrected by the quantum efficiency (QE) of the sensor. In our case, the QE is 0.85, meaning that 85% of incoming photons successfully produce a detectable electron. Summing the calibrated signal over each ROI yields the photon count associated with the respective tweezer.
Finally, the presence or absence of an atom can be determined by comparing the photon count to a predefined discrimination threshold. Signals below this threshold correspond to empty tweezers, while those above it indicate the presence of an atom. Although the threshold value can in principle be chosen arbitrarily, in practice it is optimized to maximize the detection fidelity as described in the following section.

8.4.1 Fidelity

After each fluorescence image is acquired, the presence or absence of an atom in each tweezer is classified using the procedure described in the following. We define the imaging fidelity F as the probability that this classification is correct, that is to say the probability that an atom is identified as present when it was indeed present at the start of the imaging process, or as absent when no atom was initially present. It is important to note that this definition explicitly refers to the start of the exposure, as atoms can be lost during the imaging sequence.
The number of detected photons follows a stochastic process governed by the statistics of spontaneous emission and detection. In the ideal limit, the photon counts associated with a given tweezer follow a Poisson distribution [131]. In practice, however, the measured distribution is affected by additional sources of noise, such as camera readout noise and background scattering, which broaden and distort the ideal Poissonian profile. As a result, the experimentally observed histogram of photon counts typically exhibits two distinct peaks: one corresponding to empty tweezers (background counts) and one to occupied tweezers (atomic fluorescence) as shown in Fig. 8.11.
To model these two distribution, we fit the measured histogram with a bimodal skewed Gaussian distribution, to account for possible asymmetries in the photon-count distribution. The skewed Gaussian function used for each peak is defined as:

$$S(x, A, \mu, \sigma, \alpha) = \frac{2A}{\sqrt{2\pi}\sigma} \exp\left(-\frac{(x-\mu)^2}{2\sigma^2}\right) \left[\frac{1}{2} + \mathrm{erf}\left(\frac{\alpha(x-\mu)}{\sqrt{2}\sigma}\right)\right] \tag{8.4}$$

where A is the amplitude, μ and σ are the mean and standard deviation, respectively, and α controls the skewness of the distribution. The overall model for the photon-count histogram is then given by the sum of two such components,

$$P(x) = S_0(x, A_0, \mu_0, \sigma_0, \alpha_) + S_1(x, A_1, \mu_1, \sigma_1, \alpha_1) \tag{8.5}$$

corresponding respectively to the empty and occupied tweezers. From this fit, we determine the optimal detection threshold x_t that minimizes the overlap between

the two distributions, corresponding to the total classification error

$$\varepsilon(x_t) = \varepsilon(x_t)_1 + \varepsilon(x_t)_2 \tag{8.6}$$

Where $\varepsilon(x_t)_1 = \int_{x_t}^{\infty} S_0(x)dx$ is the tail of the empty trap distribution that lies beyond the threshold representing the false positive error probability and $\varepsilon(x_t)_2 = \int_{-\infty}^{x_t} S_1(x)dx$ is the tail of the occupied trap distribution that lies below the threshold representing the false negative error probability. The imaging fidelity is then defined as

$$F = 1 - \varepsilon(x_t) \tag{8.7}$$

and the optimal threshold x_t is obtained numerically by maximizing F.
Applying this analysis to our experimental data, we fit the photon-count histogram with a bimodal skewed Gaussian function, as shown in Fig. 8.11. By optimizing the threshold x_t that maximizes F, we obtain $x_t = 23$ counts and an imaging fidelity of $F = 99.986(6)\%$ for tweezers operated at a trap depth of 360 µK and an imaging duration of 250 ms.

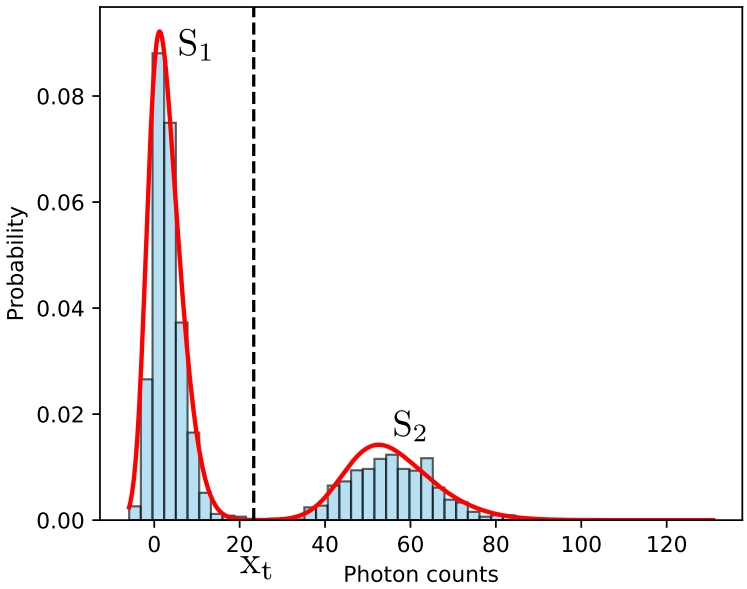

Figure 8.11. Photon-count histogram for a single imaging sequence. The data are fitted with an effective bimodal skewed Gaussian model (red line), representing the "empty" and "occupied" tweezer populations. The vertical dashed line marks the optimal threshold used to classify the presence of an atom, found at 23 counts. The resulting imaging fidelity is 99.986(6)%.

The imaging time can be further reduced at the cost of a decrease in fidelity, enabling faster experimental duty cycles when needed. The dependence of the fidelity on imaging duration is shown in Fig. 8.12, illustrating the trade-off between measurement speed and detection accuracy.
The error bars shown in Fig. 8.12, as well as those reported in the following results, were obtained using the bootstrap method [132]. The bootstrap is a non-parametric resampling approach where multiple synthetic datasets are generated by randomly drawing subset of data points with replacement from the original sample.

For each resampled dataset, the relevant statistical quantity is recalculated, and the distribution of these values provides an empirical estimate of the associated uncertainty. This method offers a robust, data-driven way to evaluate statistical errors without relying on assumptions about the functional form of the underlying probability distribution.

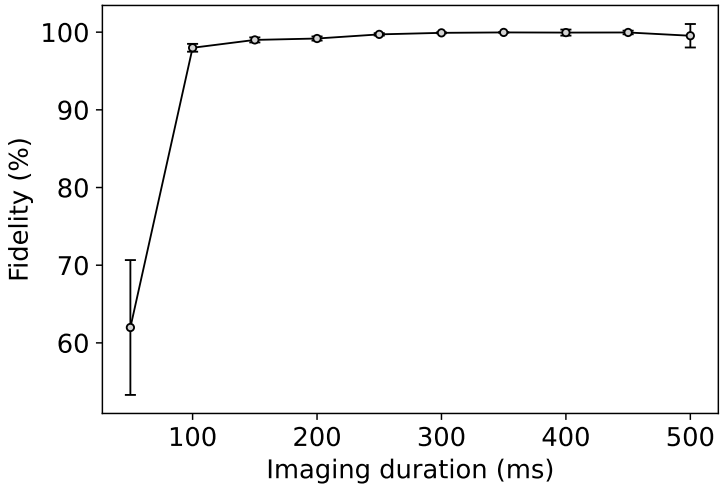

Figure 8.12. Measured imaging fidelity as a function of imaging duration for a fixed trap depth of 360 μK. Longer exposure times lead to improved photon statistics and higher fidelity, saturating near unity for imaging durations above 250 ms.

8.4.2 Survival probability

The ability to preserve atomic confinement during fluorescence imaging is a crucial requirement in optical tweezer array experiments. Post-imaging rearrangement protocols and engineered interactions between the atoms rely not only on identifying the positions of atoms with high fidelity, but also on ensuring that the atoms remain trapped after the imaging sequence.

For this reason, in addition to optimizing the imaging fidelity, it is essential to maximize the survival probability, defined as the likelihood that an atom present at the beginning of the imaging process remains in the trap at its end. We denote this quantity as S.

In the ideal case of perfect imaging fidelity ($F = 1$), the survival probability could be directly determined by acquiring two consecutive fluorescence images under identical conditions and evaluating the fraction of atoms detected in both. This fraction would correspond to S. In realistic conditions, where $F < 1$, this approach provides only an approximate estimate, since false positives (erroneous detection of empty traps) and false negatives (missed detections of occupied traps) introduce systematic biases. A more refined model that explicitly accounts for these imperfections can be used for accurate determination of the survival probability [48].

As a first-order approximation, considering our high detection fidelity, we employ this two-image method to estimate the survival probability and to investigate its dependence on the photon scattering rate during fluorescence imaging. Experimen-

tally, we prepare the array of single atoms in the tweezers, and we acquire a first fluorescence image to identify which traps are occupied. After the first acquisition, to prevent atom loss between successive exposures, both the trapping potential and the cooling light remain continuously active throughout the measurement sequence, maintaining stable trapping conditions. A second image is taken following a 300 ms delay. This interval corresponds to the combined camera readout time and the period required for the system to become ready for the next trigger, ensuring that both images are captured under identical experimental conditions. By comparing the two images, we extract the survival probability as the fraction of atoms that remain confined in their traps over the duration of the imaging sequence.
The resulting measurements are presented in Fig. 8.13. Each data point represents the mean survival probability obtained from repeated experimental runs, with error bars indicating the corresponding statistical uncertainty. As shown in the figure, the survival probability decreases sharply with increasing scattering rate during fluorescence imaging. At low scattering rates, atoms are almost always retained in the trap after imaging, whereas at higher rates photon recoil heating becomes significant, leading to enhanced atom loss. A closer view of the data around the optimal scattering regime is shown in Fig. 8.14, where the survival probability is compared with the imaging fidelity. At high scattering rates, atom loss during the imaging sequence prevents the formation of a clear bimodal histogram of detected fluorescence counts, making fidelity estimation less reliable. From this characterization, we identify the optimal imaging condition corresponding to a scattering rate of 3.12 MHz, which maximizes both survival probability and fidelity. Under these conditions, we achieve a survival probability of 97(2)% and a fidelity of 99.986(6)%. Previous strontium tweezer experiments employing blue fluorescence imaging combined with active cooling have demonstrated survival probabilities ranging from

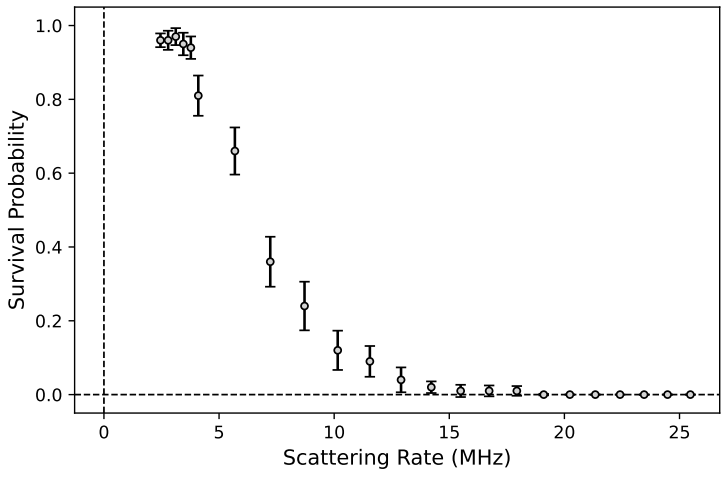

Figure 8.13. Measured single-atom survival probability S as a function of the scattering rate during fluorescence imaging. Each data point corresponds to the average survival probability extracted from multiple experimental repetitions. The observed decrease in survival at higher scattering rates results from photon recoil heating, which enhances atom loss during the imaging process.

approximately 97% to 99.9% [120, 53], while narrow-line red imaging schemes have reached survival probabilities around 97% [62]. In this context, the imaging parameters used in the present work provide a well-chosen starting point for operation, with further improvements in survival probability potentially achievable through careful optimization of the experimental conditions.

8.4.3 Vacuum lifetime

The vacuum lifetime provides a direct and quantitative measure of the quality of the vacuum environment in which the atoms are trapped. It is defined as the characteristic timescale over which a trapped atom is lost due to collisions with residual background gas atoms and molecules. Even under ultra-high vacuum conditions, a small but finite background gas density remains. Collisions between trapped atoms and these residual particles can transfer enough kinetic energy to expel the atom from the optical potential, ultimately limiting the achievable trap lifetime. A long vacuum lifetime is a key figure of merit for the stability and reliability of experiments based on single trapped atoms. In such systems, the loss of even a single atom might require reloading the trap, introducing unwanted dead times and reducing the overall experimental duty cycle. Moreover, in quantum simulation experiments, the loss of a single atom can alter the connectivity between atoms/spins, resulting in systematic errors in the output of the simulator. Ensuring long trap lifetimes is therefore essential to perform complex experimental sequences without interruption and with high repetition rates.
To characterize the vacuum lifetime, single atoms are prepared into optical tweezers and an initial fluorescence image is taken to identify which traps are occupied. The

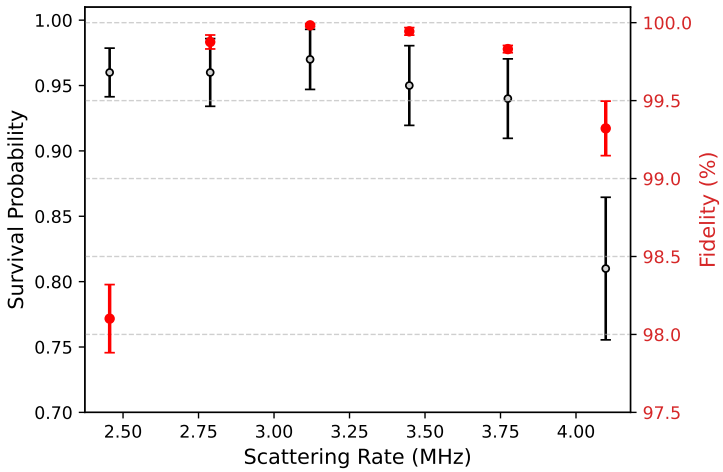

Figure 8.14. Comparison between the survival probability (black circles, left axis) and the imaging fidelity (red squares, right axis) as a function of the photon scattering rate during fluorescence imaging. The two quantities exhibit opposite trends: while increasing the scattering rate initially improves the signal-to-noise ratio and thus the fidelity, excessive scattering induces heating that reduces the survival probability. The optimal operating point is found at a scattering rate of 3.12 MHz, where both survival and fidelity reach their maximal values

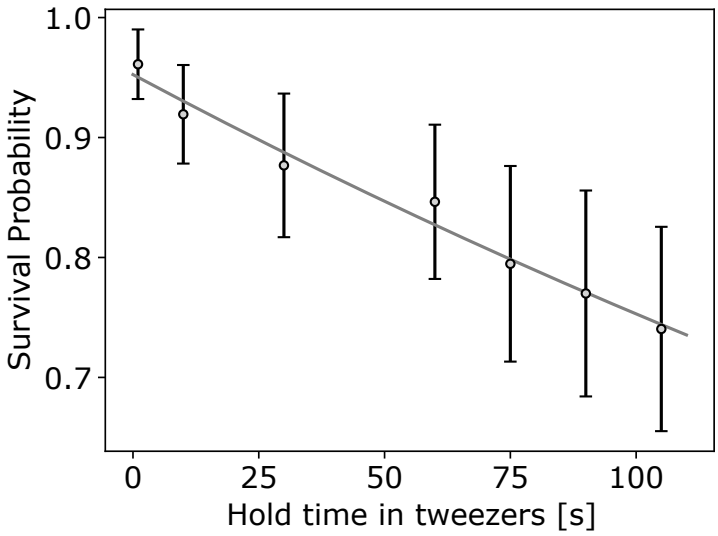

Figure 8.15. Measurement of the vacuum lifetime. The survival probability of a single atom in the tweezer is plotted as a function of the hold time. The experimental data (black dot wit error bars) are fitted with an exponential decay function (gray line), yielding a lifetime of $\tau = 425(25)$s.

trapping and cooling light are then left on for a variable hold time, t_{hold}, during which collisions with background gas may lead to atom loss. After this interval, a second fluorescence image is acquired, and the fraction of atoms that remain trapped is extracted. Repeating the procedure for different values of t_{hold} allows us to determine the survival probability $P(t)$ as a function of time. The resulting data, shown in Fig. 8.15, are fitted with a simple exponential decay model:

$$P(t) = e^{-\frac{t}{\tau_{\text{vac}}}} \tag{8.8}$$

where τ_{vac} denotes the vacuum lifetime. Yielding a vacuum lifetime of $\tau_{\text{vac}} = 425(25)$s. This value compares favorably with reported values in state-of-the-art optical tweezer experiments, which typically range from a few tens to several hundreds of seconds [53, 49, 48]. This long lifetime confirms that background gas collisions do not constitute a limiting factor for the present experiment and enables extended experimental sequences without the need for frequent reloading.

8.4.4 Atom temperature

Another key parameter in experiments with individually trapped atoms is their temperature, which determines the spatial and motional extent of the atom within the tweezer potential and is directly related to the mean motional quantum number. Therefore, it serves as a key diagnostic parameter for assessing trap quality and identifying sources of unwanted heating. A precise knowledge of the temperature is crucial for optimizing subsequent processes such as the preparation of coherent quantum states and the implementation of high-fidelity operations in neutral-atom

quantum computing platforms. Moreover, temperature measurements provide insight into possible heating mechanisms, including trapping-laser intensity noise, mechanical vibrations, and residual photon scattering.

In our experiment, the atomic temperature was determined using the release-and-recapture technique, a widely used and reliable technique in the field of atomic physics for determining the temperature of atoms confined in optical dipole traps. The principle of the method is straightforward: a single atom, initially confined in the optical tweezer, is released by switching off the trapping laser for a controlled duration t_{off}. The trap is then reactivated, and we measure whether the atom is recaptured or lost. During the free-expansion interval, the atom moves according to its initial thermal velocity. If its total energy remains below the trap depth, it stays within the capture region and is recaptured once the trap is turned back on. Conversely, atoms with higher energies escape the trapping volume and are lost. Because each measurement outcome is binary (recaptured or lost), the experiment is repeated many times for each release duration, yielding a statistical estimate of the recapture probability $P_{\text{rec}}(t_{\text{off}})$. The shape of $P_{\text{rec}}(t_{\text{off}})$ encodes the atomic velocity distribution and hence the temperature of the atom. However, the relationship between temperature and recapture probability cannot be expressed analytically in a simple form, since the atomic motion in the optical potential is nonlinear and affected by several factors such as the Gaussian beam profile, gravity, and possible trap anisotropy. For this reason, data analysis relies on comparison with Monte Carlo simulations that realistically reproduce the entire release-and-recapture process.

For the present work, we adapted the simulation framework developed in Ref. [133], which implements a full classical thermodynamic model of atomic motion. In this approach, atoms are initialized with random positions and velocities drawn from a Boltzmann distribution at temperature T. Each trajectory is then evolved for a release time t_{off} in the absence of the optical potential, including the effect of gravity. After the trap is reactivated, the atom is considered recaptured if its total energy remains below the trap depth. The model incorporates the realistic Gaussian potential, accounting for the dependence of the radial and axial trapping frequencies trap depth on laser parameters such as wavelength, power and waist. For each release duration, the simulation performs a large number of independent realizations, and the fraction of recaptured atoms, $P_{\text{sim}}(t_{\text{off}}, T) = \frac{N_{\text{recaptured}}}{N_{\text{total}}}$, is compared to the measured data. The optimal temperature is obtained by minimizing the normalized deviation between simulation and experiment. Fig. 8.16 shows the experimental recapture probabilities together with the best-fit Monte Carlo simulation, which reproduces the data with a good agreement. From this analysis, we obtain an atomic temperature of 12.95(5) µK for atoms trapped in optical tweezers at 813 nm with a trap depth of 360 µK.

Comparisons with release-and-recapture simulations in previous strontium tweezer experiments using blue imaging combined with active cooling have yielded temperatures in the few-microkelvin regime [53]. In optimally cooled conditions, narrow-line imaging schemes have reported temperatures as low as 1.8 µK, consistent with proximity to the radial motional ground state for typical trap depths [62]. In this context, the temperature extracted here is consistent with established cooling regimes in strontium tweezer platforms and provides a practical starting point for further optimization toward lower motional temperatures.

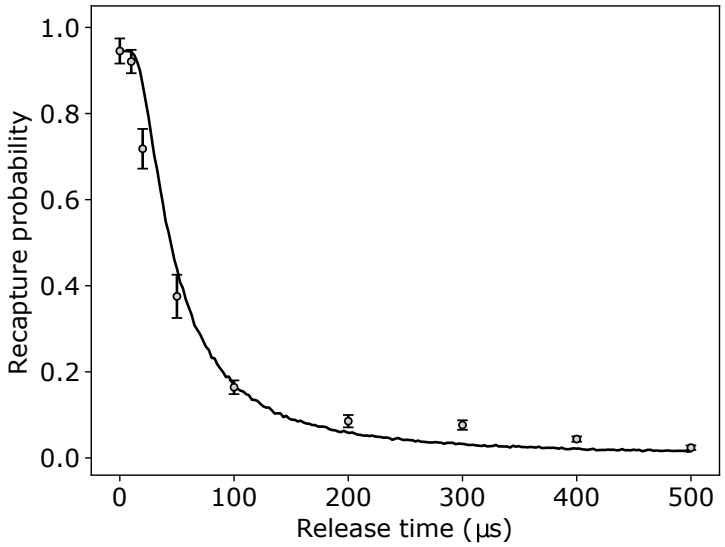

Figure 8.16. Recapture probability plotted as a function of the release time for a release and recapture measurements.The data (dots with error bars) are compared with a Monte Carlo simulation (solid line). The temperature extracted from the simulation is 12.95(5) µK.

Chapter 9

Conclusion and outlook

9.1 Summary and conclusions

In this work, I presented the design, development, and characterization of a neutral-atom quantum simulation platform based on individually trapped neutral Strontium atoms in optical tweezer arrays.
The experimental apparatus was designed, built, and optimized entirely within our laboratory, from the construction of the vacuum system and optical setups to the development of cooling, trapping, and imaging techniques, with the goal of establishing a robust and scalable system for the deterministic preparation and control of single atoms for quantum simulation purposes.
One of the key achievements of this work was the realization and optimization of a two-stage 3D magneto-optical trap of ^{88}Sr. In the first stage, we operated on the strong dipole-allowed $^1S_0 \rightarrow {}^1P_1$ transition at 461 nm, realizing a "blue MOT" that captured and pre-cooled atoms from a thermal atomic beam to temperatures of 6.4 mK, with a typical density of $\sim 4 \times 10^9\,\mathrm{cm}^{-3}$. We leveraged the shielded blu MOT configuration to enhance the atom number by up to 80% (enabled by adding a red beam resonant on the 689 nm transition). To further reduce the temperature and increase the phase-space density, the atoms were subsequently transferred to a "red MOT" operating on the narrow intercombination line $^1S_0 \rightarrow {}^3P_1$ at 689 nm. By sequentially employing a broadband cooling stage followed by a single-frequency narrow-line MOT, we reached final temperatures of 5.4 μK and densities approaching $3 \times 10^{10}\,\mathrm{cm}^{-3}$, providing ideal initial conditions for loading into tightly focused optical tweezers.
Building upon this cold atomic reservoir, we demonstrated the efficient transfer of atoms from the MOT into optical tweezers and the detection of single trapped atoms. We implemented high-fidelity fluorescence imaging based on photon-counting detection of scattered light, reaching a single-atom detection fidelity of 99.986% and a post-imaging survival probability of approximately 97(2)%. These results confirm the robustness and efficiency of our trapping and cooling protocols. Independent release-and-recapture measurements estimate the atomic temperatures in the tweezers to be 12.95(5) µK, confirming that the implemented cooling and loading sequences preserve excellent control over the motional degree of freedom of the atoms.
These results constitute a decisive step toward the realization of a fully programmable

quantum simulator based on neutral Strontium atoms confined in reconfigurable arrays of optical tweezers. The platform combines the geometric flexibility of optical tweezer architectures with the rich internal structure of two-electron atoms. Moreover, by exploiting coherent excitation to Rydberg states, controllable and long-range interactions can be engineered between individual atoms, enabling the simulation of complex many-body Hamiltonians.

9.2 Short-term goals: reordering and Rydberg interaction

In the near future, we plan to integrate a spatial light modulator (SLM), which is currently being characterized, into the experimental setup for the generation of static tweezer arrays. Two crossed AODs will be employed to dynamically transport individual atoms between sites, enabling active reordering and the generation of defect-free arrays with arbitrary geometries. This capability will allow us to deterministically assemble atomic configurations tailored to specific quantum simulation tasks. We are also exploring the feasibility of using an SLM with a fast phase mask refresh rate of 1.2 kHz to directly rearrange all atoms in parallel, in 2D and even in 3D configurations.
The next major step will be the implementation of a two-photon excitation scheme to access high-lying Rydberg states. This addition will introduce tunable, long-range interactions between atoms, marking the transition from passive trapping and control to the realization of fully interacting quantum systems. By adjusting the interatomic distance, the principal quantum number and the orbital character of the excited Rydberg state (e.g., s or d), we can control not only the strength and range of the interactions, but also their nature, ranging from isotropic van der Waals to strongly anisotropic dipole–dipole couplings. This level of tunability provides an exceptionally rich toolbox for engineering diverse quantum Hamiltonians and exploring a wide variety of many-body phenomena.
The resulting platform combines high flexibility and scalability: it will enable the generation of multidimensional arrays of single atoms with arbitrary geometries and adjustable interatomic distances, while supporting fast, coherent, and long-range interactions mediated by Rydberg excitation. These features make it a versatile tool for the implementation of quantum spin models, the investigation of quantum phase transitions, and the controlled generation of multi-particle entangled states.
Although the focus of this thesis has been on developing the neutral-atom tweezer platform as a basis for quantum simulation, it is worth noting that the same architecture is also highly relevant for other frontier applications. In particular, it provides a promising route toward scalable quantum computing architectures based on Rydberg-mediated entangling gates [100, 134], as well as for quantum metrology and optical clock experiments [135, 136].

9.3 Quantum simulation: Ising, XY model

A promising research direction that we aim to pursue with this platform is the study of spin systems. Rydberg atoms trapped in optical tweezers are particularly well

suited for simulating the behavior of various spin Hamiltonians in both one, two and three dimensions.
The Hamiltonian describing an ensemble of atoms, in which the electronic ground state $|g\rangle$ is coherently coupled to a Rydberg state $|r\rangle$ by a global laser field with Rabi frequency Ω and detuning δ, can be directly mapped onto a quantum Ising model of spin-1/2 particles. In this mapping, the two atomic states define the spin basis as $|\downarrow\rangle = |g\rangle$ and $|\uparrow\rangle = |r\rangle$. The resulting Hamiltonian takes the form [30, 28]:

$$H = \frac{\hbar\Omega}{2} \sum_i \sigma_x^i - \hbar\delta \sum_i n_i + \sum_{i<j} V_{i,j} n_i n_j \tag{9.1}$$

with:

$$V_{i,j} = \frac{C_6}{R_{i,j}^6} \tag{9.2}$$

where n_i denotes the operator counting Rydberg excitations at site i, and σ_x^i is the Pauli matrix acting on that site. Since each site hosts a single atom that can either occupy the ground state ($n_i = 0$) or the Rydberg state ($n_i = 1$), the excitation operator can be explicitly written as

$$n_i = (\sigma_z^i + 1)/2 \tag{9.3}$$

With this identification, the Hamiltonian is readily mapped onto the Ising model Hamiltonian [137]. The first term in Eq. 9.1 represents the coupling of spins to a transverse magnetic field $B_\perp \propto \Omega$, while the second term mimics the interaction with a longitudinal magnetic field $B_\parallel \propto -\delta$. The Ising coupling $J_{ij} = V_{ij}$ decays with the interatomic distance as $1/R_{ij}^6$, reflecting the van der Waals interaction between Rydberg excitations.
In the simplest configuration, a homogeneous laser field provides a spatially uniform Rabi coupling and detuning for all atoms in the array. However, more complex Hamiltonians can be engineered by introducing site-dependent Rabi frequencies or detunings, for instance, by addressing individual trapping sites with an additional laser field, implemented through the superposition of the optical tweezer array with a separate addressing beam pattern generated by a SLM or by crossed AODs.
In typical experiments, the interaction term remains fixed, while the parameters Ω and δ can be dynamically tuned to explore different regimes of the phase diagram. A possible approach is to initialize the system in a trivial phase, such as the paramagnetic state, and then abruptly change one of the control parameters (quantum quench) to study the subsequent time evolution under the effective Ising Hamiltonian. The single-site resolution achievable in optical tweezer arrays enables direct measurement of both the total magnetization, defined as the fraction of Rydberg excitations ($|\uparrow\rangle$) relative to the total number of atoms, and the spin–spin correlation function, which quantifies the conditional probability of finding a Rydberg excitation at site j given one already present at site i.
The van der Waals interactions between identical Rydberg states have been engineered to implement the transverse-field Ising Hamiltonian for spin-1/2 systems, across a variety of geometries and interaction strengths in one and two dimensions [138]. Subsequent experiments have scaled this approach to systems comprising

hundreds of individually controlled atoms [33], enabling the observation of phase transitions into spatially ordered states that break discrete symmetries and the investigation of critical dynamics across such transitions [31]. Further work has explored the dynamics of artificial one and two dimensional quantum antiferromagnets with different lattice geometries [139], and realized large-scale two-dimensional arrays of hundreds of Rydberg atoms implementing an extended transverse-field Ising Hamiltonian. These studies have revealed the emergence of antiferromagnetic correlations and long-range order across diverse geometries [36].

Beyond the Ising model, the system can be extended to realize an XY-type spin Hamiltonian by considering atoms excited to different Rydberg states that are coupled through dipole–dipole interactions. A common implementation involves two Rydberg levels, such as $|\mathrm{nS}\rangle$ and $|\mathrm{nP}\rangle$, typically separated by a few gigahertz. These two states once again form an effective spin-1/2 basis, defined as $|\downarrow\rangle = |\mathrm{nS}\rangle$ and $|\uparrow\rangle = |\mathrm{nP}\rangle$.
The resonant dipole–dipole interaction between atoms in these states induces a coherent exchange of their internal excitations. The corresponding interaction potential scales as C_3/R^3, where C_3 is the dipolar coupling coefficient and R is the interatomic distance. When a microwave field couples the two Rydberg states, the system can be described by an effective spin XY Hamiltonian, where the microwave coupling acts as an effective external magnetic field [30]:

$$H = \frac{\hbar\Omega_{\mu w}}{2}\sum_i \sigma_x^i - \frac{\hbar\delta_{\mu w}}{2}\sum_i \sigma_z^i + \sum_{i\neq j}\frac{C_3}{R_{ij}^3}(\sigma_+^i\sigma_-^j + \sigma_-^i\sigma_+^j) \tag{9.4}$$

where $\Omega_{\mu w}$ and $\delta_{\mu w}$ denote the Rabi frequency and detuning of the microwave drive, respectively. In this model, the first term represents the coupling of the effective spins to a transverse microwave field, inducing coherent oscillations between $|\mathrm{nS}\rangle$ and $|\mathrm{nP}\rangle$, analogous to spin flips between $|\downarrow\rangle$ and $|\uparrow\rangle$. The second term corresponds to a longitudinal magnetic field that introduces an energy imbalance between the two spin states, thereby controlling their relative populations. The third term describes the resonant dipole–dipole interaction, which enables coherent exchange of excitations, i.e. spin-spin exchanges between atoms. Since the dipole–dipole interaction decays as $1/R^3$, it is most significant for nearest neighbors, but can also mediate interactions between more distant spins, depending on the lattice spacing. The competition between the exchange interaction and the external field terms can be tuned by varying the microwave Rabi frequency $\Omega_{\mu w}$ and detuning $\delta_{\mu w}$, allowing exploration of different dynamical and many-body regimes. In particular, by controlling these parameters, one can access regions of the phase diagram where collective quantum phenomena, such as quantum phase transitions or correlated spin transport, emerge from the interplay of coherent driving and long-range dipolar interactions.
Several works have leveraged the dipole–dipole interaction between different Rydberg states to explore the rich physics emerging from such XY type couplings. For instance, the realization of a one-dimensional 1/2 spin chain governed by an effective XY Hamiltonian demonstrated how the interplay between coherent Rabi coupling and Rydberg interactions gives rise to a symmetry-protected topological (SPT) phase [140]. Similarly, a synthetic spin-orbit coupled system described by a

generalized XY Hamiltonian with a density-dependent Peierls phase has been implemented [141], extending conventional spin-exchange dynamics to include controllable, density-dependent gauge fields. More recently, programmable two-dimensional Rydberg arrays have been realized, described by frustrated XY Hamiltonians in which competing interactions give rise to regimes compatible with a topological $\mathbb{Z}_2$ spin liquid [32].

Although both the Ising and XY spin models have been extensively studied, several fundamental questions remain open and can be effectively addressed using this platform. These include the impact of geometric frustration, a comprehensive exploration of the system's phase diagram, the characterization of its dynamical response to sudden parameter quenches, and the investigation of how disorder and imperfections affect the system's behavior.
More complex spin models, such as the three-dimensional XXZ [142] and XYZ models [143], have also been explored, along with the role of quantum gauge fields in two-dimensional geometries [144]. In this context, the experimental platform developed and described in this thesis will provide a powerful tool to investigate these rich quantum phenomena. By enabling full control and detection at the single-particle level, it will pave the way for a new generation of studies of quantum many-body dynamics with individual-particle control.

The results reported in this thesis demonstrate the successful implementation of a robust and high-fidelity platform for optical trapping and imaging of single strontium atoms. The apparatus provides the foundation for future quantum simulation experiments with alkaline-earth atoms excited to the Rydberg state, offering precise control over individual particles and the ability to scale towards larger, programmable atomic arrays.

Bibliography

[1] I. M. Georgescu, S. Ashhab, and F. Nori. Quantum simulation. *Rev. Mod. Phys.*, 86:153–185, Mar 2014.

[2] R. P. Feynman. Simulating physics with computers. *Int. J. Theor. Phys.*, 21:467–488, 1982.

[3] Iulia Buluta and Franco Nori. Quantum simulators. *Science*, 326(5949):108–111, 2009.

[4] E. Altman, K. R. Brown, G. Carleo, L. D. Carr, Eà Demler., C. Chin, S. E. DeMarco, B.and Economou, M. A. Eriksson, K. C. Fu, M. Greiner, K. R.A. Hazzard, R. G. Hulet, A. J. Kollár, B. L. Lev, M. D. Lukin, R. Ma, X. Mi, S. Misra, C. Monroe, K. Murch, Z. Nazario, K. Ni, A. C. Potter, P. Roushan, M. Saffman, M. Schleier-Smith, I. Siddiqi, R. Simmonds, M. Singh, I.B. Spielman, K. Temme, D. S. Weiss, J. Vučković, V. Vuletić, J. Ye, and M. Zwierlein. Quantum simulators: Architectures and opportunities. *PRX Quantum*, 2:017003, Feb 2021.

[5] Seth Lloyd. Universal quantum simulators. *Science*, 273(5278):1073–1078, 1996.

[6] M. Greiner, O. Mandel, T. Esslinger, T. W. Hänsch, and I. Bloch. Quantum phase transition from a superfluid to a mott insulator in a gas of ultracold atoms. *Nature*, 415:39–44, 2002.

[7] Jonathan Simon, Waseem S. Bakr, Ruichao Ma, M. Eric Tai, Philipp M. Preiss, and Markus Greiner. Quantum simulation of antiferromagnetic spin chains in an optical lattice. *Nature*, 472(7343):307–312, 2011.

[8] Anton Mazurenko, Christie S. Chiu, Geoffrey Ji, Maxwell F. Parsons, Márton Kanász-Nagy, Richard Schmidt, Fabian Grusdt, Eugene Demler, Daniel Greif, and Markus Greiner. A cold-atom fermi–hubbard antiferromagnet. *Nature*, 545(7655):462–466, 2017.

[9] Gregor Jotzu, Michael Messer, Rémi Desbuquois, Martin Lebrat, Thomas Uehlinger, Daniel Greif, and Tilman Esslinger. Experimental realization of the topological haldane model with ultracold fermions. *Nature*, 515:237–240, 2014.

[10] Marc Cheneau, Peter Barmettler, Dario Poletti, Manuel Endres, Peter Schauß, Takeshi Fukuhara, Christian Gross, Immanuel Bloch, Corinna Kollath, and

Stefan Kuhr. Light-cone-like spreading of correlations in a quantum many-body system. *Nature*, 481(7382):484–487, 2012.

[11] S. Trotzky, Y.-A. Chen, A. Flesch, I. P. McCulloch, U. Schollwöck, J. Eisert, and I. Bloch. Probing the relaxation towards equilibrium in an isolated strongly correlated one-dimensional bose gas. *Nature Physics*, 8(4):325–330, 2012.

[12] H. Häffner, C. F. Roos, and R. Blatt. Quantum computing with trapped ions. *Physics Reports*, 469(4):155–203, 2008.

[13] C. J. Ballance, T. P. Harty, N. M. Linke, M. A. Sepiol, and D. M. Lucas. High-fidelity quantum logic gates using trapped-ion hyperfine qubits. *Phys. Rev. Lett.*, 117:060504, Aug 2016.

[14] D. Porras and J. I. Cirac. Effective quantum spin systems with trapped ions. *Phys. Rev. Lett.*, 92:207901, May 2004.

[15] A. Friedenauer, H. Schmitz, J. T. Glueckert, D. Porras, and T. Schaetz. Simulating a quantum magnet with trapped ions. *Nature Physics*, 4:757–761, 2008.

[16] K. Kim, M.-S. Chang, S. Korenblit, R. Islam, E. E. Edwards, J. K. Freericks, G.-D. Lin, L.-M. Duan, and C. Monroe. Quantum simulation of frustrated ising spins with trapped ions. *Nature*, 465(7298):590–593, 2010.

[17] Rainer Blatt and Christian F. Roos. Quantum simulations with trapped ions. *Nature Physics*, 8:277–284, 2012.

[18] Christopher Monroe, Wesley C. Campbell, L.-M. Duan, Zhe-Xuan Gong, Alexey V. Gorshkov, Paul W. Hess, Rajibul Islam, Kihwan Kim, Guido Pagano, Philip Richerme, Crystal Senko, and Norman Y. Yao. Programmable quantum simulations of spin systems with trapped ions. *Reviews of Modern Physics*, 93(2):025001, 2021.

[19] Morten Kjaergaard, Max E. Schwartz, Jochen Braumüller, Philip Krantz, Joel I.-J. Wang, Simon Gustavsson, and William D. Oliver. Superconducting qubits: Current state of play. *Annual Review of Condensed Matter Physics*, 11(1):369–395, 2020.

[20] A. A. Houck, H. E. Türeci, and J. Koch. On-chip quantum simulation with superconducting circuits. *Nature Physics*, 8:292–299, 2012.

[21] Alexandre Blais, Arne L. Grimsmo, Steven M. Girvin, and Andreas Wallraff. Circuit quantum electrodynamics. *Reviews of Modern Physics*, 93(2):025005, 2021.

[22] D. Marcos, P. Rabl, E. Rico, and P. Zoller. Superconducting circuits for quantum simulation of dynamical gauge fields. *Phys. Rev. Lett.*, 111:110504, Sep 2013.

[23] Y. Salathé, M. Mondal, M. Oppliger, J. Heinsoo, P. Kurpiers, A. Potočnik, A. Mezzacapo, U. Las Heras, L. Lamata, E. Solano, A. Wallraff, and S. Filipp. Digital quantum simulation of spin models with circuit quantum electrodynamics. *Physical Review X*, 5(2):021027, 2015.

[24] Alán Aspuru-Guzik and Philip Walther. Photonic quantum simulators. *Nature Physics*, 8(4):285–291, 2012.

[25] Jianwei Wang, Fabio Sciarrino, Anthony Laing, and Mark G Thompson. Integrated photonic quantum technologies. *Nature Photonics*, 14:273–284, 2020.

[26] Daniel Loss and David P DiVincenzo. Quantum computation with quantum dots. *Physical Review A*, 57(1):120, 1998.

[27] Ronald Hanson, Leo P Kouwenhoven, Jason R Petta, Seigo Tarucha, and Lieven MK Vandersypen. Spins in few-electron quantum dots. *Reviews of Modern Physics*, 79(4):1217, 2007.

[28] Adam M. Kaufman and Kang-Kuen Ni. Quantum science with optical tweezer arrays of ultracold atoms and molecules. *Nature Reviews Physics*, 3:667–685, 2021.

[29] Manuel et al. Endres. Atom-by-atom assembly of defect-free one-dimensional cold atom arrays. *Science*, 354(6315):1024–1027, 2016.

[30] A. Browaeys and T. Lahaye. Many-body physics with individually controlled rydberg atoms. *Nat. Phys.*, 16:132–142, 2020.

[31] H. Bernien, S. Schwartz, A. Keesling, H. Levine, A. Omran, H. Pichler, S. Choi, A. S. Zibrov, M. Endres, M. Greiner, V. Vuletić, and M. D. Lukin. Probing many-body dynamics on a 51-atom quantum simulator. *Nature*, 551:579–584, 2017.

[32] Giulia Semeghini, Harry Levine, Alexander Keesling, Sepehr Ebadi, Tout T. Wang, Dolev Bluvstein, Ruben Verresen, Hannes Pichler, Marcin Kalinowski, Rhine Samajdar, Ahmed Omran, Subir Sachdev, Ashvin Vishwanath, Markus Greiner, Vladan Vuletić, and Mikhail D. Lukin. Probing topological spin liquids on a programmable quantum simulator. *Science*, 374(6572):1242–1247, 2021.

[33] Sepehr Ebadi, Tout T. Wang, Harry Levine, Alexander Keesling, Giulia Semeghini, Ahmed Omran, Dolev Bluvstein, Rhine Samajdar, Hannes Pichler, Wen Wei Ho, Soonwon Choi, Subir Sachdev, Markus Greiner, Vladan Vuletić, and Mikhail D. Lukin. Quantum phases of matter on a 256-atom programmable quantum simulator. *Nature*, 595(7866):227–232, 2021.

[34] M. A. Norcia, A. W. Young, and A. M. Kaufman. Microscopic control and detection of ultracold strontium in optical-tweezer arrays. *Phys. Rev. X*, 8:041054, Dec 2018.

[35] Daichi Okuno, Yuma Nakamura, Toshi Kusano, Yosuke Takasu, Nobuyuki Takei, Hideki Konishi, and Yoshiro Takahashi. High-resolution spectroscopy and single-photon rydberg excitation of reconfigurable ytterbium atom tweezer arrays utilizing a metastable state. *Journal of the Physical Society of Japan*, 91(8):084301, 2022.

[36] Pascal Scholl, Michael Schuler, Hannah J. Williams, Alexander A. Eberharter, Daniel Barredo, Kai-Niklas Schymik, Vincent Lienhard, Louis-Paul Henry, Thomas C. Lang, Thierry Lahaye, Andreas M. Läuchli, and Antoine Browaeys. Quantum simulation of 2d antiferromagnets with hundreds of rydberg atoms. *Nature*, 595(7866):233–238, 2021.

[37] Grégoire Pichard, Desiree Lim, Étienne Bloch, Julien Vaneecloo, Lilian Bourachot, Gert-Jan Both, Guillaume Mériaux, Sylvain Dutartre, Richard Hostein, Julien Paris, Bruno Ximenez, Adrien Signoles, Antoine Browaeys, Thierry Lahaye, and Davide Dreon. Rearrangement of individual atoms in a 2000-site optical-tweezer array at cryogenic temperatures. *Phys. Rev. Appl.*, 22:024073, Aug 2024.

[38] Neng-Chun Chiu, Elias C. Trapp, Jinen Guo, Mohamed H. Abobeih, Luke M. Stewart, Simon Hollerith, Pavel L. Stroganov, Marcin Kalinowski, Alexandra A. Geim, Simon J. Evered, Sophie H. Li, Xingjian Lyu, Lisa M. Peters, Dolev Bluvstein, Tout T. Wang, Markus Greiner, Vladan Vuletić, and Mikhail D. Lukin. Continuous operation of a coherent 3,000-qubit system. *Nature*, 646:1075–1080, 2025.

[39] Hannah J. Manetsch, Gyohei Nomura, Elie Bataille, Xudong Lv, Kon H. Leung, and Manuel Endres. A tweezer array with 6100 highly coherent atomic qubits. *Nature*, 2025.

[40] Harold J. Metcalf and Peter van der Straten. *Laser Cooling and Trapping*. Springer, New York, 1999.

[41] Claude Cohen-Tannoudji, Jacques Dupont-Roc, and Gilbert Grynberg. *Atom–Photon Interactions: Basic Processes and Applications*. Wiley-VCH, New York, 1992.

[42] A. Ashkin. Trapping of atoms by resonance radiation pressure. *Phys. Rev. Lett.*, 40:729–732, Mar 1978.

[43] S. H. Autler and C. H. Townes. Stark effect in rapidly varying fields. *Phys. Rev.*, 100:703–722, Oct 1955.

[44] R. Grimm, M. Weidemüller, and Y.B. Ovchinnikov. Optical dipole traps for neutral atoms. In *Advances In Atomic, Molecular, and Optical Physics*, volume 42, pages 95–170. Academic Press, 2000.

[45] Daniel A. Steck. *Quantum and Atom Optics*. 2024. Revision 0.16.1, 16 June 2024.

[46] Michael M. Boyd. *High Precision Spectroscopy of Strontium in an Optical Lattice: Towards a New Standard for Frequency and Time*. Phd thesis, University of Washington, 2002.

[47] Ivan H. Deutsch and Poul S. Jessen. Quantum-state control in optical lattices. *Phys. Rev. A*, 57:1972–1986, Mar 1998.

[48] Ivaylo S. Madjarov. *Entangling, controlling, and detecting individual strontium atoms in optical tweezer arrays*. Ph.d. dissertation, California Institute of Technology, 2021.

[49] A. A. Urech. *Single Strontium Atoms in Optical Tweezers*. Phd thesis, Universiteit van Amsterdam, 2023.

[50] G. Morigi, J. Eschner, J. I. Cirac, and P. Zoller. Laser cooling of two trapped ions: Sideband cooling beyond the lamb-dicke limit. *Phys. Rev. A*, 59:3797–3808, May 1999.

[51] J. D. Teufel, T. Donner, D. Li, J. W. Harlow, M. S. Allman, K. Cicak, A. J. Sirois, J. D. Whittaker, K. W. Lehnert, and R. W. Simmonds. Sideband cooling of micromechanical motion to the quantum ground state. *Nature*, 475:359–363, 2011.

[52] A. M. Kaufman, B. J. Lester, and C. A. Regal. Cooling a single atom in an optical tweezer to its quantum ground state. *Phys. Rev. X*, 2:041014, Nov 2012.

[53] Jacob P. Covey, Ivaylo S. Madjarov, Alexandre Cooper, and Manuel Endres. 2000-times repeated imaging of strontium atoms in clock-magic tweezer arrays. *Phys. Rev. Lett.*, 122:173201, May 2019.

[54] Renhao Tao, Maximilian Ammenwerth, Flavien Gyger, Immanuel Bloch, and Johannes Zeiher. High-fidelity detection of large-scale atom arrays in an optical lattice. *Phys. Rev. Lett.*, 133:013401, Jul 2024.

[55] Chun-Chia Chen, Shayne Bennetts, Rodrigo González Escudero, Florian Schreck, and Benjamin Pasquiou. Sisyphus optical lattice decelerator. *Phys. Rev. A*, 100:023401, Aug 2019.

[56] Vladyslav V. Ivanov and Subhadeep Gupta. Laser-driven sisyphus cooling in an optical dipole trap. *Phys. Rev. A*, 84:063417, Dec 2011.

[57] Florian Stellmer. *Production of Quantum-Degenerate Strontium Gases*. Ph.d. thesis, University of Innsbruck, 2013.

[58] National Institute of Standards and Technology. Strontium: Atomic data. `https://physics.nist.gov/PhysRefData/Handbook/Tables/strontiumtable1.htm`. Accessed: 2025-06-20.

[59] Alec Jenkins, Joanna W. Lis, Aruku Senoo, William F. McGrew, and Adam M. Kaufman. Ytterbium nuclear-spin qubits in an optical tweezer array. *Physical Review X*, 12(2):021027, 2022.

[60] M. Yasuda, T. Kishimoto, M. Takamoto, and H. Katori. Photoassociation spectroscopy of ^{88}sr: Reconstruction of the wave function near the last node. *Physical Review A*, 73:011403, 2006.

[61] J. E. Sansonetti and G. Nave. Wavelengths, transition probabilities, and energy levels for the spectrum of neutral strontium (sr i). *Journal of Physical and Chemical Reference Data*, 39:033103, 2010.

[62] A. Urech, M. A. Norcia, J. M. Robinson, A. W. Young, and A. M. Kaufman. Narrow-line imaging of single strontium atoms in shallow optical tweezers. *Physical Review Research*, 4:023245, 2022.

[63] Bahaa E. A. Saleh and Malvin Carl Teich. *Fundamentals of Photonics*. Wiley, Hoboken, NJ, 2nd edition, 2007.

[64] I. H. A. Knottnerus. Tweezer machine for sr atoms using a homebuilt microscope objective from commercial lenses. Ma thesis, University of Amsterdam, 2018.

[65] Eugene Hecht. *Optics*. Pearson, Boston, MA, 5th edition, 2017.

[66] Luca Guariento. *A New Setup for Single Strontium Atoms in Optical Tweezers*. Ph.d. thesis, Università degli Studi di Firenze, 2025. Defended 13 February 2025.

[67] Preangka Roy. Acousto-optic deflector-principles, working and applications. *International Journal of Advanced Networking and Applications*, 15:6126–6130, 01 2024.

[68] Akis P. Goutzoulis. *Design and Fabrication of Acousto-Optic Devices*. CRC Press, 1st edition, 2021.

[69] Max Born and Emil Wolf. *Principles of Optics: Electromagnetic Theory of Propagation, Interference and Diffraction of Light*. Cambridge University Press, Cambridge, UK, 7th edition, 1999.

[70] Joseph W. Goodman. *Introduction to Fourier Optics*. Roberts and Company Publishers, Greenwood Village, CO, 3rd edition, 2005.

[71] Liang Zhu and Jian Wang. Arbitrary manipulation of spatial amplitude and phase using phase-only spatial light modulators. *Scientific Reports*, 4:7441, 2014.

[72] R. W. Gerchberg. A practical algorithm for the determination of phase from image and diffraction plane pictures. *Optik*, 35:237–246, 1972.

[73] Maximilian Ammenwerth, Hendrik Timme, Veronica Giardini, Renhao Tao, Flavien Gyger, Ohad Lib, Dirk Berndt, Dimitrios Kourkoulos, Tim Rom, Immanuel Bloch, and Johannes Zeiher. Dynamical spatial light modulation in the ultraviolet spectral range. *Physical Review Applied*, 2025. Accepted manuscript, 1 July 2025.

[74] C.-H. Wen, S. Gauza, and S.-T. Wu. Photostability of liquid crystals and alignment layers. *Journal of the Society for Information Display*, 13(9):805–811, 2005.

[75] T. Topcu and A. Derevianko. Possibility of triple magic trapping of clock and rydberg states of divalent atoms in optical lattices. *Journal of Physics B: Atomic, Molecular and Optical Physics*, 49(14):144004, 2016.

[76] D. Bluvstein, S. J. Evered, A. A. Geim, S. H. Li, H. Zhou, T. Manovitz, S. Ebadi, M. Cain, M. Kalinowski, D. Hangleiter, J. P. Bonilla Ataides, N. Maskara, I. Cong, X. Gao, P. Sales Rodriguez, T. Karolyshyn, G. Semeghini, M. J. Gullans, M. Greiner, V. Vuletić, and M. D. Lukin. Logical quantum processor based on reconfigurable atom arrays. *Nature*, 626:58–65, 2023.

[77] P. Zupancic, P. M. Preiss, R. Ma, A. Lukin, M. Eric Tai, M. Rispoli, R. Islam, and M. Greiner. Ultra-precise holographic beam shaping for microscopic quantum control. *Optics Express*, 24:13881–13893, 2016.

[78] D. Tsevas. Precise shaping of coherent laser beams with a liquid-crystal-on-silicon spatial light modulator. Master's thesis, Ludwig-Maximilians-Universität München, 2021.

[79] T. A. Savard, K. M. O'Hara, and J. E. Thomas. Laser-noise-induced heating in far-off resonance optical traps. *Phys. Rev. A*, 56:R1095–R1098, Aug 1997.

[80] Y. Y. Jau, A. M. Hankin, T. Keating, I. H. Deutsch, and G. W. Biedermann. Entangling atomic spins with a rydberg-dressed spin-flip blockade. *Nature Physics*, 12(1):71–74, jan 2016.

[81] J. Zeiher, R. van Bijnen, P. Schauß, S. Hild, J.-y. Choi, T. Pohl, I. Bloch, and C. Gross. Many-body interferometry of a rydberg-dressed spin lattice. *Nature Physics*, 12(12):1095–1099, 2016.

[82] C. Gaul, B. J. DeSalvo, J. A. Aman, F. B. Dunning, T. C. Killian, and T. Pohl. Resonant rydberg dressing of alkaline-earth atoms via electromagnetically induced transparency. *Phys. Rev. Lett.*, 116:243001, Jun 2016.

[83] Ivaylo S. Madjarov, Jacob P. Covey, Alexander L. Shaw, Joonhee Choi, Abhishek Kale, Adam Cooper, Hannes Pichler, Vladimir Schkolnik, Jason R. Williams, and Manuel Endres. High-fidelity entanglement and detection of alkaline-earth rydberg atoms. *Nature Physics*, 16(8):857–861, 2020.

[84] Shuo Ma, Alex P. Burgers, Genyue Liu, Jack Wilson, Bichen Zhang, and Jeff D. Thompson. Universal gate operations on nuclear spin qubits in an optical tweezer array of ^{171}Yb atoms. *Phys. Rev. X*, 12:021028, May 2022.

[85] Sven Jandura, Jeff D. Thompson, and Guido Pupillo. Optimizing rydberg gates for logical-qubit performance. *PRX Quantum*, 4:020336, Jun 2023.

[86] Nicolas Schlosser, Georges Reymond, Igor Protsenko, and Philippe Grangier. Sub-poissonian loading of single atoms in a microscopic dipole trap. *Nature*, 411:1024–7, 07 2001.

[87] Jacob Sherson, Christof Weitenberg, Manuel Endres, Marc Cheneau, Immanuel Bloch, and Stefan Kuhr. Single-atom resolved fluorescence imaging of an atomic mott insulator. *Nature*, 467:68–72, 09 2010.

[88] W Bakr, A Peng, M Tai, Ruichao Ma, J Simon, J Gillen, S Fölling, L Pollet, and M Greiner. Probing the superfluid-to-mott insulator transition at the single-atom level. *Science (New York, N.Y.)*, 329:547–50, 07 2010.

[89] Marshall T. DePue, Colin McCormick, S. Lukman Winoto, Steven Oliver, and David S. Weiss. Unity occupation of sites in a 3d optical lattice. *Physical Review Letters*, 82(11):2262–2265, 1999.

[90] M. O. Brown, T. Thiele, C. Kiehl, T.-W. Hsu, and C. A. Regal. Gray-molasses optical-tweezer loading: Controlling collisions for scaling atom-array assembly. *Phys. Rev. X*, 9:011057, Mar 2019.

[91] J. Ang'ong'a, J. T. Wilson, M. E. Kimchi-Schwartz, and H. Bernien. Gray molasses cooling of ^{39}k atoms in optical tweezers. *Physical Review Research*, 4(1):013240, 2022.

[92] Adam L. Shaw, Pascal Scholl, Ran Finklestein, Ivaylo S. Madjarov, Brandon Grinkemeyer, and Manuel Endres. Dark-state enhanced loading of an optical tweezer array. *Phys. Rev. Lett.*, 130:193402, May 2023.

[93] Daniel Barredo, Sylvain de Léséleuc, Vincent Lienhard, Thierry Lahaye, and Antoine Browaeys. An atom-by-atom assembler of defect-free arbitrary two-dimensional atomic arrays. *Science*, 354(6315):1021–1023, 2016.

[94] Remy El Sabeh, Jessica Bohm, Zhiqian Ding, Stephanie Maaz, Naomi Nishimura, Izzat El Hajj, Amer E. Mouawad, and Alexandre Cooper. Efficient algorithms to solve atom reconfiguration problems. ii. assignment-rerouting-ordering algorithm. *Phys. Rev. A*, 108:023108, Aug 2023.

[95] Hyosub Kim, Minhyuk Kim, Woojun Lee, and Jaewook Ahn. Gerchberg-saxton algorithm for fast and efficient atom rearrangement in optical tweezer traps. *Opt. Express*, 27(3):2184–2196, Feb 2019.

[96] T. F. Gallagher. *Rydberg Atoms*. Cambridge University Press, Cambridge, 1994.

[97] J. Lim, H. Lee, J. Lee, and J. Ahn. Review of cold rydberg atoms and their applications. *Journal of the Korean Physical Society*, 63:867–876, 2013.

[98] N. Šibalić, J. D. Pritchard, C. S. Adams, and K. J. Weatherill. *Rydberg Physics*. IOP Expanding Physics. IOP Publishing, 2018.

[99] L. Béguin, A. Vernier, R. Chicireanu, T. Lahaye, and A. Browaeys. Direct measurement of the van der waals interaction between two rydberg atoms. *Physical Review Letters*, 110(26):263201, 2013.

[100] H. Levine, A. Keesling, A. Omran, H. Bernien, S. Schwartz, A. S. Zibrov, M. Endres, M. Greiner, V. Vuletić, and M. D. Lukin. High-fidelity control and entanglement of rydberg-atom qubits. *Physical Review Letters*, 121(12):123603, 2018.

[101] A. Gaëtan, Y. Miroshnychenko, T. Wilk, A. Chotia, M. Viteau, D. Comparat, P. Pillet, A. Browaeys, and P. Grangier. Observation of collective excitation of two individual atoms in the rydberg blockade regime. *Nature Physics*, 5:115–118, 2009.

[102] Chang Qiao, Canzhu Tan, Julia Siegl, Fachao Hu, Zhijing Niu, Yuhai Jiang, Matthias Weidemüller, and Bing Zhu. Rydberg blockade in an ultracold strontium gas revealed by two-photon excitation dynamics. *Phys. Rev. A*, 103:063313, Jun 2021.

[103] S. Ye, X. Zhang, T. C. Killian, H. Shao, J. Chen, and S. Wang. Production of very-high-n strontium rydberg atoms. *Physical Review A*, 88(4):043430, 2013.

[104] L. Couturier, I. Nosske, F. Hu, R. Mukherjee, J. Zeiher, S. Helmrich, S. Blatt, I. Bloch, and M. Weidemüller. Measurement of the strontium triplet rydberg series by depletion spectroscopy of ultracold atoms. *Physical Review A*, 99(2):022503, 2019.

[105] R. Ding, Y. Jiang, D. Zhang, L. Wu, J. Zhao, S. Jia, and S. Zhang. Spectroscopy of ^{87}sr triplet rydberg states. *Physical Review A*, 98(4):042505, 2018.

[106] Veronica Giardini. Development of a novel platform for quantum simulation with sr rydberg atoms. Ma thesis, University of Florence, LENS, 2022.

[107] T. Denecker, Y. T. Chew, O. Guillemant, G. Watanabe, T. Tomita, K. Ohmori, and S. de Léséleuc. Measurement and feedforward correction of the fast phase noise of lasers. *Phys. Rev. A*, 111:042614, Apr 2025.

[108] R. W. P. Drever, J. L. Hall, F. V. Kowalski, J. Hough, G. M. Ford, A. J. Munley, and H. Ward. Laser phase and frequency stabilization using an optical resonator. *Applied Physics B*, 31:97–105, 1983.

[109] Giuseppe Di Domenico, Stefan Schilt, and Pierre Thomann. Simple approach to the relation between laser frequency noise and laser line shape. *Applied Optics*, 49(25):4801–4807, 2010.

[110] T. W. Hänsch and B. Couillaud. Laser frequency stabilization by polarization spectroscopy of a reflecting reference cavity. *Optics Communications*, 35:441–444, 1980.

[111] PHILIP THOMAS STARKEY. A software framework for control and automation of precisely timed experiments. 7 2019.

[112] Wang Yan, Hu Zhao-Hui, and Qi Lu. Comparison of two absorption imaging methods to detect cold atoms in magnetic trap. *Chinese Physics B*, 24(2):024203, 2015.

[113] David A. Smith, Simon Aigner, Sebastian Hofferberth, Michael Gring, Mauritz Andersson, Stefan Wildermuth, Peter Krüger, Stephan Schneider, Thorsten Schumm, and Jörg Schmiedmayer. Absorption imaging of ultracold atoms on atom chips. *Opt. Express*, 19(9):8471–8485, Apr 2011.

[114] A. Yamaguchi. *Metastable State of Ultracold and Quantum Degenerate Ytterbium Atoms: High-Resolution Spectroscopy and Cold Collisions*. Phd thesis, Kyoto University, 2008.

[115] Jonatan Höschele, Sandra Buob, Antonio Rubio-Abadal, Vasiliy Makhalov, and Leticia Tarruell. Atom-number enhancement by shielding atoms from losses in strontium magneto-optical traps. *Phys. Rev. Appl.*, 19:064011, Jun 2023.

[116] Nicola Poli, Marco Schioppo, S. Vogt, Stephan Falke, Uwe Sterr, Ch Lisdat, and G. Tino. A transportable strontium optical lattice clock. *Applied Physics B*, 117, 09 2014.

[117] Hidetoshi Katori, Tetsuya Ido, Yoshitomo Isoya, and Makoto Kuwata-Gonokami. Magneto-optical trapping and cooling of strontium atoms down to the photon recoil temperature. *Phys. Rev. Lett.*, 82:1116–1119, Feb 1999.

[118] John P. Bartolotta, Matthew A. Norcia, Julia R. K. Cline, James K. Thompson, and Murray J. Holland. Laser cooling by sawtooth-wave adiabatic passage. *Phys. Rev. A*, 98:023404, Aug 2018.

[119] S. Snigirev, A. J. Park, A. Heinz, I. Bloch, and S. Blatt. Fast and dense magneto-optical traps for strontium. *Phys. Rev. A*, 99:063421, Jun 2019.

[120] Alexandre Cooper, Jacob P. Covey, Ivaylo S. Madjarov, Sergey G. Porsev, Marianna S. Safronova, and Manuel Endres. Alkaline-earth atoms in optical tweezers. *Phys. Rev. X*, 8:041055, Dec 2018.

[121] Martin Miranda, Ryotaro Inoue, Yuki Okuyama, Akimasa Nakamoto, and Mikio Kozuma. Site-resolved imaging of ytterbium atoms in a two-dimensional optical lattice. *Phys. Rev. A*, 91:063414, Jun 2015.

[122] Karl Nelson, Xiao Li, and David Weiss. Imaging single atoms in a three-dimensional array. *Nature Physics*, 3, 06 2007.

[123] Maxwell F. Parsons, Florian Huber, Anton Mazurenko, Christie S. Chiu, Widagdo Setiawan, Katherine Wooley-Brown, Sebastian Blatt, and Markus Greiner. Site-resolved imaging of fermionic ^{6}Li in an optical lattice. *Phys. Rev. Lett.*, 114:213002, May 2015.

[124] G. J. A. Edge, R. Anderson, D. Jervis, D. C. McKay, R. Day, S. Trotzky, and J. H. Thywissen. Imaging and addressing of individual fermionic atoms in an optical lattice. *Phys. Rev. A*, 92:063406, Dec 2015.

[125] Lin Su, Alexander Douglas, Michal Szurek, Anne Hébert, Aaron Krahn, Robin Groth, Gregory Phelps, Ognjen Marković, and Markus Greiner. Fast single atom imaging for optical lattice arrays. *Nature Communications*, 16, 01 2025.

[126] Elmar Haller, James Hudson, Andrew Kelly, Dylan Cotta, Bruno Peaudecerf, Graham Bruce, and Stefan Kuhr. Single-atom imaging of fermions in a quantum-gas microscope. *Nature Physics*, 11, 03 2015.

[127] Andrea Bergschneider, Vincent M. Klinkhamer, Jan Hendrik Becher, Ralf Klemt, Gerhard Zürn, Philipp M. Preiss, and Selim Jochim. Spin-resolved single-atom imaging of ^{6}Li in free space. *Phys. Rev. A*, 97:063613, Jun 2018.

[128] Alessandro Muzi Falconi, Riccardo Panza, Riccardo Forti, Sara Sbernadori, Omar Abdel Karim, Matteo Marinelli, and Francesco Scazza. Microsecond-scale high-survival and number-resolved detection of ytterbium atom arrays. *arXiv preprint*, 2025. arXiv:2507.01011 [quant-gas].

[129] D. Petrosyan, S. Norrell, C. Poole, and M. Saffman. Fast measurements and multiqubit gates in dual-species atomic arrays. *Phys. Rev. A*, 110:042404, Oct 2024.

[130] M. T. Lichtman. *Coherent operations, entanglement, and progress toward quantum search in a large 2D array of neutral atom qubits*. Phd thesis, University of Wisconsin, Madison, WI, 2015.

[131] H.F. Arnoldus and G. Nienhuis. Photon statistics of fluorescence radiation. *Optica Acta: International Journal of Optics*, 33(6):691–702, 1986.

[132] Bradley Efron and Robert J. Tibshirani. *An Introduction to the Bootstrap*. Chapman & Hall/CRC, New York, 1993.

[133] Ralph Vincent Brooks. *Control and Collisions of ^{87}Rb and ^{133}Cs Atoms in Optical Tweezers*. Doctoral thesis, Durham University, Durham, UK, 2022. Available at Durham E-Theses repository.

[134] Dolev Bluvstein, Harry Levine, Giulia Semeghini, Tout Wang, Sepehr Ebadi, Marcin Kalinowski, Alexander Keesling, Nishad Maskara, Hannes Pichler, Markus Greiner, Vladan Vuletic, and Mikhail Lukin. A quantum processor based on coherent transport of entangled atom arrays. *Nature*, 604:451–456, 04 2022.

[135] Ivaylo S. Madjarov, Alexandre Cooper, Adam L. Shaw, Jacob P. Covey, Vladimir Schkolnik, Tai Hyun Yoon, Jason R. Williams, and Manuel Endres. An atomic-array optical clock with single-atom readout. *Phys. Rev. X*, 9:041052, Dec 2019.

[136] Aaron Young, William Eckner, William Milner, Dhruv Kedar, Matthew Norcia, Eric Oelker, Nathan Schine, Jun Ye, and Adam Kaufman. Half-minute-scale atomic coherence and high relative stability in a tweezer clock. *Nature*, 588:408–413, 2020-12 2020.

[137] S. Blundell. *Magnetism in Condensed Matter*. Oxford Master Series in Condensed Matter Physics. OUP Oxford, 2001.

[138] Henning Labuhn, Daniel Barredo, Sylvain Ravets, Sylvain de Leseleuc, Tommaso Macri, Thierry Lahaye, and Antoine Browaeys. Tunable two-dimensional arrays of single rydberg atoms for realizing quantum ising models. *Nature*, 534, 06 2016.

[139] Vincent Lienhard, Sylvain de Léséleuc, Daniel Barredo, Thierry Lahaye, Antoine Browaeys, Michael Schuler, Louis-Paul Henry, and Andreas M. Läuchli. Observing the space- and time-dependent growth of correlations in dynamically tuned synthetic ising models with antiferromagnetic interactions. *Phys. Rev. X*, 8:021070, Jun 2018.

[140] S. de Léséleuc, Y. Wan, P. T. Brown, D. Barredo, L. Béguin, T. Lahaye, and A. Browaeys. Observation of a symmetry-protected topological phase of interacting bosons with rydberg atoms. *Science*, 365(6455):775–780, 2019.

[141] Vincent Lienhard, Pascal Scholl, Sebastian Weber, Daniel Barredo, Sylvain de Léséleuc, Rukmani Bai, Nicolai Lang, Michael Fleischhauer, Hans Peter Büchler, Thierry Lahaye, and Antoine Browaeys. Realization of a density-dependent peierls phase in a synthetic, spin-orbit coupled rydberg system. *Phys. Rev. X*, 10:021031, May 2020.

[142] P. Scholl, H. J. Williams, G. Bornet, F. Wallner, D. Barredo, L. Henriet, A. Signoles, C. Hainaut, T. Franz, S. Geier, A. Tebben, A. Salzinger, G. Zürn, T. Lahaye, M. Weidemüller, and A. Browaeys. Microwave engineering of programmable xxz hamiltonians in arrays of rydberg atoms. *PRX Quantum*, 3:020303, Apr 2022.

[143] Lea-Marina Steinert, Philip Osterholz, Robin Eberhard, Lorenzo Festa, Nikolaus Lorenz, Zaijun Chen, Arno Trautmann, and Christian Gross. Spatially tunable spin interactions in neutral atom arrays. *Phys. Rev. Lett.*, 130:243001, Jun 2023.

[144] Simon Ohler, Maximilian Kiefer-Emmanouilidis, Antoine Browaeys, Hans Peter Büchler, and Michael Fleischhauer. Self-generated quantum gauge fields in arrays of rydberg atoms. *New Journal of Physics*, 24(2):023017, feb 2022.